UNIVERSITÀ DEGLI STUDI DELL'INSUBRIA
FACOLTÀ DI SCIENZE FISICHE
DIPARTIMENTO DI ALTA TECNOLOGIA

DOTTORATO DI RICERCA IN FISICA ED ASTROFISICA
CICLO XXXIII

Multi-wavelength study of binary millisecond pulsars

Arianna Miraval Zanon

Supervisor: Prof. Francesco Haardt

Co-supervisors: Dr Sergio Campana & Dr Paolo D'Avanzo

Coordinator: Prof. Giuliano Benenti

A.Y. 2020/2021

Contents

Abstract

The main object of my research activity has been the multi-wavelength study of the temporal evolution of binary millisecond pulsars, from the accretion phase to the radio pulsar state and back. I have employed multi-wavelength observations to disentangle and study the different emission mechanisms at play in the same system and to investigate different evolutionary states in the same class of objects.

Pulsars are now known to be fast-spinning, highly-magnetised neutron stars, resulting from the death of a massive star through a supernova explosion. They are a natural laboratory of fundamental physics, allowing us to test gravity in the strong field regime and to study the behaviour of matter in extremely high density states. Millisecond pulsars are a sub-population of neutron stars with very fast spin (hundreds of rotations per second) and relatively weak magnetic field (10^8 G). The short spin periods of millisecond pulsars are the outcome of the accretion onto the neutron star of the mass transferred by a low mass companion star, through an accretion disc.

In this thesis, I present new results on the emission phenomena associated with binary millisecond pulsars in different stages of their evolution. Different manifestations of binary millisecond pulsars will be inspected, including *accreting millisecond X-ray pulsars*, *transitional millisecond pulsars* and *radio millisecond pulsars*. After a general introduction on the pulsar phenomenon in astrophysics, Chapter 1 will be dedicated to explain the evolutionary link and the physical properties of these different classes of sources.

- *Accreting Millisecond X-ray Pulsars* (AMXPs) represent a subclass of transient Low Mass X-ray Binaries (LMXBs) that host an old, weakly magnetic neutron star that accretes mass from a companion star and has been spun up to millisecond periods via transfer of matter and angular momentum. All AMXPs are

transient systems, with accretion discs that run through cycles of outburst, and quiescence. During the outburst the gas stripped from the companion is channeled onto the magnetic poles of the rotating neutron star, giving rise to X-ray pulsations at the neutron star spin frequency. The discovery of AMXPs confirmed evolutionary models that link the neutron stars of LMXBs to those of radio millisecond pulsars, the former being the progenitors of the latter.

Chapter 2 is focused on SAX J1808.4–3658, the first-discovered AMXP. SAX J1808.4–3658 is a neutron star spinning at a period of 2.49-ms and it is part of a tight binary system with an orbital period of 2.01 hr. We analyzed data acquired during the 2019 outburst with the Silicon Fast Astronomical Photometer and Polarizer mounted at the Telescopio Nazionale Galileo, with the Space Telescope Imaging Spectrograph on board the Hubble Space Telescope, and with the Neutron Star Interior Composition Explorer. In this Chapter we present the first detection ever of coherent optical and ultraviolet pulsations at the 2.49-ms spin period of SAX J1808.4–3658 during its 2019 outburst. This discovery challenges the widely accepted paradigm that the pulsed emission of binary millisecond pulsars surrounded by an accretion disc is powered solely by mass accretion. Indeed, energy arguments rule out thermal emission from heated neutron star polar caps or processes related to accretion, and argue against reprocessing of accretion powered X-ray emission. Optical and ultraviolet pulsations are likely driven by synchro-curvature radiation in the pulsar magnetosphere or just outside of it.

- *Transitional Millisecond Pulsars* (tMSPs) are binary pulsars swinging between a state in which they accrete matter from the companion - thus manifesting as AMXPs - and a state in which they appear as radio millisecond pulsars. These objects are con-

sidered the missing link between LMXBs and binary radio millisecond pulsars. During the accretion stage these systems are bright in the X-ray band, instead, when the mass transfer rate decreases the emission in the radio band, powered by the neutron stars rotation, becomes dominant. Only three of these systems are known (with high certainty) so far IGR J1824–2452, PSR J1023+0038 and XSS J12270–4859.

Chapter 3 is devoted to the study of two tMSPs: XSS J12270–4859 and PSR J1023+0038. We analyzed *XMM-Newton* X-ray data of their X-ray active state and also of their quiescent state (or radio pulsar state). Observations during the X-ray active state show a strong and rapid X-ray variability with three different modes: a high luminosity mode ($L_X \sim 8 \times 10^{33}$ erg s^{-1}, 0.3-10 keV) in which the X-ray pulsations at the neutron star spin period are detected, a low mode ($L_X \sim 10^{33}$ erg s^{-1}) during which no pulsations are detected and a flaring mode ($L_X \sim 10^{34}$ erg s^{-1}) also not showing pulsations. Here, we propose two spectral models motivated by different physical scenarios in order to explain the rapid variability between high, low and flare modes. In the first physical scenario, the transition between the observed high and low modes can be explained as a fast transition between the physical 'propeller' state and the radio-ejection pulsar state. In the second physical picture, the radio pulsar is always active, even during the X-ray active state, and the source of power for the pulsations is its rotational energy. XSS J12270–4859 is the only known system in which, during the low state, two different sub-states are observable: low-soft and low-hard. These two sub-states are distinguishable from their spectral shape. We study the physical process responsible for the spectral change in the low-hard state through an accurate spectral analysis that compares the different spectral shapes during the soft and hard

low modes. We find that the harder component observed in the low-hard state can be interpreted as the tail of the flare emission.

- *Radio Millisecond Pulsars* (RMSPs) represent the last step of the evolutionary scenario of LMXBs.

  Chapter 4 is dedicated to a sub-class of RMSPs, the so called eclipsing binary pulsars. They are systems in which the pulsar is in a tight orbit around a low-mass companion star that is losing mass. The ionized gas lost by the companion absorbs the radiation coming from the neutron star, causing more or less regular eclipses of the pulsar signal. The eclipsing binary pulsars can be divided into two sub-classes: *black widow* (BW) and *redback* (RB) pulsars. BW pulsars are characterized by a very low-mass ($\leqslant 0.1\,M_{\odot}$), semi-degenerate companion star. The companion mass loss is typically driven by the evaporation of the outer layer of the star, caused by the irradiation of the surface by the strong pulsar wind. RB systems have more massive non-degenerate companions (0.1-0.4 $M_{\odot}$) only partially ablated. Both systems are characterised by eclipses of the radio signal, which cover a small fraction ($< 20\%$) of the orbit in the BWs and significant fraction (up to 60%) of the orbit in the RBs.
  Here, we focus on the RB PSR J1048+2339, analysing data acquired simultaneously with Very Large Telescope, Sardinia Radio Telescope, Low-Frequency Array, Galileo telescope and *Swift* satellite. This pulsar shows double-peaked emission lines in the optical spectra, possibly originated in the accretion disc. The multi-wavelength campaign was aimed at unveiling the physical origin of the double-peaked emission lines and mapping the distribution of the material in the system. The Hα Doppler map that we obtained, revealed a significant emission close to the inner Lagrangian point L_1 extending along the free-fall trajectory of the gas. This extended structure close to L_1 is the first direct

1 Introduction

1.1 Pulsar generality

Pulsars (standing for *PULsating stAR*) were discovered serendipitously in 1967 at the Mullard Radio Astronomy Observatory in Cambridge (UK) by a young PhD student, Miss Jocelyn Bell, under the supervision of Professor Antony Hewish from the Cambridge University [Hewish et al., 1968]. Studying the scintillation in the interplanetary medium, at a frequency of 81.5 MHz, they accidentally detected an extremely regular pulsed signal, from an object named CP 1919, repeating every day at the same sidereal time with a period of $\sim$1.3 s.

The physical nature of pulsars was debated after the discovery of CP 1919 [Hewish et al., 1968], nowadays known as PSR B1919+21: Hewish et al. [1968] proposed that the periodic emission of CP 1919 could be produced by the radial oscillations of either a white dwarf (WD) or a neutron star (NS); Burbidge [1968] and Saslaw [1968] suggested that the pulsations might be due to orbital motion of a close binary, whereas Ostriker [1968] hypothesized hot spots on the surface of a rotating WD as the source of emission. Finally, [Pacini, 1967] and Gold [1968] proposed that pulsations were originated by a rotating NS.

After the discovery of Vela [Large et al., 1968] and Crab [Staelin and

Reifenstein, 1968] pulsars, which showed pulse frequencies of $\simeq 11\,\mathrm{Hz}$ and $\simeq 30\,\mathrm{Hz}$, respectively, the WD-based models were ruled out and the identification of pulsars with highly-magnetized, rapidly-rotating NS became generally accepted and also their association with supernova remnants [Gold, 1969].

Pulsars are auto-gravitating objects kept in equilibrium by the degeneracy pressure of the neutrons that mainly constitute them. They combine a numerous of extreme physical conditions: high mean density $\rho \gtrsim 10^{14}$ g cm^{-3}, mass of about 1.4 $M_\odot$ with dimensions comparable to the size of a city ($R \sim 10$ km), high spin rate (typical rotational period P at birth in the range $10^{-3} - 1$ s) and high surface magnetic field ($B \sim 10^{8-14}$ G, for comparison the Sun has a magnetic field of 1 G).

The possibility of the existence of these extremely dense objects was theorized in 1934 by Baade and Zwicky [1934]. They conceived the idea of a NS as a possible product of a supernova explosion. When a massive star approaches the end of its main-sequence lifetime, the light elements in its core are depleted and nuclear burning ceases. The reduced radiation pressure can no longer sustain the star gravitationally, and the core collapses, forming a NS. The outer layers of the star rebound from the solid core and are blown out in a supernova. Colgate and White [1966] predicted that, in the explosion, the conservation of the magnetic flux ($4\pi B_i R_i^2 = 4\pi B_f R_f^2$, where B is the magnetic field and R is the star radius before and after the SN explosion) and the angular momentum ($I_i \Omega_i = I_f \Omega_f$, where I is the moment of inertia and Ω is the angular velocity) would allow the star to retain a strong magnetic field and to reach spin frequencies of tens or hundreds of Hz.

Most pulsars, according to the theory of stellar evolution, are formed by the *core-collapse supernova* explosion (Type II, Type Ib or Type Ic) of massive stars (with masses from 8 to 25 $M_\odot$). During the explosion the star reaches luminosity of $\sim 10^{10}\,L_\odot$. This phase occurs when the star progenitor cannot sustain itself against its own

gravity due to the absence of the radiative pressure generated by nuclear fusion. In fact, the heavy stars ($> 8\,M_{\odot}$) are able to produce iron (^{56}Fe) in the stellar core. The fusion of ^{56}Fe is an endothermic process and then it cannot release energy. As a result, the star collapse is unavoidable since the star is no longer able to counteract its self-gravity. The outer layers of the star are ejected to form the supernova remnant, while the inner core implodes forming a NS.

NSs are believed to be constituted by multiple layers, where the matter has different densities and states. The models of NS inner structure depend on the equation of state, which is still unknown. The first model of the interior of a NS was made by Oppenheimer and Volkoff [1939] and Tolman [1939], who combined the fluid mass and momentum conservation in a Schwarzschild metric [Schwarzschild, 1916] obtaining the *Tolman-Oppenheimer-Volkoff* equation. Present models predict a stratified structure, made of three layers [Shapiro and Teukolsky, 1983, Chamel and Haensel, 2008]:

- **atmosphere**. The atmosphere is a thin ($0.1 - 10\,\mathrm{cm}$) layer constitutes by ionised nuclei and non-degenerate electrons. Its mass is negligible compared to that of NS.

- **crust**. The crust can be divided into an external and an internal part, and comprises about 1% of the stellar mass. The outer crust is make of a crystalline reticule of atomic nuclei embedded in an electron sea. It extends a few hundred meters from the bottom of the atmosphere down region where the neutron drip density reaches values of $\rho_{drip} \sim 4 \times 10^{11}\,\mathrm{g\,cm^{-3}}$. In the inner crust where the neutron drip density $\rho_{drip} \sim 3 \times 10^{14}\,\mathrm{g\,cm^{-3}}$ is reached, a free neutron gas is formed. It is composed of ions and ultra-relativistic, degenerate free electrons.

- **core**. The core is the largest region in the NS and accounts for

99% of the total mass. In the outer core ($\sim$ 10 km) the matter is thought to be in an almost completely neutronized superfluid state. Instead, the inner core of NSs is the densest point of the observable Universe, probably reaching values of about 10^{14-15} g cm^{-3}. Its composition and size is unknown, it has been hypothesised that exotic matter such as hyperons, pions/kaons or free quarks can be found in it.

The pulsar 'standard model'

The presence of a radio pulsar is revealed by a sequence of pulses observed in most cases in the radio band at regular intervals equal to the NS spin period. Due to the misalignment between rotation and magnetic axis, pulsars irradiate radio beams from their magnetic poles, which can be observed in the form of pulse only when the beam intercepts our line of sight. This is the *lighthouse model*, illustrated in Figure 1.1. The pulse shapes are different for each pulsar and can show microstructures on timescales as short as 10 ns. Thanks to this profile each pulsar can be identified univocally.

The physical process underlying the radio pulsar phenomenon is not yet fully understood, but a simplified model can explain some of the observed characteristics. This model was first developed by Goldreich and Julian [1969] and today's version of it is called 'Standard Model' for pulsars. In this model, the fast rotation of NS magnetic field induces an electric field that exerts a strong electric force (much higher than the surface gravitational force) on the NS surface. The electric force rips off the charged particles from the NS surface, forming a dense plasma that surrounds the star. The plasma particles are forced to co-rotate rigidly with the star. The particles, bounded to the magnetic field lines, can co-rotate with the star only up to a distance called *light*

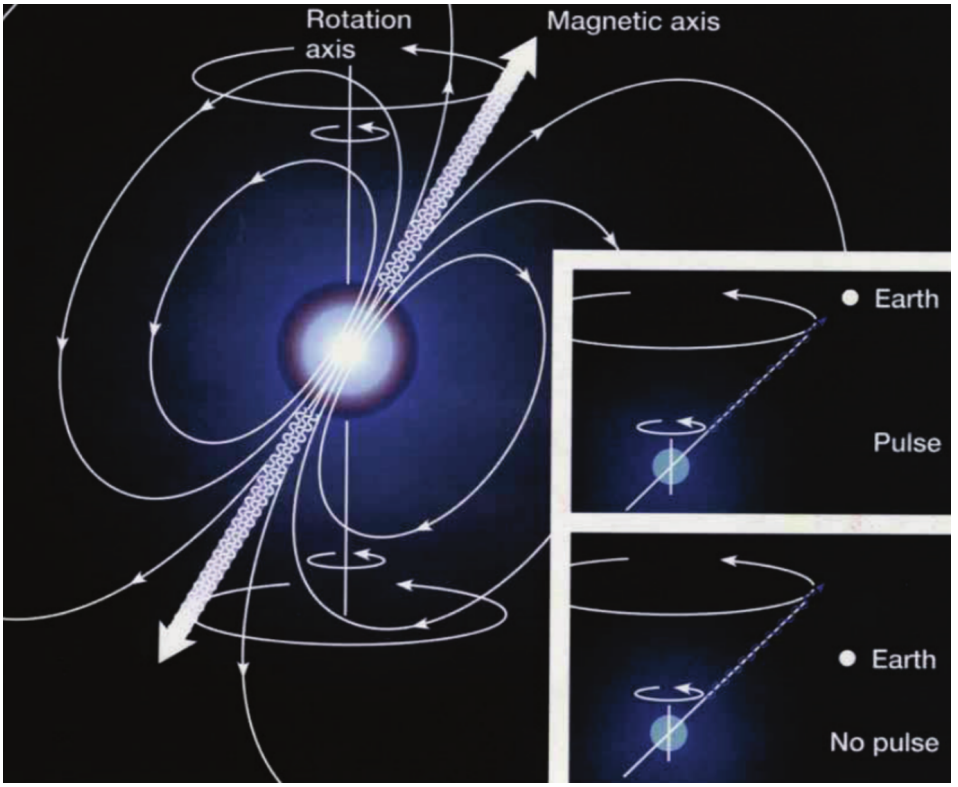

Figure 1.1: Rotating magnetic dipole model of a pulsar with misaligned rotation and magnetic axes. The radiation is concentrated in the cone near the magnetic poles and generates the lighthouse effect (from `https://medium.com/through-the-optic-glass/una-ulx-in-ngc-5907-197f3918742e`.

cylinder radius (r_{lc}):

$$r_{lc} = \frac{cP}{2\pi} \simeq 4.77 \times 10^4 \,\mathrm{km} \left(\frac{P}{\mathrm{s}}\right), \tag{1.1}$$

at which its tangential speed is equal to the speed of light c. The imaginary surface defined by the light cylinder divides the magnetic field lines in two groups: closed field lines that close within r_{lc} and open field lines that do not close (see Figure,1.2). The coherent radiation that we observe in most pulsars is generated in the region called *polar gaps*, defined by the last open field line and centred on the magnetic poles. Here the charged particles are accelerated along the open field lines, producing γ-ray photons either by curvature emission [Ruderman and Sutherland, 1975, Arons, 1983] or by inverse Compton scattering on lower-energy photons [Daugherty and Harding, 1986]. The γ-ray photons, due to the presence of strong magnetic field, can split producing $e^- - e^+$ pairs. This new generation of particles in turn produces curvature radiation at lower energies. As a result, the γ-ray photons produce a pair cascade in the polar gaps, multiplying the initial plasma density by a factor of 10 to 10^4 [Hibschman and Arons, 2001, Arendt and Eilek, 2002]. Finally, the charged particles produce highly collimated beams of radiation in the radio band, visible from the Earth once per rotation of the NS as a *cosmic lighthouse*. The single pulses are extremely regular in time, but their shape typically varies. On the contrary, the integrated pulse profile (i.e. the coherent sum of few hundreds or thousands of pulses) is very stable in time.

Possible emission mechanisms

There are many ways to classify pulsars: by the presence of a companion star, by the values of their rotational period P and derivative of rotation period $\dot{P}$, by their emission energy bands, e.g. radio, optical,

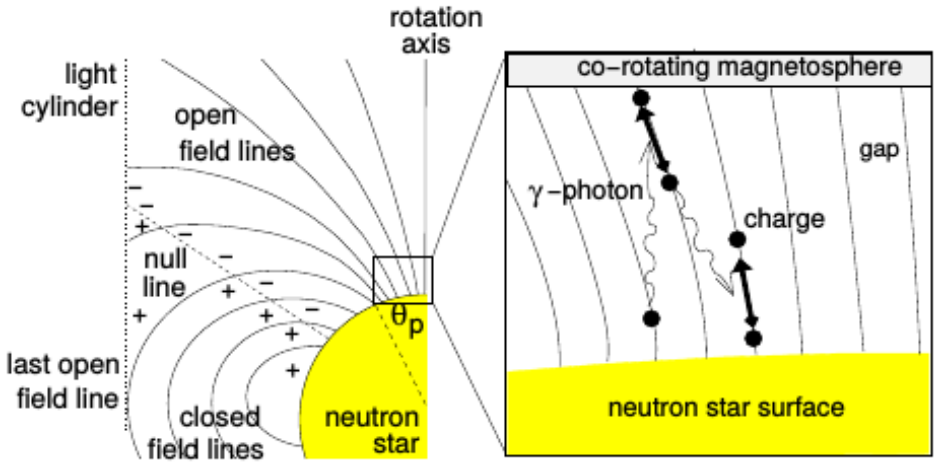

Figure 1.2: Pulsar magnetosphere in the Goldreich–Julian model [Goldreich and Julian, 1969, Lorimer and Kramer, 2004].

X-ray and γ-ray, and also by the main channel powering their emission. Here, we summarize the possible channels responsible for NSs pulsed and un-pulsed emissions:

- **rotation**. The emission of a rotation-powered pulsar is due to the rotation of the electromagnetic dipole. The loss of rotational kinetic energy leads to a deceleration of the NS and therefore to the emission of electromagnetic radiation. Rotation-powered NSs can be observed as pulsars or via radiation propagating through the surrounding nebula. In this second case the radiation arises from the interaction of the pulsar relativistic wind of particle and the nebula. They can be either isolated or located in a binary system.
- **accretion**. Accretion-powered pulsars are part of binary sys-

tems. The emission in this case is powered by the release of gravitational binding energy of matter transferred from the companion star to the NS surface. Accretion-powered emission can be observed only if the NS magnetic field is large enough ($\sim 10^{7-8}$ G) to form a magnetosphere around the NS.

- **nuclear**. The emission of thermonuclear flashes (named type I X-ray bursts) is due to the accumulation of matter on the NS surface. When a sufficient amount of matter is accumulated on the NS surface, critical conditions may cause unstable hydrogen and helium burning. This radiation originates directly from the surface of the accreting NS and occurs only in binary systems.

- **magnetic**. For a particular class of NSs, the magnetars, the emission is powered by the high magnetic field. These magnetic-powered NSs show X-ray luminosities too large for the rotation-powered emission only, and no sign of an ongoing accretion process. Their emission is therefore linked to the instability and decay of their extremely high magnetic field ($\sim 10^{14}$ G).

- **thermal**. The emission of thermally-powered NSs is due to the cooling processes observable for $\sim 10^5$ yr from the NS formation. NSs emit their internal heat, residual of their formation or recovered by accretion processes.

Rotation and accretion-powered mechanisms represent nowadays the two most frequently observed emission channels. These emissions occur at different energies, from radio to γ-ray band. In the next sections both mechanisms will be discussed in order to understand the formation and evolution of binary millisecond pulsars. In Section 1.2 the rotation-powered pulsars are reviewed. The Section 1.3 is dedicated to explore the 'pulsar zoo', focusing in particular on the millisecond pulsars and then on the accretion-powered mechanism that allows for

their formation. This introductory Chapter ends with an overview of the three main evolutionary states that lead to formation of binary millisecond pulsars: *accreting millisecond X-ray pulsars* (Section 1.5), *transitional millisecond pulsars* (Section 1.6) and *eclipsing millisecond pulsars* (Section 1.7).

1.2 Rotation-powered pulsars

The pulsar emission, both in the form of radiation and in the form of relativistic particles, determines a continuous loss of energy and therefore a slow-down. Traditionally, rotation-powered pulsars are associated with radio pulsars because they were first discovered in the radio band and most pulsars are visible in this band. However, most of the energy is emitted at high frequencies (X and γ-ray), while the radio emission only accounts for about 10^{-6} of the overall energy radiated.

Suppose that the NS's magnetic field is purely dipolar, and that the magnetic moment $\mathbf{m}$ of the NS is misaligned with its rotation axis by an angle α (Fig.1.1). A decelerating rotating NS releases energy at the expense of the rotational kinetic energy. The rate of energy loss, also referred to as *spin-down luminosity*, $L_{\rm sd}$, can be obtained simply by taking the time derivative of the rotational kinetic energy:

$$L_{\rm sd} = -I\Omega\dot{\Omega} = 4\pi^2 I \dot{P}\, P^{-3}, \qquad (1.2)$$

where $I = 2/5MR^2$ is the moment of inertia for an homogeneous NS, P is the spin period expressed in s and $\dot{P}$ is its derivative. Assuming a value of I close to $10^{45}\,{\rm g\,cm^2}$, a measurement of P and $\dot{P}$ allows us to find the energy budget available to power the emission, $L_{\rm sd} \simeq 4\times10^{33}\dot{P}_{13}P^{-3}\,{\rm erg\,s^{-1}}$, where $\dot{P}_{13}$ is the spin period derivative in units of 10^{-13}.

From classical electrodynamics it is known that a rotating magnetic dipole emits radiation and its power can be expressed using the Larmor formula as:

$$\dot{E} = \frac{2}{3c^3}|\ddot{\mathbf{m}}|^2 = \frac{2}{3c^3}\frac{1}{4}B^2R^6\Omega^4\sin^2\,\alpha = \frac{1}{6c^3}B^2R^6\Omega^4\sin^2\,\alpha, \qquad (1.3)$$

where $\ddot{\mathbf{m}} = \mathrm{d}^2\mathbf{m}/\mathrm{d}t^2$, $\mathbf{m}$ is the magnetic dipole moment, B is the magnetic field strength at the magnetic pole, R is the NS radius and $\Omega = 2\pi P^{-1}$ is its angular frequency.

In the hypothesis that the NS spin-down is caused only by the varying magnetic moment and the magnetic field is a perfect dipole, we can estimate the age of the pulsar and its magnetic field by equating Equation 1.2 and Equation 1.3:

$$-I\Omega\dot{\Omega} = \frac{1}{6c^3}B^2R^6\Omega^4\sin^2\,\alpha. \qquad (1.4)$$

The equation 1.4 can be generalized using a power law with index n:

$$\dot{\Omega} = -K\Omega^n \qquad \Leftrightarrow \qquad \dot{P} = KP^{(2-n)}, \qquad (1.5)$$

where $K \equiv \dfrac{2m^2\sin^2\alpha}{3Ic^3}$ is a constant. The *braking index* n can be obtained differentiating Equation 1.5 as $n = \dfrac{\Omega\ddot{\Omega}}{\dot{\Omega}^2}$. The braking index is an important parameter because its value depends on the physical processes involved in the emission and probes the pulsar energy loss mechanism. However it is often difficult to measure in practical applications because $\dot{\Omega}$ is either dominated by timing noise or it is to small to be measured.

1.2.1 Characteristic age

From Equation 1.5, written in terms of P and $\dot{P}$, we can estimate the age of the pulsar by measuring the rate of loss of rotational speed

along with its period. Assuming $n \neq 0$, we integrate Equation 1.5 from $t = 0$ (the birth of the pulsar) to the current time τ

$$P^{(n-2)}\mathrm{d}P = K\mathrm{d}t \qquad \Leftrightarrow \qquad \int_{P_0}^{P} P^{(n-2)}\mathrm{d}P = K\int_{0}^{\tau}\mathrm{d}t, \qquad (1.6)$$

where $P_0 \equiv P(t = 0)$ is the pulsar spin period at birth. Solving the integral we find:

$$\tau = \frac{P}{(n-1)\dot{P}}\left[1 - \left(\frac{P_0}{P}\right)^{n-1}\right]. \qquad (1.7)$$

Assuming a spin period at birth much smaller than the current spin period ($P_0 \ll P$) and in the hypothesis that the only source of energy loss is the magnetic dipole emission ($n = 3$), the previous Equation reduces to:

$$\tau_c = \frac{P}{2\dot{P}}. \qquad (1.8)$$

This quantity is called *characteristic age* and it can be taken as an approximation of the pulsar's true age. In some pulsars it is possible to calculate the true age by studying the supernova remnant that surrounds them. In these cases it is useful to compare the two ages in order to determine the braking index and thus investigate the energetics of the source.

1.2.2 Magnetic field

Under the assumption of $n = 3$ (i.e. the case of a purely dipolar magnetic field), we derive from the Equation 1.4 an expression for the magnetic field strength, B_s, at the surface of a NS of radius R [Lorimer

and Kramer, 2004]:

$$B_s = B(r = R) = \left(\frac{3c^3}{8\pi^2}\frac{I}{R^6 sin^2\alpha}\right)^{1/2} (P\dot{P})^{1/2} \simeq 3.2 \times 10^{19}(P\dot{P})^{1/2} G, \tag{1.9}$$

where $\alpha = 90°$, $R \sim 10\,\mathrm{km}$ and $I \simeq 10^{45}\,\mathrm{g\ cm^2}$. This is the *characteristic magnetic field*, and it provides us with a hint about the order of magnitude of the actual field intensity near the surface.
Instead, at a distance r from the NS surface the dipolar magnetic field strength scales as:

$$B(r) \propto \frac{|\mathbf{m}|}{r^3}. \tag{1.10}$$

1.3 Ordinary pulsars, millisecond pulsars and magnetars

To date, according to the Australia Telescope National Facility (ATNF) pulsar catalogue[1], about 2800 rotation-powered pulsars are known and ∼97% of them are seen in the radio band. The rest of the pulsars (∼3%) are observed only at higher frequencies. The poor sample at high energies is due to the fact that most pulsars are too faint for current X-ray and γ-ray telescopes. The diverse zoo of radio pulsar is summarized in Fig. 1.3, the $P - \dot{P}$ diagram (i.e. the evolutionary diagram of radio pulsars). In this diagram, which can be seen as the analogous of the Hertzsprung-Russell diagram for normal stars, we can distinguish five main groups: young and ordinary pulsars in the central region, mildly-recycled and recycled pulsars in the bottom left part and magnetars in the top right corner. These groups of pulsars

[1] `https://www.atnf.csiro.au/research/pulsar/psrcat/`

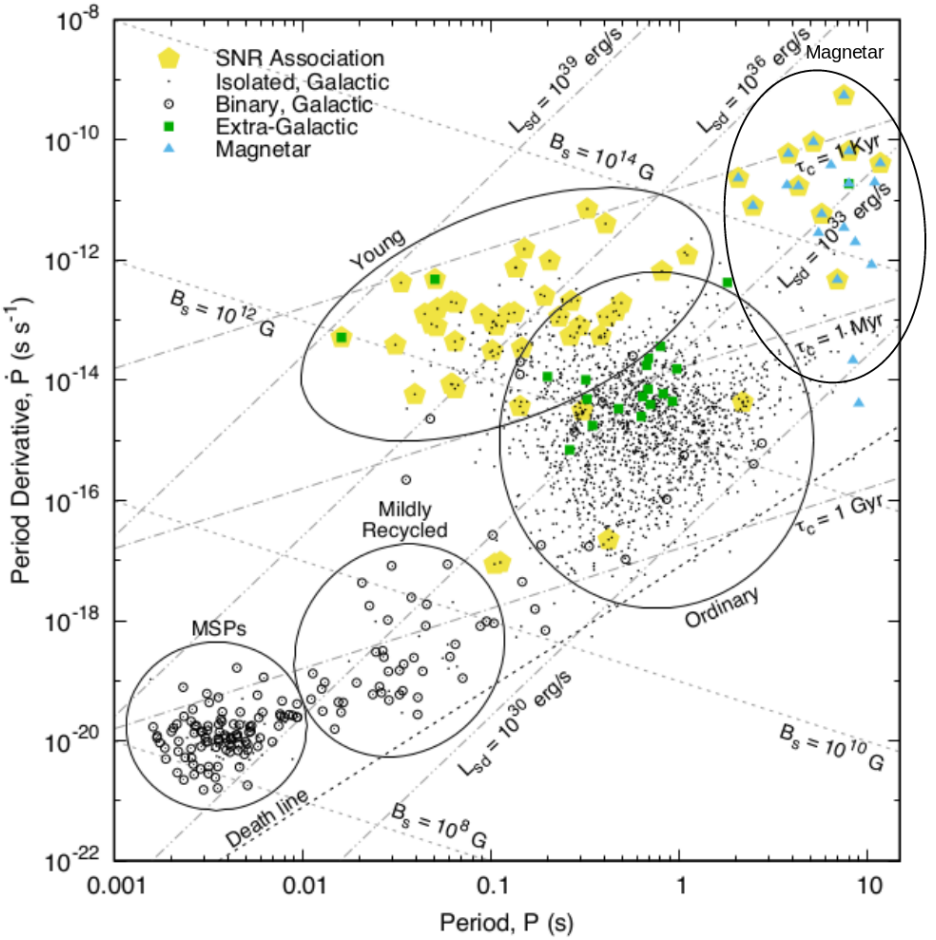

Figure 1.3: $P - \dot{P}$ diagram relative to currently detected radio pulsars ($\sim$2500). We can distinguish three main groups: young-ordinary pulsars in the central region, mildly-recycled and recycled pulsars in the bottom left corner and magnetars in the top right corner. Adapted from A. Ridolfi 2017,Ph.D. Thesis, Univesitaet Bonn.

are distinguished by their value of P and $\dot{P}$, and consequently of B_s and τ_c.

Ordinary pulsars are located around the central region of the $P-\dot{P}$ diagram; they are characterized by relatively long periods ($P \sim 0.01-5\,\mathrm{s}$), high spin-down rate ($\dot{P} \sim 10^{-17}-10^{-12}\,\mathrm{s\,s^{-1}}$) and strong magnetic field ($B \sim 10^{10}-10^{13}\,\mathrm{G}$). These pulsars include both the young pulsars ($\tau_c \lesssim 100$ kyr), resulted from a recent supernova explosion, and the pulsars older with $\tau_c \sim 10^5 - 10^8\,\mathrm{yr}$. The young and ordinary pulsars are concentrated in the Galactic plane, mimicking the distribution of the most massive O-B stars and, thus, confirming their supposed origin from supernova explosions. Ordinary pulsars continue to spin down, until they cross the so called *death-line*, where the radio emission mechanism switches off and pulsars become undetectable.

Millisecond pulsars (MSPs) are a particular class of pulsars spinning extremely fast, up to several hundred of times per second. MSPs are believed to form in binary systems, in which the companion star transfers matter and angular momentum onto the NS surface. During this long phase, the NS is spun-up to very short spin periods (a few ms). The $P - \dot{P}$ diagram shows clearly the distinction between ordinary pulsars and the MSPs, that occupy the bottom left corner of the diagram. MSPs are characterized by short rotational period ($P \sim 0.001 - 0.2\,\mathrm{s}$), low spin-down rate ($\dot{P} \sim 10^{-18} - 10^{-21}\,\mathrm{s\,s^{-1}}$) and relatively low magnetic field ($B \sim 10^7 - 10^9\,\mathrm{G}$). The characteristic age ($\tau_c \propto P/\dot{P}$) of MSPs inferred from observations is $10^{8-9}\,\mathrm{yr}$. They are spatially distributed across higher Galactic latitudes compared to ordinary pulsars and in globular clusters, in fact their long life allows them to move away to greater distances from their birthplace. Another important difference between normal and millisecond pulsars is the presence of a companion: about the 80% of MSPs are in a binary system while less than 1% of all ordinary pulsars are observed orbiting around a companion.

Magnetars (standing for *MAGNETic stARs*) are isolated NS pow-

ered by their extremely high magnetic field ($B \sim 10^{14} - 10^{15}$ G). They are the most magnetic stars in the universe and occupy the top right corner of the $P - \dot{P}$ diagram. The magnetic field decay powers the emission at high energies, particularly in the X-ray and γ-ray bands. The active life of a magnetar is short because their strong magnetic fields decay after about 10^4 years, after which activity and strong X-ray emission cease. To date, we know about 30 magnetars[2].

1.3.1 Millisecond pulsars

The first MSP was discovered in 1982 at Arecibo [Backer et al., 1982]. This NS spins at 642 Hz and has remained the most rapidly spinning NS for a long time. Now, the fastest-spinning NS ever found is PSR J1748–2446ad and has a spin frequency of 716 Hz [Hessels et al., 2006]. MSPs attain such high rotational regimes by accreting matter and angular momentum from a companion star, in a process called *recycling* [Alpar et al., 1982], which can last billions of years. This scenario, usually considered as the evolutionary standard model, assumes that binary MSPs originate in a *core-collapse* supernova.

Another model for the production of binary MSPs relies on the *accretion-induced collapse* (AIC) of an O-Ne-Mg white dwarf [Michel, 1987] (or Type Ia supernova). This scenario has been considered inefficient in literature but [Hurley et al., 2010] showed that the birth rate of binary MSPs via AIC is comparable to the one estimated for the most known core-collapse supernova mechanism. The two evolutionary scenarios for MSPs are briefly reviewed in the following sections.

[2] `http://www.physics.mcgill.ca/~pulsar/magnetar/main.html`

1.3.2 Recycling scenario

The idea of the first discovered MSP belonging to a completely different class of objects than ordinary pulsars was first proposed in [Backer et al., 1982]. After some time, a model explaining the formation of MSPs was formalised in (Alpar et al. 1982, Radhakrishnan and Srinivasan 1982) taking the name of *recycling model*. At their birth NSs spin very fast (tens of milliseconds), then they slow down in a relatively short time scale (high $\dot{P}$) until the radio emission mechanism is no longer efficient and the pulsars switch off.
If the NS is isolated it ends its electromagnetic life in the so-called pulsar graveyard (bottom right part of the $P - \dot{P}$ diagram, Fig. 1.3), if instead it belongs to a binary system it might be re-accelerated. When the pulsar companion expands due to its nuclear evolution, it might fill its Roche lobe, i.e. the last equipotential surface that keeps all the mass gravitationally bound to the star, and starts transferring material through the Lagrangian point or via wind. During this phase, the NS is spun-up to a very short rotational period, few or few tens of milliseconds, depending on the amount of matter accreted, which, in turn, depends on the initial mass of the companion. This process can last up to Gyr period [Tauris et al., 2013].
During this prolonged phase in which the system is observed as a bright X-ray source, the accreted mass ($\sim 0.1 - 0.2\,\mathrm{M}_{\odot}$) likely causes a magnetic decay down to $10^7 - 10^8$ G and a circularization of the orbit. When the mass accretion stops, the NS shines as a radio and/or γ-ray MSP powered by the rotation of its magnetic field. This evolutionary framework is supported by the detection of a few hundreds of radio MSPs in binaries. Moreover, it received strong support from the discovery of coherent X-ray pulsations during type I X-ray bursts first [Strohmayer et al., 1996] and then by the discovery of coherent pulsations during the outburst of (faint) X-ray transients [Wijnands and van der Klis, 1998] (see Section 1.5). Finally, the discovery of

transitional millisecond pulsars (see Section 1.6) brought additional proof of the recycling model.

The initial mass of the companion star and the orbital separation at the time of the NS formation determine different evolutionary paths in the recycling scenario. The relevant evolutionary paths for a NS with high-mass, intermediate-mass and low-mass companions are displayed in Fig.1.4 [Stairs, 2004] and discussed below.

Low-mass X-ray binary systems

In Low-Mass X-ray Binary (LMXB) systems, the companion star with a mass below $\sim 1.5\,M_\odot$ transfers matter via Roche-lobe overflow (see below) onto the NS or the black hole (BH) on long timescale ($10^8 - 10^9$ yr, [Stairs, 2004, Tauris et al., 2013]). The companions are associated with old population II, G-K spectral type, stars. LMXBs are transient systems, that during $\sim 10^9$ years can alternately experience different evolutionary states, from quiescence to accretion and outburst phases. These phases can persist for a few months/years (as in the case of outbursts) or last for 10^4-10^5 years.
During the long accretion process the NSs spin-up to periods as short as few ms [Alpar et al., 1982]. Due to their relatively weak magnetic fields $\sim 10^8 - 10^9$ G, likely resulting from accretion-induced field decay [Taam and van den Heuvel, 1986], LMXBs very rarely pulsate in the X-ray band. The tidal forces on the bloated giant star and the magnetic torques make the system lose additional angular momentum, leading to the circularization of the orbit (path (A) in Fig. 1.4). Once the recycling is complete, the companion star sheds its outer layers to become a He or C-O WD in orbit around a MSP.

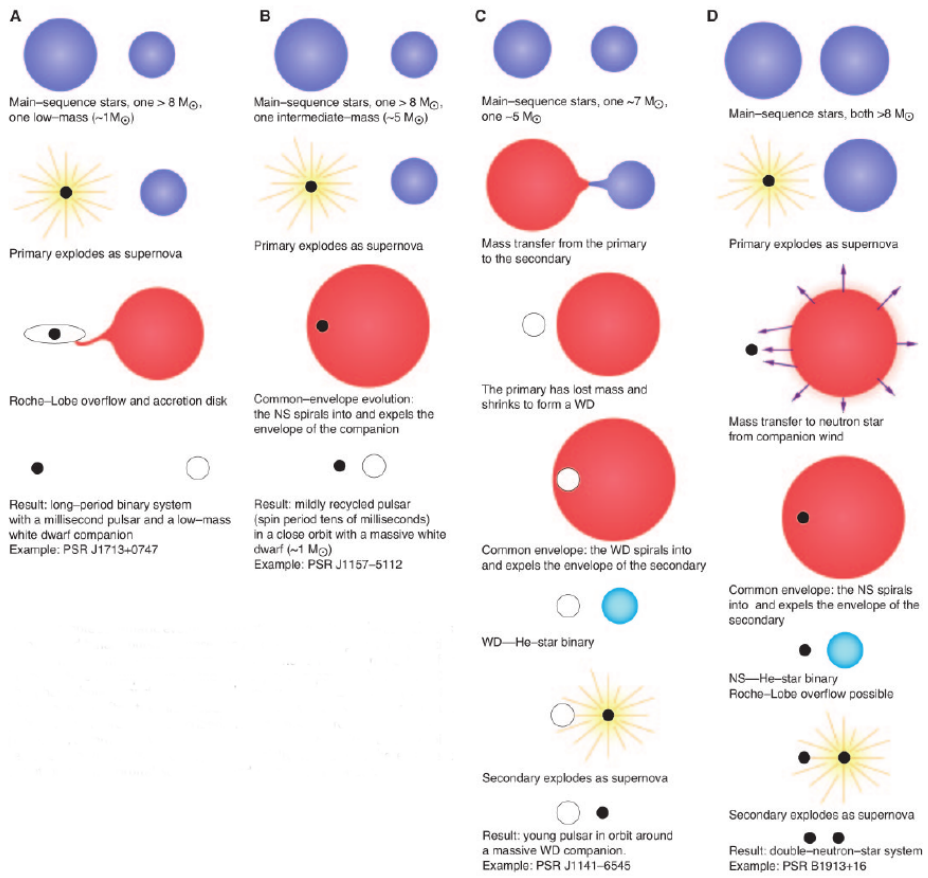

Figure 1.4: Four possible evolutionary scenarios involving binary pulsars with high-mass, intermediate-mass and low-mass companions [Stairs, 2004].

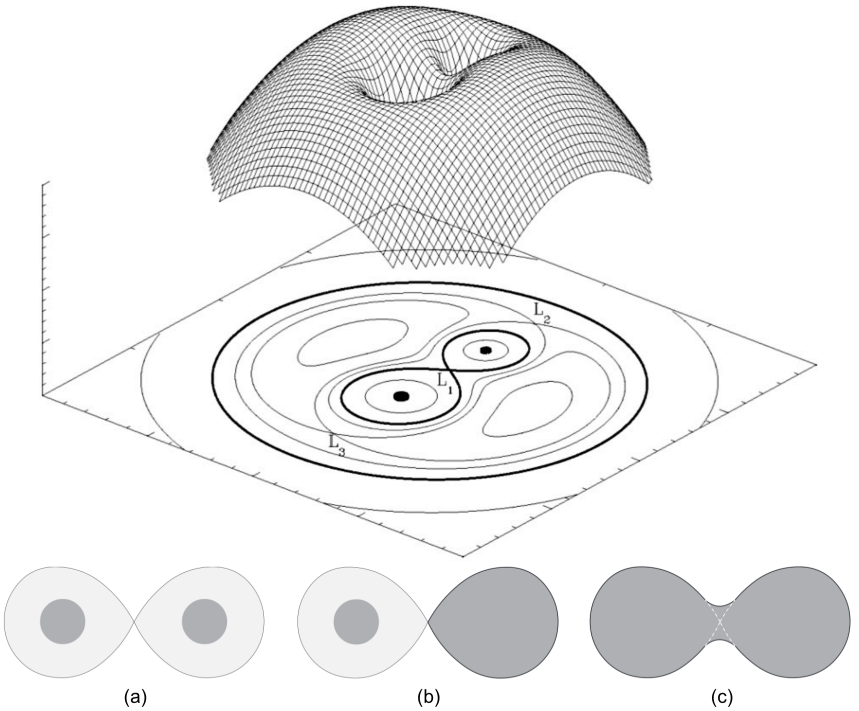

Figure 1.5: Top: 3D representation of the potential energy of a binary system. The black solid lines in the equipotential plot at the bottom of the figure are called the Roche lobes of each star. L_1, L_2 and L_3 are the Lagrangian points where the gravitational forces of the two large bodies cancel out. The mass can flow through the saddle point L_1 from one star to its companion, if the latter fills its Roche lobe (`http://hemel.waarnemen.com/Informatie/Sterren/hoofdstuk6.html`). Bottom: Three possible stable binary configurations are possible: *detached* (a), *semi-detached* (b) and *contact* (c). The semi-detached scenario occurs in the Roche lobe overflow.

Roche lobe overflow

The Roche lobe model, first studied by Edouard Roche in the 19$^{\text{th}}$ century, is based on two auto-gravitating bodies orbiting around a common centre of mass. In Fig. 1.5 a 3D representation of the potential energy of a binary system is shown. We call Roche lobe the region of space around each star within which orbiting material is gravitationally bound to that star (bottom part of the Fig. 1.5). The equivalent radius of the Roche lobe is defined as the radius of a sphere with the same volume, $V_L = 4/3\pi R_L^3$. Its dimension is determined by the mass ratio of the two stars $q = M_2/M_1$ and by the binary separation a, as [Eggleton, 1983]:

$$\frac{R_{L2}}{a} = \frac{0.49q^{2/3}}{0.6q^{2/3} + \ln(1 + q^{1/3})} \tag{1.11}$$

An analogous expression for R_{L1} can be be obtained by replacing q with q^{-1}. There are three possible configurations in which both star are in hydrostatic equilibrium (i.e. the stellar surface coincides with an equipotential surface, see Fig. 1.5):

- *detached binary* in which both stars fill an equipotential surface inside their Roche lobe;
- *semi-detached* in which one of the stars exactly fills its Roche lobe while the other is smaller. The hydrostatic equilibrium is no longer possible near the inner Lagrangian point and then matter must flow through L_1 into the Roche lobe of the companion star. This is exactly what happens during the Roche-lobe overflow;
- *contact binary* occurs when both stars fill their Roche lobe. In this configuration the stars can exchange heat and mass.

In the semi-detached scenario, the transferring matter orbits around M_1 (the NS in our case) due to the high angular momentum, forming

an accretion disc. Viscosity plays a crucial role in the accretion process by removing angular momentum from the matter and allowing it to spiralize inwards. In this process the disc matter is heated up to millions of degrees and, according to Wein's law, emits X-rays. The loss of angular momentum drifts matter inwards into the lowest energy Keplerian orbit with orbital frequency of $\nu_K(r) = 1/2\pi(GM/r^3)^{1/2}$, where M is the mass of the compact object. The Keplerian assumption for the motion of particles is valid if the disc is geometrically thin in its vertical direction [Shakura and Sunyaev, 1973, Ghosh and Lamb, 1978].

Intermediate-mass X-ray binary systems

Intermediate-Mass X-ray Binaries (IMXBs) [Camilo, 1996] are characterized by companion stars with mass in the range 1-10 $\mathrm{M}_\odot$ [Tauris and van den Heuvel, 2006]. The pulsars have longer rotational period (10-200 ms), due to the short-lasting accretion phase (few 1000 yr, Tauris and van den Heuvel [2006]). Like LMXBs, these systems feature mass transfer via Roche lobe overflow from the companion star to the compact object, but the companions are not massive enough to produce wind mass-loss rates high enough to power an observable X-ray source. As a consequence of the fast evolution, the pulsar is only partially spun-up and thus becomes a *mildly recycled* pulsar (see Fig. 1.3). These intermediate-mass pulsars with massive WD companions can be characterized either by low orbital eccentricity (but generally not as low as the results of LMXB evolution) or by larger eccentricity ($e \gtrsim 10^{-3}$), depending on evolutionary path (path (B) or path (C), Fig. 1.4). Following path (B), the systems with initially more massive companions undergoes short-lived and unstable mass transfer during a common-envelope stage. During the common-envelope evolution the NS spirals into the envelope of the companion, becoming somewhat spun up. At the end, the potential energy lost as the or-

bit shrinks allows the pulsar to expel the envelope, leaving a mildly recycled pulsar with a massive companion WD (path (B)) in a low-eccentricity binary with the orbital period of up to a few tens of days [Taam and Sandquist, 2000, Tauris et al., 2000]. Alternatively, a high eccentricity system can be formed when the initially more massive star loses a large amount of mass and forms a WD (path (C)). Then, the initially less massive companion accretes enough mass (through a common envelope phase) that its core is nudged over the Chandrasekhar limit and undergoes a supernova explosion forming a young (non-recycled) pulsar in orbit around a massive WD [Portegies Zwart and Yungelson, 1999].

High-mass X-ray binary systems

High-mass X-ray binaries (HMXBs) are binary systems in which the secondary star is a massive star ($M \gtrsim$ 8-10 $M_\odot$), usually an O or B type and hence they are very young systems (age $< 10^7$ yr). These systems can lead to the formation of double NS binaries in an eccentric orbit like the Hulse-Taylor pulsar (PSR B1913+16, Hulse and Taylor [1975]) and PSR J0737–3039A/B [Burgay et al., 2003, Lyne et al., 2004] (path (D), Fig. 1.4). In these systems both stars are massive enough to explode as a supernova, and if the binary is lucky enough to survive the double explosion, it is able to form a binary system with a recycled pulsar (i.e. PSR J0737–3039A with a 22.7-ms spin period) and an ordinary pulsar (i.e. PSR J0737–3039B with a 2.77-s spin period). After the primary explodes as a supernova, the HMXB system undergoes a common-envelope evolution as the slower evolving star becomes a giant. Then, the NS companion loses its mass via wind or Roche lobe overflow, exposing its helium core [Dewi et al., 2002, Dewi and Pols, 2003]. The timescale of this matter transfer is very short and, consequently, it is hardly detectable. The outcome of this phase is a system consisting of the helium core of the companion and

a NS. If the helium star is more massive than $2.2\,M_\odot$, it collapses and produces a NS; and the system becomes a double NS binary.

The compact objects that undergo the HMXB phase are young NS with high magnetic fields ($\sim 10^{12}$ G). The strong magnetic field is often able to channel the accreting matter along the field lines until it reaches the magnetic polar caps causing X-ray pulsed emission at the NS spin period. The typical pulse periods of HMXBs are between 10–300 s (though the entire observed range spans between 0.069 seconds and 20 minutes) [Tauris and van den Heuvel, 2006]. Among these HMXBs, some host a NS and others a BH.
HMXBs are a heterogeneous class of sources, as they can have both $P_{\rm orb} \leqslant 10$ days with low eccentricity ($e \leqslant 0.1$) and $P_{\rm orb} \simeq$ 20-100 days with $e \simeq$ 0.3-0.5. The 'standard' HMXB systems such as Cen X-3 [Chodil et al., 1967] and SMC X-1 [Leong et al., 1971] are also characterized by regular X-ray eclipses and double-wave ellipsoidal light variations produced by tidally deformed giant or sub-giant companion stars.

1.3.3 Accretion-induced collapse

In the AIC scenario the formation of a MSP can occur during the course of a mass transfer via Roche-lobe overflow, when a WD composed mainly of oxygen and neon with some magnesium reaches the Chandrasekhar limit, and collapses to form a NS [Bhattacharya and van den Heuvel, 1991]. Initially, the system includes two stars in a relatively wide detached binary system, the primary is a main sequence star with mass between 1 to $3.5\,M_\odot$ and its companion is a C-O or O-Ne-Mg WD [Ivanova and Taam, 2004]. The primary star then evolves to overflow its Roche lobe and starts to transfer matter to its now WD companion. The WD accretes matter from the secondary star until it reaches $M_{Ch} = 1.37\,M_\odot$ and then collapses (Type Ia supernovae) [Smedley et al., 2015]. After the WD collapse a low-mass or

intermediate-mass X-ray binary phase can be established, forming a class of object called LMXBs(AIC)/IMXBs(AIC) [Hurley et al., 2010].

1.4 Changing of states in millisecond pulsars

The evolution of MSPs in tight binary systems is governed by the balance between the outward pressure exerted by the pulsar wind on the mass lost by the companion, and the inward gravitational force of the NS. Slight variations in the mass inflow rate from the companion star may lead to different evolutionary states that we will treat in the next three sections.

The ram pressure of the accreting matter in radial free-fall is [Davidson and Ostriker, 1973]:

$$P_{ram} = \rho v^2 \qquad \Rightarrow \qquad P_{ram} = \frac{(2GM_{NS})^{1/2}\dot{M}}{4\pi r^{5/2}}, \tag{1.12}$$

where $v = (2GM_{NS}/r)^{1/2}$ and $\dot{M} = 4\pi r^2 \rho v$ is the mass accretion rate.

The magnetic stress from the NS magnetic field is equal to:

$$P_{mag}(r) = \frac{\mu^2}{8\pi r^6}, \tag{1.13}$$

where $\mu = B_s R^3/2$ is the NS magnetic dipole moment, B_s is the field strength at the magnetic poles of the NS with radius R. Depending on which force prevails and at what distance from the NS the accretion disc is truncated, we can delineate three main possible outcomes (see Fig. 1.6).

The theory of accretion onto magnetized rotating NS defines characteristic radii that enclose regions with different physical properties [Davidson and Ostriker, 1973, Lamb et al., 1973]:

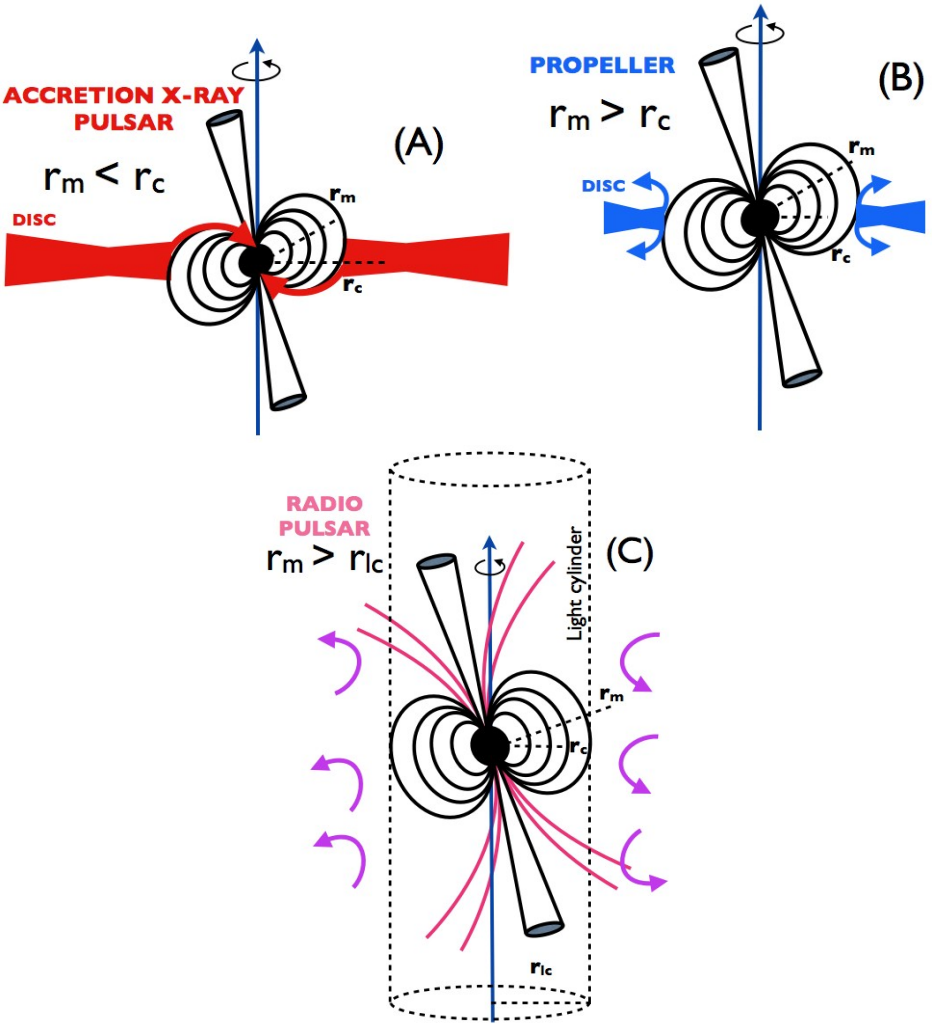

Figure 1.6: Cartoon of the three different regimes of a NS in a binary system for decreasing mass accretion rates (from (A) to (C)). The state depends on the value of the mass accretion rate and then on the dimension of magnetospheric radius (r_m), corotation radius (r_c) and light cylinder radius (r_{lc}).

- *Alfvén radius.* This is the radius at which the star's magnetic field pressure balances the ram pressure of the infalling matter. In spherical symmetry, the theory predicts that this will occur at

$$r_A = \left(\frac{B_s^4 R^{12}}{2GM\dot{M}^2} \right)^{1/7}, \tag{1.14}$$

where G is the gravitational constant [Pringle and Rees, 1972]. In some models [Ghosh and Lamb, 1979] the boundary between the disc and the magnetosphere is expressed through the *magnetospheric radius*:

$$r_m = \xi r_A, \tag{1.15}$$

with $\xi \simeq 0.5$ [Campana et al., 2018].

- *co-rotation radius.* It is the radius at which the pulsar co-rotation velocity is equal to the Keplerian velocity:

$$r_c = \left(\frac{GMP^2}{4\pi^2} \right)^{1/3}. \tag{1.16}$$

- *light cylinder radius* (see Eq. 1.1).

The relative size of these radii determines the state in which the pulsar is found: *accretion-powered*, *propeller* and *rotation-powered*.

During the accretion phase the NS gravitational force prevails (Fig. 1.6, (A)) and the magnetospheric radius (delimiting the inner radius of the disc) is smaller than both the co-rotation radius and the light cylinder radius ($r_m < r_c$). The material flows from the accretion disc down to the magnetospheric radius, where the magnetic stress becomes dominant. The inflow matter penetrates the NS magnetosphere where it is enforced to co-rotate with it. During this phase the rotation-powered pulsar switches off and the NS accretes matter and angular momentum preferentially onto the magnetic polar caps, thus

increasing its spin period [Campana et al., 1998, Burderi et al., 2001]. The accretion onto the NS surface gives rise to X-ray pulsations at the NS spin periods. The total luminosity due to accretion is given by

$$L_{acc}(R) = GM\dot{M}/R, \tag{1.17}$$

that depends on the mass accretion rate $\dot{M}$. Accretion onto the NS continues as long as the centrifugal force exerted by the co-rotating magnetic field lines on the accreting material is weaker than gravity [Illarionov and Sunyaev, 1975, Stella et al., 1986].

If the accretion rate decreases under a certain threshold, the inflowing matter is no longer able to overcome the centrifugal barrier set by the rotating pulsar magnetosphere and the *propeller* regime takes place (Fig. 1.6, (B)). During this phase the magnetospheric radius expands becoming larger than the corotation radius ($r_c < r_m < r_{lc}$), therefore the drag exerted by the NS magnetic field becomes super-Keplerian. The fate of the infalling matter is uncertain and still debated. General relativistic MHD simulations demonstrate that the accretion flow can be stopped by the pulsar wind just beyond the light cylinder, creating a termination shock [Parfrey and Tchekhovskoy, 2017]. Alternatively, the material can accumulate outside the magnetospheric boundary, giving rise to a pressure build-up. If the material accumulates at the magnetospheric boundary more rapidly than the ejection rate, the pressure might push the magnetospheric radius inside the corotation radius, leading to accretion onto the NS surface [Davies and Pringle, 1981, Maraschi et al., 1983].

During the secular evolution, the expansion of the outer layers of donor star can be opposed by the radiation pressure of the accreting NS [Kluzniak et al., 1988] emitting at high energy. In this case the Roche lobe is not filled and the mass accretion stops or strongly decreases. A strong decrease in the mass accretion rate leads the magnetospheric radius to expand beyond the light cylinder radius ($r_m > r_{lc}$).

The pulsar becomes able to sweep away the accreting matter at the inner Lagrangian point. At this point the rotation-powered pulsar is assumed to switch on (Fig. 1.6, (C)).
The discovery of transient systems like accreting millisecond X-ray pulsars [Wijnands and van der Klis, 1998] and transitional millisecond pulsars [Archibald et al., 2010, Papitto et al., 2013], shows that the transition between accretion and rotation-powered states can also occur on short timescales of weeks/months, or even shorter.

1.5 Accreting millisecond X-ray pulsars

Accreting millisecond X-ray pulsars (AMXPs) belong to transient systems in which a NS accretes mass from a low-mass companion star. AMXP systems are a sub class of LMXBs. They spend most of the time in a quiescence state, with X-ray luminosity of order of $10^{31} - 10^{33}\,\mathrm{erg\,s^{-1}}$, and sometimes they show X-ray outburst reaching X-ray luminosity of $10^{36} - 10^{37}\,\mathrm{erg\,s^{-1}}$.
During outbursts, X-ray coherent pulsations are observed with periods in the range 1.1–9.5 ms [Patruno and Watts, 2012, Campana and Di Salvo, 2018]. X-ray and radio pulsations have never been observed in quiescence [Iacolina et al., 2010, Patruno et al., 2017]. Radio pulsation have never been observed also in outburst [Patruno and Watts, 2012].
All of the known AMXPs have donor stars with mass $M \lesssim 1\,M_{\odot}$, that transfer mass via Roche lobe overflow and NSs with weak surface magnetic field ($B \sim 10^{8-9}\,\mathrm{G}$). The gas stripped from the companion is channeled onto the magnetic poles of the rotating NS, giving rise to X-ray pulsations at the NS spin frequency (see Fig. 1.7). At a distance of a few tens of kilometers from the NS, the gas flows almost undisturbed towards the surface. Once the gas reaches the transition region, where the kinetic energy of the free-falling gas becomes comparable to the magnetic energy of the NS magnetosphere, it stops flowing in

Keplerian orbits and starts to co-rotate with the magnetosphere. The gas exchanges angular momentum with the magnetosphere and the NS is spun up. The kinetic energy of the infalling matter is converted in radiation mostly in the X-ray/γ-ray band of the spectrum, originating an accretion luminosity given by Eq. 1.17. Some AMXPs also show millisecond oscillations during thermonuclear bursts that ignite on their surface [Strohmayer et al., 1996].

Tab. 1.1 shows the 19 AMXPs discovered so far [Campana and Di Salvo, 2018]. Despite the few number so far discovered, AMXPs are an heterogeneous class of object with some common features. The recurrence and duration of outbursts varies considerably from one source to another: NGC 6440 X–2 goes into outburst every month for 4-5 days, whereas the longest outburst, from HETE J1900.1–2455, has lasted for $\sim$10 years. All AMXPs show faint luminosity ($\sim 10^{36}\,\mathrm{erg\,s^{-1}}$) during outburst, suggesting low time averaged mass accretion rates, very small donor stars with masses almost always below $0.2\,M_{\odot}$, and relatively short orbital periods with P_b <1 day (see Tab. 1.1). The best studied AMXP, SAX J1808.4–3658, shows regular outbursts occurring every 1.6-3.5 yrs. The latest outburst took place in August 2019 [Goodwin et al., 2019], and it will be object of study in Chapter 2.

These objects play a key role in the theory of evolution of LMXBs and are considered to be the first confirmation of the recycling scenario. This class of sources represent a link between the accretion-powered (LMXBs) and the rotation-powered (MSPs) NSs.

1.6 Transitional millisecond pulsars

Even more than AMXPs, the tight link between NS-LMXBs and radio MSPs has been demonstrated by the discovery of transitional MSPs (tMSPs) [Archibald et al., 2010, Papitto et al., 2013, Bassa et al., 2014]. These sources are considered the 'missing link' between LMXBs

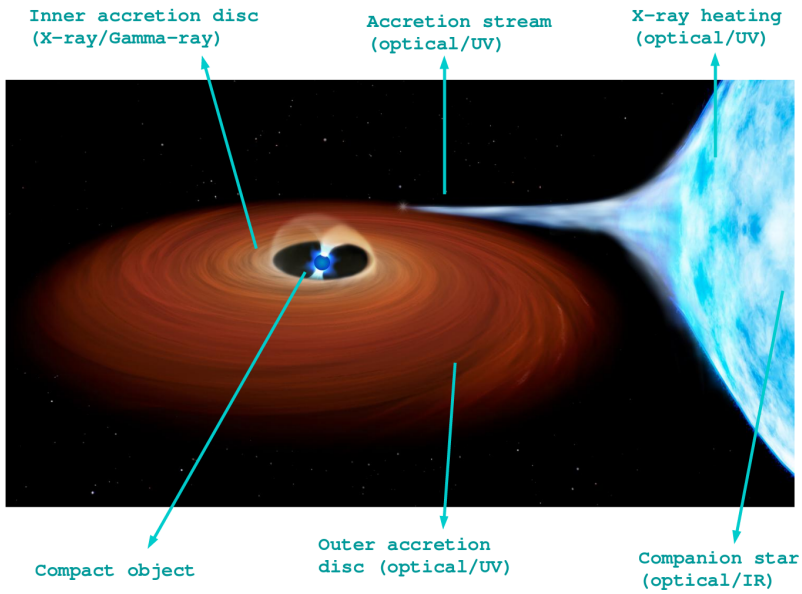

Figure 1.7: Artistic view of an accreting X-ray binary. Adapted from `https://www.nao.ac.jp/en/news/science/2016/20160908-cfca.html`

Table 1.1: Accreting millisecond X-ray pulsar in LMXBs and transitional millisecond pulsars [Campana and Di Salvo, 2018, Sanna et al., 2018a,b].

Source	P [ms]	$P_{\rm orb}$ [hr]	$M_{c,min}$ [$M_\odot$]	Companion Type
Accreting Millisecond Pulsars				
Aql X-1	1.8	18.95	0.56	MS
Swift J1749.4–2807	1.9	8.82	0.59	MS
SAX J1748.9–2021	2.4	8.77	0.1	MS
IGR J17498–2921	2.5	3.84	0.17	MS
XTE J1814–338	3.2	4.27	0.17	MS
IGR J17511–3057	4.1	3.47	0.13	MS
IGR J00291+5934	1.7	2.46	0.039	BD
SAX J1808.4–3658	2.5	2.01	0.043	BD
HETE J1900.1–2455	2.7	1.39	0.016	BD
IGR J17379–3747	2.1	1.9	0.06	BD?
XTE J1751–305	2.3	0.71	0.014	He WD
MAXI J0911–655	2.9	0.74	0.024	He WD?
NGC6440 X–2	4.8	0.95	0.0067	He WD
Swift J1756.9–2508	5.5	0.91	0.007	He WD
IGR J16597–3704	9.5	0.77	0.006	He WD
XTE J0929–314	5.4	0.73	0.0083	C/O WD
XTE J1807–294	5.3	0.67	0.0066	C/O WD
IGR J17062–6143	6.1	0.63	?	C/O WD?
IGR J17591–2342	1.9	8.8	0.42	?
Transitional Millisecond Pulsars				
XSS J12270–4859	1.7	6.91	0.27	MS
PSR J1023+0038	1.7	4.75	0.20	MS
IGR J18245–2452	3.9	11.03	0.17	MS

The companion types are: WD = White Dwarf, BD= Brown Dwarf, MS = Main Sequence, He Core = Helium Star, C/O WD = Carbon-Oxygen White Dwarfs.

and MSPs because they have been observed to switch between accretion and rotation-powered emission on timescales of days/months. During the accretion stage the systems are bright in the X-ray band. When the mass transfer rate decreases, the emission in the radio band, powered by the NS's rotation, becomes predominant (see Fig. 1.8). During the transition the luminosity changes by at least one order of magnitude, due to the variation in mass accretion rate. Today, we have only three firm tMSPs: PSR J1023+0038 [Archibald et al., 2009], IGR J18245–2452 [Papitto et al., 2013] and XSS J12270–4859 [Bassa et al., 2014] (see Tab. 1.1).
All of them lie in tight orbits ($P_b < 1\,\mathrm{day}$) and have a companion star with mass between 0.1 and $0.3\,M_\odot$. tMSPs are characterized by three possible states: X-ray active (or accretion) state, rotation-powered (or radio pulsar) state and accretion outburst. Compared to any other accreting binary systems belonging to LMXBs and AMXPs, these objects show a lower X-ray luminosity ($L_X \approx 10^{33}\,\mathrm{erg\,s^{-1}}$) during the X-ray active state, hence we refer to this state as *sub-luminous* disc state. tMSPs can remain in the sub-luminous disc state for months/years or oscillate back and forth to the radio pulsar state every now and then. In the rotation-powered state, tMSPs behave as *redbacks* (see next section). During this evolutionary phase they are relatively faint at all wavelengths, and most of the information comes from the study of the radio pulsar and its irregular eclipses. Finally, the accretion outburst state has only been observed in IGR J18245–2452 in 2013 [Papitto et al., 2013, Ferrigno et al., 2014]. This outburst lasted $\sim$ three weeks and reached X-ray luminosity of $L_X \simeq 5 \times 10^{36}\,\mathrm{erg\,s^{-1}}$, comparable to some AMXPs. Contrary to the typical behaviour AMXPs, the X-ray light curves of IGR J18245–2452 show an extreme variability during outburst [Ferrigno et al., 2014].

All of the three tMSPs discovered so far (and also the five new tMSP candidates [Bogdanov et al., 2015, Bahramian et al., 2018, Coti Zelati et al., 2019, Li et al., 2020]) show a peculiar behaviour during the

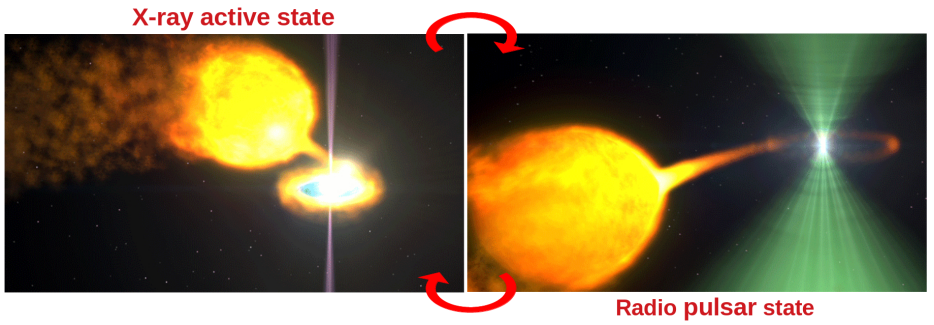

Figure 1.8: Artistic view of a transitional millisecond pulsar. The left panel shows the X-ray active state in which the accretion-powered pulsar is surrounded by the accretion disc. The accretion flow pushes through the pulsar wind and, penetrating the pulsar magnetosphere, gives rise the X-ray pulsations. The right panel shows the rotation-powered radio pulsar state when the mass accretion decreases. During this phase the radio signal is eclipsed by the residual material from the accretion disc and/or by the companion star is losing mass, for a large fraction of the orbit. The transitions between accretion and rotation-powered states can occur on time scales of days/months. Credit: National Aeronautics and Space Administration's Goddard Space Flight Center.

sub-luminous disc state or the outburst state, i.e. a rapid variability between three luminosity modes (see below). This peculiarity allow us to identify strong candidates that will likely perform a transition in the near future. The most efficient way to identify tMSP candidates is searching for optical/X-ray counterparts of unidentified γ-ray sources with peculiar time variability.

PSR J1023+0038

PSR J1023+0038 is the best studied tMSP due to its proximity (1.3 kpc, Deller et al. [2012]) and brightness. Initially known as J102347.6+003841

and nowadays as PSR J1023+0038, it was originally detected as a variable radio source and classified as a peculiar magnetic cataclysmic variable [Bond et al., 2002]. In 2009, the radio pulsar PSR J1023+0038 was discovered and recognised to have been previously surrounded by an accretion disc [Archibald et al., 2009]. The discovery of the radio pulsar showed that the previous classification as a cataclysmic variable (where the compact object is a WD) was incorrect. However, when the radio MSP was found, the system showed no evidence for an accretion disc. A few years later, in June 2013, the source underwent a transition with the disappearance of the radio pulsed signal [Stappers et al., 2014], and an increase by a factor of ∼5 in the GeV flux [Takata et al., 2014]. This state transition from a MSP to a sub-luminous disc state was accompanied by optical brightening with observed double peaked Hα emission lines, signature of an accretion disc [Patruno et al., 2014]. This new state persisted in time and PSR J1023+0038 is still in the sub-luminous disc state (September 2020, see Fig. 1.9). Using the fast optical photometer SiFAP at the Telescopio Nazionale Galileo (TNG), PSR J1023+0038 was recently discovered to be also an optical pulsar [Ambrosino et al., 2017]. This is the first case of a MSP in which pulsed emission in the optical band has been detected.

IGR J18245–2452

IGR J18245−2452 was first detected by INTEGRAL/ISGRI during a bright outburst ($L_X \approx 10^{36}\,\mathrm{erg\,s^{-1}}$) [Eckert et al., 2013]. It is located in the globular cluster M28 at a distance of ∼ 5.5 kpc [Heinke et al., 2013]. In 2013, during the LMXB outburst Papitto et al. [2013] discovered X-ray pulsations at 3.9 ms, modulated by an 11-hr orbital period. Cross-referencing with pulsar catalogue led to the realization that this new AMXP coincided with the known radio MSP PSR J1824–2452I [Bégin, 2006]. IGR J18245−2452 turned into a millisecond radio pulsar two weeks after the end of the outburst, confirming the system as

a tMSPs. Previous serendipitous observations revealed two other outburst episodes in 2008 and 2009 (Linares [2014], Pallanca et al. [2013], see Fig. 1.9).

XSS J12270–4859

XSS J12270–4859 resembles very closely PSR J1023+0038 under many aspects. It was discovered as a hard X-ray source during the Rossi X-ray Timing Explorer (RXTE) survey [Sazonov and Revnivtsev, 2004b]. It remained stable at all wavelengths from the discovery up to the end of 2012, when a decrease in the X-ray flux was observed [Bassa et al., 2014]. The observed decrease of the X-ray flux suggested a transition from an LMXB state to one where the accretion disc is absent and the system shines as a recycled radio MSPs. XSS J12270–4859 is the first binary for which it has been possible to observe the transition from a sub-luminous disc state to a radio pulsar state. The corresponding radio pulsar PSR J1227–4853 was discovered with the Giant Metrewave Radio Telescope (GMRT) at 607 MHz [Roy et al., 2015].

The discovery of the three tMSPs stimulated the search for new candidates. Cross-matching between unidentified *Fermi* LAT gamma-ray sources and spatially coincident hard X-ray variable sources represents a very efficient method to select new candidates, and has led to the identification of a few strong candidates [Papitto and de Martino, 2020]: 3FGL J1544.6–1125 [Bogdanov, 2016], IGR J11098–6457 [Coti Zelati et al., 2019], 4FGL J0407.7–5702 [Miller et al., 2020] and 3FGL J0427.9–6704 [Strader et al., 2016]. Other possible candidates that show some of the tMSPS features are Terzan 5 CX10 [Bahramian et al., 2018], XMM J174457–2850.3 [Degenaar et al., 2014] and a source in NGC 6539 [Bahramian et al., 2020].

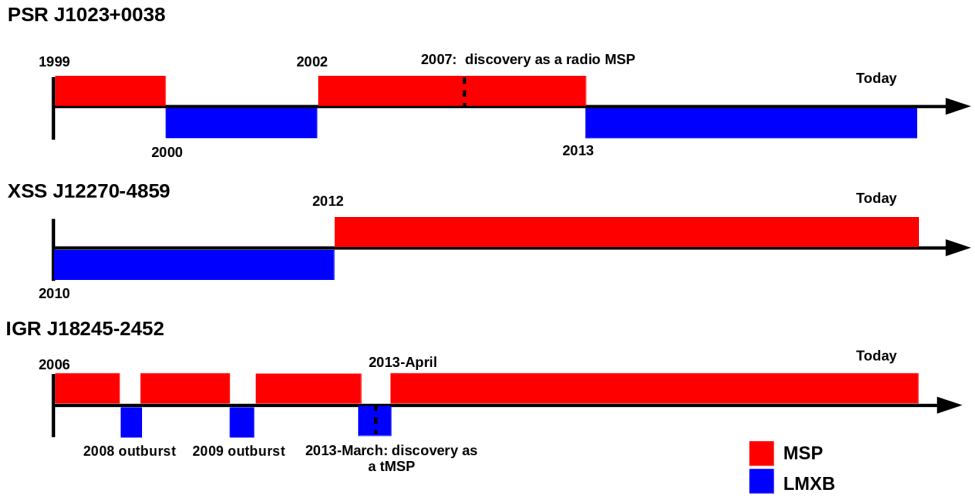

Figure 1.9: Timeline of discoveries and changes of state of tMSPs.

1.6.1 The three modes of tMSPs during the sub-luminous disc state

During the enigmatic sub-luminous disc state, tMSPs show a high luminosity variability over the $\sim 10^{32} - 10^{34}\,\mathrm{erg\,s^{-1}}$ range. The source oscillates between three different luminosity modes [Campana and Di Salvo, 2018]:

- a *high* mode with a 0.3-80 keV luminosity $L_X \sim 7 \times 10^{33}\,\mathrm{erg\,s^{-1}}$. This mode occurs for the 70-80% of the time and it is characterized by X-ray and optical pulsations at the NS spin period with a r.m.s pulsed fraction of ∼8% and ∼1% [Papitto et al., 2019], respectively. This mode can last from a few tens of seconds to a few hours.

- a *low* mode with a 0.3-80 keV luminosity $L_X \sim 3 \times 10^{33}\,\mathrm{erg\,s^{-1}}$. This mode is characterized by a roughly constant luminosity

about one order of magnitude fainter then the *high* mode but a few times brighter than the rotation-powered state ($L_{X,\mathrm{rot}} \sim 8 \times 10^{32}\,\mathrm{erg\,s^{-1}}$). During this mode X-ray and optical pulsations are not detected with a r.m.s upper limit $\lesssim 3.0\%$ and $\lesssim 0.034\%$ (at 3σ c.l.) [Papitto et al., 2013, 2014, 2019], respectively.

- a *flaring* mode during which bright flares occur, reaching luminosity of $\sim (2-7) \times 10^{34}\,\mathrm{erg\,s^{-1}}$. During the flare activity only optical pulsations are detected with a r.m.s pulsed fraction of $0.16 \pm 0.02\%$ [Papitto et al., 2019].

The transition between high, low and flare modes is very rapid (even down to $\sim 10\,\mathrm{s}$) and has been detected simultaneously in the X-ray, UV and optical bands [Coti Zelati et al., 2018, Papitto et al., 2019]. No periodicities or correlations between waiting time are found. Instead, simultaneous radio and X-ray observations of PSR J1023+0038 (the only tMSP currently in the sub-luminous disc state) reveal an anti-correlation pattern of variability [Bogdanov et al., 2018]: the increased radio activity is associated with the X-ray low mode. This phenomenology has been interpreted as due to episodes of low-level accretion onto the NS during the X-ray high mode characterized by rapid ejections of plasma by the active rotation-powered pulsar.
During the sub-luminous disc state, radio pulsations (at 1.4 GHz and 19 GHz) in PSR J1023+0038 have not been detected in either modes (Bogdanov et al. [2015], Papitto et al. in preparation), but this does not imply that the rotation-powered pulsar is not active. The radio signal could be completely absorbed by the disc surrounding the pulsar.

In Chapter 3 we will discuss two different physical scenarios in order to explain the rapid variability between high and low modes.

1.7 Eclipsing millisecond pulsars

The last piece of the puzzle in the evolutionary scenario of binary MSPs is represented by the eclipsing binary MSPs, a sub-class of radio MSPs. These systems are the last evolutionary phase of the recycling scenario, in which the accretion disc disappears and the recycled pulsar switches on.

Eclipsing binary MSPs show long irregular eclipses in the radio signal that last for a large fraction of the orbital period. They are very tight systems (orbital periods of a few hours) with a low-mass companion star that is losing ionized material. This plasma can be driven off from the surface of the companion by high-energy particles produced by the pulsar wind [van den Heuvel and van Paradijs, 1988]. Alternatively, if the companion star fills its Roche lobe the overflowing matter from the companion star can be stopped and blown away by the MSPs radiation pressure at the inner Lagrangian point [Campana et al., 1998, Burderi et al., 2001]. In both cases the interaction between the pulsar wind and the outflow from the donor star can trigger an intrabinary shock emission (see Fig. 1.10). The signature of the intrabinary shock can be detected indirectly in the X-ray light curves, characterized by a double peak orbital modulation [de Martino et al., 2015]. The X-ray modulation is caused by the eclipse of the intrabinary shock emission by the donor. In Chapter 4 we will show a direct evidence of an intrabinary shock emission from the eclipsing binary system PSR J1048+2339. Using the Doppler tomography technique, we identify a shock front between the matter flowing from the Lagrangian point L_1 and the pulsar wind.

The ionized material coming from the donor star can intercept and distort or absorb the NS radiation. Eclipses occur mostly at the inferior conjunction of the donor, when the companion star interposes between the pulsar and the observer. The duration and intensity of

radio eclipses depend on the physical mechanism that determines the disappearance of the pulsed signal, on the observed frequency and on shape and density profile of the outflow. Numerical simulations show that the plasma flow can assume a 'cometary' shape along the orbit due to all the forces present in the system, i.e. gravitational, centrifugal, Coriolis and radiation pressure [Rasio et al., 1989b]. The optical depth of the material is frequency dependent, for instance $\propto \nu^{-2}$ for the electron scattering and $\propto \nu^{-1}$ for cyclotron absorption Thompson et al. [1994], therefore the ionized layers are more transparent at higher frequency. As a consequence, in eclipsing MSPs like PSR J1023+0038 eclipses can last up to ∼60% of the orbit at 350 MHz, ∼25% of the orbit at higher frequencies (1.4 GHz) and they are nearly absent at ∼3 GHz [Archibald et al., 2009, 2013].

There are several mechanisms that can account for the periodic disappearance of the pulsed signal in eclipsing binaries, for instance the dispersion pulse smearing, the Raman scattering and the cyclotron-synchrotron absorption. Observations of PSR J1227–4853 suggest that the eclipses could be due to absorption, rather than scattering, because there is a correlated variation of continuum flux density and mean pulsed flux density at the eclipse boundary [Roy et al., 2015, Broderick et al., 2016].

1.7.1 Black widows and redbacks

The study of eclipsing binary systems started with the discovery of PSR B1957+20, in 1987 [Fruchter et al., 1988]. PSR B1957+20 is a MSP with rotational period of 1.6-ms in orbit around a very low-mass ($\sim 0.002\,M_\odot$) companion. The radio signal of PSR B1957+20 regularly disappears during part ($< 10\%$) of the orbit. After that, many similar systems have been found and classified into two sub-populations [Roberts, 2013]: *black widow* (BW) and *redback* (RB) pulsars. These outlandish names reflect the main feature of these

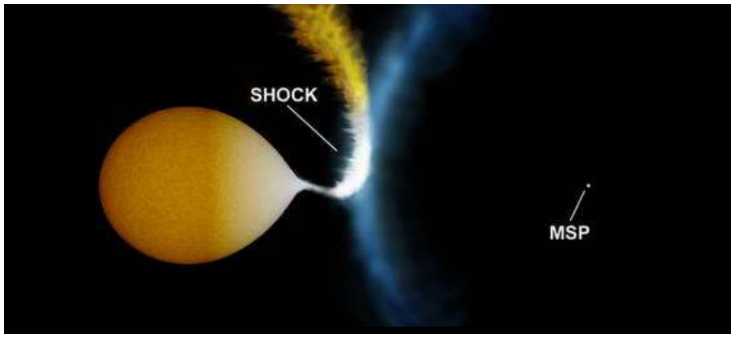

Figure 1.10: Artistic view of an eclipsing binary millisecond pulsar with an intrabinary shock produced by the interaction of the pulsar wind with matter issuing from the inner Lagrangian point or directly onto the donor surface. Credit: NASA/CfA/S.Bogdanov

systems, which is the ongoing ablation of the companion. Indeed, like female spiders kill their partner after mating, this kind of pulsars ablate their companion after being recycled.

BWs and RBs are distinguished mainly by the duration of the eclipses and the mass of the companion star. The distribution of the companion mass in these systems shows a clear bi-modality [Roberts, 2013]. BW pulsars are characterized by a very low-mass ($\ll 0.1\,M_\odot$), semi-degenerate companion star, in which eclipses usually cover a small fraction ($< 20\%$) of the orbit. RB pulsars have a more massive ($\sim$0.1-0.5 $M_\odot$), non-degenerate companion which is filling its Roche lobe. Radio eclipses in RBs typically cover a significant fraction (up to 60%) of the orbit. In both RBs and BWs the eclipse of the radio signal for part of the orbit is due to absorption or scattering by the intrabinary gas produced from the ablation of the companion star irradiated by the pulsar wind.

Most of these 'spiders' were initially found in globular clusters, but in recent years nearly as many have been discovered in the Galactic

plane. The importance of these systems for pulsar astrophysics has been constantly increasing from the discovery of PSR B1957+20. Indeed the existence of BW pulsars might represent a possible answer to the intriguing question concerning the formation of *isolated* MSPs. The majority of MSPs are found in binary systems, nevertheless some 40% of them are isolated. Originally, it was believed that the strong ablation process could eventually make the companion star completely evaporate, forming isolated MSPs. However, recent finding by simulations partially disprove this theory, showing that the evaporation alone cannot be responsible for the formation of most isolated MSPs [Ginzburg and Quataert, 2020a]. Ginzburg and Quataert [2020a,b] propose that the ablation wind coupled to the companions magnetic field is able to remove orbital angular momentum from the binary while maintaining stable the Roche-lobe overflow and thus lead to the total evaporation of the companion star.

The binary properties

The orbit of all RBs and BWs is almost circular ($e < 10^{-5}$) due to the tidal circularization that occurs during the secular LMXB phase. Radio pulsar timing indicates the presence of apparent orbital period variations (of a few seconds) over timescale of weeks/months [Ridolfi et al., 2016, Jaodand et al., 2016b]. This variability on the orbital phase translates into an uncertainty in the epoch of passage at the ascending node and prevents us from predicting the correct orbital phases at a later time, making it difficult to find a phase-connected timing solution. This phenomenon can be ascribed to the exchange of angular momentum between the orbit and the companion star determined by variations in the mass distribution of the companion affecting its quadrupole moment [Applegate and Shaham, 1994, Voisin et al., 2020].

The optical light curves of these systems display a modulation at

the binary orbital period. The shape of the curve gives us precious information about the nature of the companion and the interaction between the latter and the pulsar. When the irradiation by the high energy emission of the pulsar dominates, a sinusoidal single peak modulation with maximum at the pulsar inferior conjunction is seen. Heating of the donor is confirmed by the change in spectral type between inferior and superior conjunction, i.e. the cold ('night') and hot ('day') sides, respectively [Linares et al., 2018]. Alternatively, when we see a double peak at the two orbit quadratures it means that the companion is being deformed by tidal interactions with the NS.

A number of RBs and BWs occasionally show emission line in their optical spectra, despite the absence of accretion disc signatures. Since an increase in the X-ray-to-γ-ray flux is not observed, the emission lines could be ascribed to intrabinary shock emission and/or to material driven off the companion by the pulsar wind. The reason is that the emission features (both single and double peaked) change in both strength and width on short timescales (one orbit or less) [de Martino et al., 2014, Strader et al., 2019].

The X-ray light curve in eclipsing MSPs also show a large amplitude orbital variability, with a maximum at the superior conjunction of the companion star [de Martino et al., 2015], i.e. almost in phase with the optical maximum emission. The X-ray light curve of RBs and BWs can change from quasi-sinusoidal profile to double peaked profile in short timescales. For instance, PSR J1227–4853 and also PSR J1048+23339 displayed variations from single to double and again single-peaked shape over several months [de Martino et al., 2015, Cho et al., 2018]. The modulation of the X-ray light curve probably depends on the location and shape of the intrabinary shock.

2

Accreting millisecond X-ray pulsars

The work presented in this chapter is published in the following article:

- Ambrosino, F.[†]; **Miraval Zanon, A.**[†]; Papitto, A.; Coti Zelati, F.; Camapana, S.; D'Avanzo, P.; Stella L.; Di Salvo T.; Burderi L.; Casella P.; Sanna A.; de Martino D.; Cadelano M.; Ghedina A.; Leone F.; Meddi F.; Cretaro P.; Baglio M.C.; Poretti E.; Mignani R.P.; Torres D.F.; Israel G.L.; Cecconi M.; Russell D.M.; Gonzalez Gomez M.D.; Riverol Rodriguez A.L.; Perez Ventura H.; Hernandez Diaz M.; San Juan J.J.; Bramich D.M.; Lewis F.: *"Optical and ultraviolet pulsed emission from an accreting millisecond X-ray pulsar"*; Nature Astronomy, https://doi.org/10.1038/s41550-021-01308-0

[†] These authors contributed equally to this work

2.1 Optical and ultraviolet pulsed emission from an accreting millisecond pulsar

Millisecond spinning, low magnetic field neutron stars are believed to attain their fast rotation in a 0.1-1 Gyr-long phase during which they accrete matter endowed with angular momentum from a low-mass companion star [Alpar et al., 1982]. Despite extensive searches, coherent periodicities originating from accreting neutron star magnetospheres have been detected only at X-ray energies [Wijnands and van der Klis, 1998] and in $\sim$ 10% of the presently known systems [Campana and Di Salvo, 2018]. Here we report the detection of optical and ultraviolet coherent pulsations at the X-ray period of the transient low mass X-ray binary system SAX J1808.4–3658, during an accretion outburst that occurred in August 2019 [Bult et al., 2019]. At the time of the observations, the pulsar was surrounded by an accretion disc, displayed X-ray pulsations and its luminosity was consistent with magnetically funneled accretion onto the neutron star. Current accretion models fail to account for the luminosity of both optical and ultraviolet pulsations; these instead are likely driven by synchro-curvature radiation [Torres, 2018, Harding et al., 2018] in the pulsar magnetosphere or just outside of it. This interpretation would imply that particle acceleration can take place even when mass accretion is going on, and opens up new perspectives in the study of coherent optical/UV pulsations from fast spinning accreting neutron star in low-mass X-ray binary systems.

Introduction

LMXB systems hosting a weakly magnetic ($\sim 10^8$ G) NS are believed to be the progenitors of millisecond radio pulsars. The evolutionary link between the two classes was first demonstrated through the de-

tection of fast coherent X-ray pulsations generated by accretion onto the NS magnetic poles and the ensuing lighthouse effect in several transient LMXBs [Wijnands and van der Klis, 1998, Chakrabarty and Morgan, 1998]. Definitive proof came with the discovery of a small group of tMSPs which alternate between rotationally-powered and accretion-powered states [Archibald et al., 2009, Papitto et al., 2013].

Fast coherent pulsations and their frequency evolution in accreting NS systems are a tool of fundamental importance to determine binary parameters and accretion torques, investigate the properties of disc-magnetosphere interaction and magnetically funneled accretion, and derive constraints on the equation of state of ultradense matter [Watts et al., 2016]. Through the detection and precise determination of the spin and orbital ephemeris of LMXBs, especially the most luminous and closest ones, it is also possible to carry out *tuned*, increased sensitivity searches for gravitational waves at (twice) the NS rotational frequency.

Fast accretion-powered coherent pulsations have proven elusive: in more than three decades they were detected at X-ray energies in 22 [Wijnands, 2006, Patruno and Watts, 2012, Campana and Di Salvo, 2018, Di Salvo and Sanna, 2020, Papitto and de Martino, 2020] out of ∼190 LMXBs harbouring NSs [Liu et al., 2007], all of which are transient systems attaining peak luminosities of up to a some percent the Eddington limit. So far optical pulsations have been detected only from the transitional millisecond pulsar PSR J1023+0038 [Ambrosino et al., 2017], during an X-ray sub-luminous disc state [Papitto et al., 2019]. Both the X-ray and optical pulsations of this system, which happen almost exactly at unison, are believed to originate from synchrotron radiation in the intrabinary shock just beyond the light cylinder radius, where the wind of relativistic particles ejected by the pulsar meets the accretion disc [Papitto et al., 2019, Veledina et al., 2019, Campana et al., 2019].

The transient X-ray binary SAX J1808.4–3658 (hereafter SAX J1808)

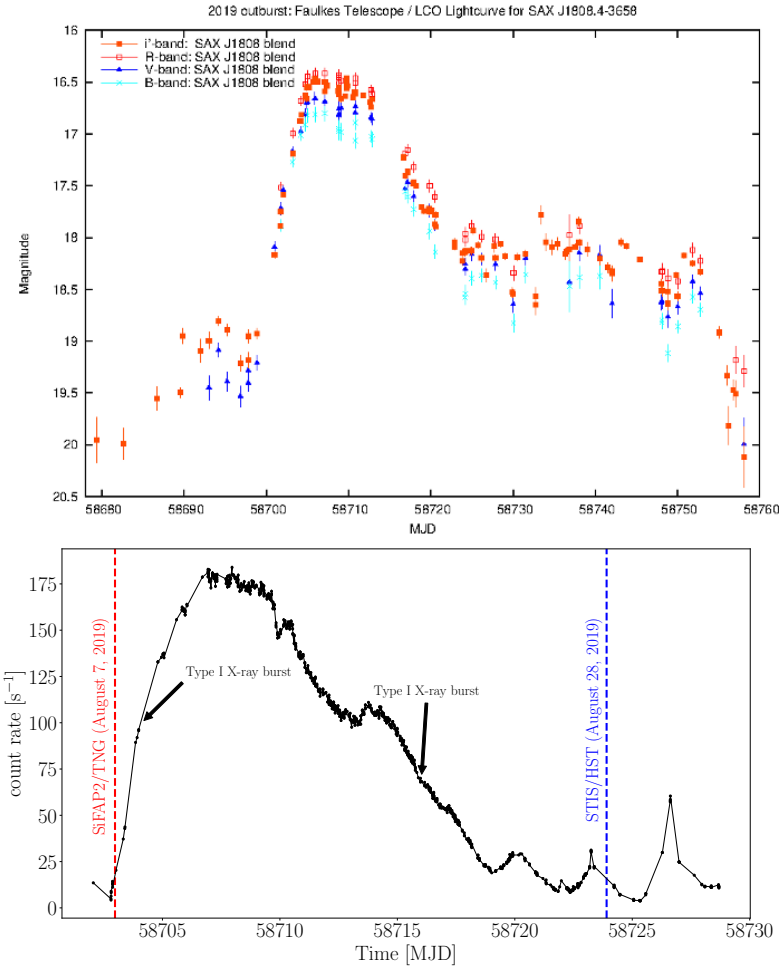

Figure 2.1: *Top panel*: optical light curve of SAX J1808 as observed by *Faulkes Telescope/LCO* from 26 June to 4 October 2019. The source was monitored in four different bands: B, V, R, i'. *Bottom panel*: X-ray light curve of SAX J1808 as observed by *NICER* from 7 August to 31 August 2019. The red and blue dashed lines indicate the epoch of optical and UV observations with TNG/SiFAP2 and HST/STIS, respectively. Intervals including type-I X-ray bursts have been removed from the plot. The epoch of their occurrence is indicated by arrows.

is the first-discovered AMXP[Wijnands and van der Klis, 1998]. SAX J1808 is a NS spinning at a period of 2.49 ms and it is part of a tight binary system with an orbital period of 2.01 h [Chakrabarty and Morgan, 1998]. It is located at a distance of about 3.5 kpc [Galloway and Cumming, 2006] and its companion star has a mass of $0.04^{+0.02}_{-0.01}$ solar masses [Wang et al., 2013]. The system was observed for the first time during an outburst in 1996 using the *BeppoSAX* satellite [in 't Zand et al., 1998] and it was discovered as an AMXP in a subsequent outburst in 1998 [Wijnands and van der Klis, 1998]. Since its discovery in 1996, the source underwent nine ~ 1 month-long outbursts during which the X-ray source luminosity [Gilfanov et al., 1998] reached typically a few $10^{36}\,\mathrm{erg\,s^{-1}}$, starting from a quiescence level [Stella et al., 2000] of $\sim 5 \times 10^{31}\,\mathrm{erg\,s^{-1}}$. The higher mass inflow rate giving rise to the X-ray outbursts causes also an increase in the source ultraviolet (UV) and optical brightness by ~ 4 and ~ 3.5 magnitudes, as a result of enhanced irradiation of the companion star and outer disc regions [Giles et al., 1999] by the X-rays from the inner disc region and the NS [Gilfanov et al., 1998, Gierliński et al., 2002].

This source during outburst shows five phases [Patruno and Watts, 2012](see Fig. 2.1): a fast increase in luminosity lasting few days, a peak, a slow decay, a fast decay and a flaring tail lasting some weeks. The flaring tail has been observed in all outbursts of SAX J1808, but despite this it has no clear explanation within the disc instability model. Indeed, the first four stages of the outburst are typical of several AMXPs.

In Sect. 2.1.1 we describe the discovery of optical and UV pulsation in J1808 during 2019 outburst. In Sect. 2.1.2 we present our data set and the related timing analysis. Sects. 2.1.4 and 2.1.5 are dedicated to the spectral energy distribution and to the discussion of possible physical models that can explain the new phenomenology. In Sect. 2.1.6 we discuss the results and we present future perspectives.

2.1.1 Optical and ultraviolet pulsations

In the summer of 2019, SAX J1808 underwent another outburst [Bult et al., 2019], attaining a peak 0.5–10 keV luminosity of $\sim 10^{36}\,\mathrm{erg\,s^{-1}}$ on August 12, after a ~ 5 day rise. A decay followed and, starting from August 24, $\sim 4-5$ day-long luminosity oscillations took place between $\sim 10^{34}$ and $\sim 10^{35}\,\mathrm{erg\,s^{-1}}$.

Repeated observations with the X-ray Timing Instrument (XTI) on board the *Neutron Star Interior Composition Explorer* (NICER) closely monitored the evolution of the outburst and X-ray pulsations (see Fig. 2.1 bottom panel), yielding refined measurements of the NS spin period and orbital parameters (see Sect. 2.1.3 and [Bult et al., 2019]). On August 7, during the rising phase of the outburst when the X-ray luminosity was $\sim 6\times10^{34}\,\mathrm{erg\,s^{-1}}$, we observed the source for $\sim$ 1 hr with the Silicon Fast Astronomical Photometer (SiFAP2)Ambrosino et al. [2017], operating in the 320–900 nm band and mounted at the *Telescopio Nazionale Galileo* (TNG) in La Palma. A ∼2 ks observation was carried out on August 28 with the Space Telescope Imaging Spectrograph (STIS), operating in $165-310$ nm UV band, on board the *Hubble Space Telescope* (HST), when the X-ray luminosity was $\sim 3.4\times10^{34}\,\mathrm{erg\,s^{-1}}$ in the final oscillating stages of the outburst (see Fig. 2.1 bottom panel).

The Fourier power density spectra of the high timing resolution optical and UV light curves are shown in Fig. 2.2. In both cases, a narrow peak is present at the ~ 401 Hz spin frequency of the NS, with a probability of random occurrence in a single frequency bin of 5.1×10^{-8} and 2.3×10^{-6} in the optical and UV data, respectively.

The optical and UV pulsed light curves folded at the X-ray spin period reported in Table 2.1 and displaying a single-peaked quasi-sinusoidal profile are shown as insets in Fig. 2.2.

The background-subtracted rms amplitude of the optical pulsations was $(0.55\pm0.06)\%$, corresponding to $L_{pulsed(opt)} \simeq 2.7\times10^{31}\,\mathrm{erg\,s^{-1}}$

Table 2.1: X-ray, UV and optical ephemeris of SAX J1808.4−3658 during the August 2019 outburst.

Parameter	X-ray	Ultraviolet	Optical
Right Ascension (α, J2000)	$18^{\rm h}\ 08^{\rm m}\ 27^{\rm s}.62$	–	–
Declination[a] (δ, J2000)	$-36^\circ\ 58'\ 43.3''$	–	–
Validity Range [MJD]	58702–58726		
Reference epoch T_{ref} [MJD]	58715.0	–	–
Time System	TDB	TDB	TDB
Planetary ephemeris	DE405	DE200	DE405
Spin frequency ($\nu(T_{ref})$) [Hz]	400.97520966(1)	–	–
Spin frequency ($\nu(T_{TNG})$) [Hz]	400.97521018(8)	–	400.975225(72)
Spin frequency ($\nu(T_{HST})$) [Hz]	400.97520962(4)	400.97517(10)	–
Spin frequency first derivative ($\dot{\nu}$) [Hz s^{-1}]	$-(2.42 \pm 0.25) \times 10^{-13}$	–	–
Spin frequency second derivative ($\ddot{\nu}$) [Hz s^{-2}]	$(4.9 \pm 1.3) \times 10^{-19}$	–	–
Orbital period (P_b) [s]	7249.1572(14)	–	–
Time of ascending node ($T_{\rm asc}$) [MJD]	58715.022098(3)	–	–
Projected semi-major axis [lt-s]	0.062810(4)	–	–
χ^2/d.o.f	550/378	–	–

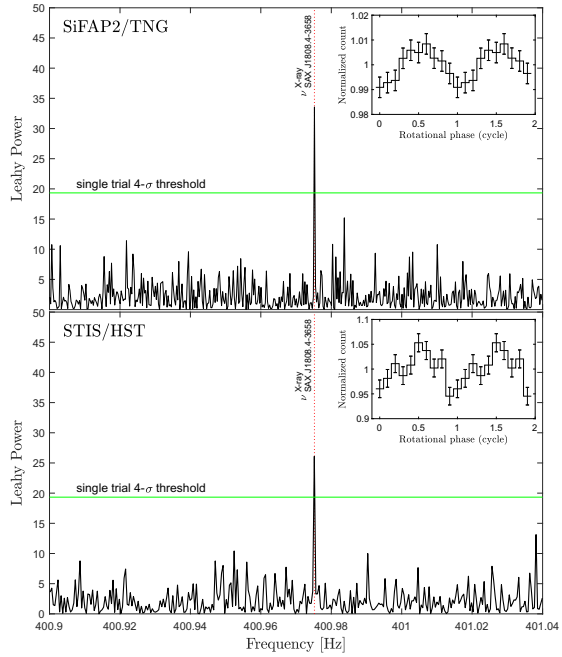

Figure 2.2: Detection and shape of coherent optical and ultraviolet signals from SAX J1808.4−3658. Upper panel: Fourier power density spectrum of the optical (320–900 nm) light curve from the 3.3 ks observation carried out with the SiFAP2 photometer mounted at the TNG, starting on August 7, 2019 at 22:31 (UTC). Once corrected for the systematic drift of the SiFAP2 system clock, photon arrival times were converted to the Solar System Barycentre (SSB) and then corrected for the pulsar orbital motion using the X-ray ephemeris reported in Table2.1. The light curve was binned at 100 μs, corresponding to a Nyquist frequency of 5 kHz. Lower panel: Fourier power density spectrum over the same frequency range from the ultraviolet (165–310 nm) light curve collected with STIS on board HST during a 2.2 ks observation starting on August 28, 2019 at 21:47 UTC. UV photon arrival times were first processed with the *ODELAYTIME* task to shift them to the SSB, and then corrected for the pulsar orbital motion using the same X-ray ephemeris reported in Table2.1. The light curve was rebinned to 500 μs, yielding a Nyquist frequency of 1 kHz. The dotted red vertical line marks the spin frequency of SAX J1808.4−3658 from the X-ray ephemeris, whose uncertainty on the spin frequency is small enough that only a single trial frequency has to be examined. The highest peaks in both panels coincide with this frequency, to within their Fourier resolution. The green horizontal lines mark the power level corresponding to a probability of 6.3×10^{-5} (4-σ) of being exceeded by white noise in a single frequency bin. The insets show the background-subtracted, normalised pulse profiles obtained by folding the optical and UV light curves at the X-ray period (Table2.1), two cycles are plotted for clarity. Phases refer to the reference epoch of the SiFAP2 and STIS observations, respectively; errors bars are 1-σ.

(the total 325–690 nm optical luminosity was $L_{opt} \approx 5 \times 10^{33}\,\mathrm{erg\,s^{-1}}$). In the XTI/NICER observations that covered the epoch of the SiFAP2/TNG observation, the X-ray pulsations had a ~ 9 times larger rms amplitude (4.8±0.3%), and a factor ~ 100 higher luminosity, $L_{pulsed(X)} \approx 2.3 \times 10^{33}\,\mathrm{erg\,s^{-1}}$, than the optical pulsations. Interestingly, the optical pulsation profile was shifted in phase by $\Delta\phi = 0.55 \pm 0.02$ (or $\Delta\tau = 1.38 \pm 0.06$ ms in time; see Fig. 2.3) with respect to that in the X-rays, that is, virtually in anti-phase. We note that PSR J1023+0038 does not show such feature being its optical and X-ray pulse profiles almost in phase (time lag of $\sim 200\,\mu$s) [Papitto et al., 2019].

The UV coherent pulsations detected during the STIS/HST observation were (relatively) stronger than the optical pulsations from 3 weeks earlier: their (2.6±0.7)% rms amplitude led to a pulsed 165–310 nm luminosity of $L_{pulsed(UV)} = 0.026\ L_{UV} \approx 2 \times 10^{32}\,\mathrm{erg\,s^{-1}}$. Correspondingly, the X-ray pulsations detected during the NICER observation carried out a few hours later had a (5.7±0.9)% rms amplitude, and involved a factor of ~ 10 higher pulsed X-ray luminosity of $L_{pulsed(X)} \approx 1.9 \times 10^{33}\,\mathrm{erg\,s^{-1}}$. Owing to the large uncertainties on the absolute timing of the HST data (~ 1 s [1]) the relative phasing of the UV and X-ray profiles could not be determined.

The presence of type I X-ray bursting activity as well as X-ray luminosities exceeding the spin-down power measured in quiescence [Bult et al., 2019] ($1.6 \times 10^{34}\,\mathrm{erg\,s^{-1}}$) by up to two orders of magnitude testify that the outbursts of SAX J1808 are powered by mass accretion.

Also at the time of the SiFAP2/TNG and STIS/HST observations, the X-ray luminosity was higher than the spin-down power by a factor of ~ 2 and 4 (though the pulsed X-ray luminosity was lower). Moreover the source X-ray spectral and timing properties evolved moderately and continuously across the luminosity swing of the outburst (as well as that of previous outbursts) down to $\sim 10^{34}\,\mathrm{erg\,s^{-1}}$ without

[1] HST helpdesk private communication.

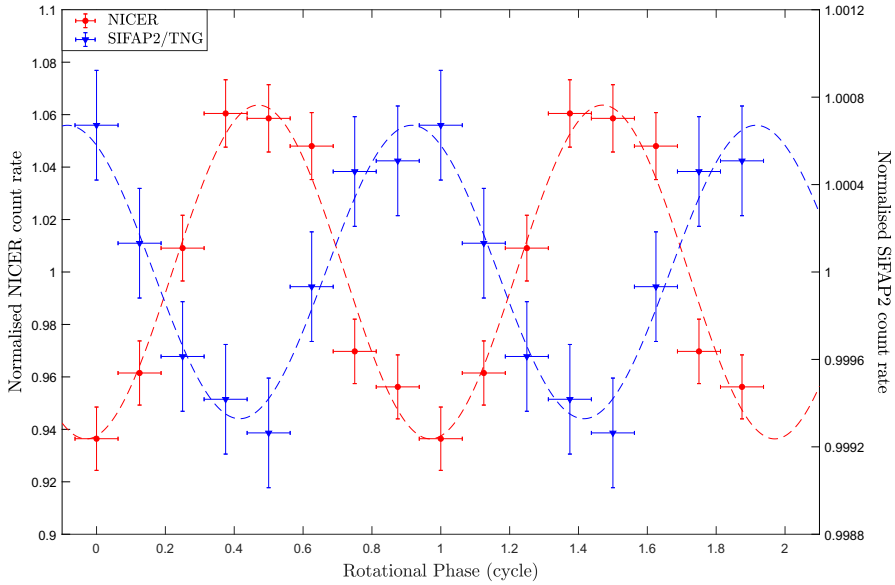

Figure 2.3: Pulse profiles of SAX J1808.4–3658 in the X-ray (red) and optical (blue) bands (note the different scale used). Light curves were folded using the timing solution reported in Table 2.1. The phase shift between the two curves is $\Delta\phi = (0.554 \pm 0.023)$, corresponding to a time lag of $\tau = (1.385 \pm 0.057)$ ms.

displaying any evidence for transitions to a non-accreting regime [Bult et al., 2019] .

The X-ray pulsations were likely generated by funneled accretion onto the magnetic pole. Therefore, we conclude that the SAX J1808 optical/UV pulsations detected nearly simultaneously with the X-ray pulsations are thus the first detected certainly during the accretion phase of a millisecond spinning NS. In Sect. 2.1.5 we discuss their possible origin.

2.1.2 Observations and data reduction

Optical observation

The optical dataset of SAX J1808 was collected with the Silicon Fast Astronomical Photometer (SiFAP2 [Ghedina et al., 2018], TNG Director Discretionary Time, PI Papitto) mounted at the Nasmyth A focus of the INAF 3.58 m Telescopio Nazionale Galileo (TNG), located on the Roque de los Muchachos Observatory in La Palma (Canary Islands, Spain). SiFAP2, the upgraded version of SiFAP [Meddi et al., 2012, Ambrosino et al., 2016], is a two-channel ultra-fast photometer operating in the optical band (320–900 nm) capable to tag the Time of Arrival (ToA) of individual photons with a time resolution of 8 ns.

The absolute timing is provided by a commercial Global Positioning System (GPS) unit via the Pulse Per Second (PPS) signal with a nominal 25 ns accuracy on the Universal Time Coordinated (UTC) worsened to less than 60 μs because of the SiFAP2 electronics transfer function. This value was obtained from observations performed on the Crab pulsar for calibration purposes [Papitto et al., 2019]. We carried out a single 3.3 ks observation of SAX J1808 starting on August 7, 2019 at 22:31 (UTC), during the earliest stage of the outburst. The optical light curve of the source collected with SiFAP2 is shown in Fig. 2.4.

No filter was used during our run. The telescope elevation above the horizon was ~ 24 deg corresponding to an airmass of ~ 2.5, while seeing conditions varied within the range from 0.5 up to 0.9 arcsec (at the Zenith). The Moon was at an angular distance of 47 deg from the target, increasing the background contribution by $\sim 70\%$. During the acquisition, we also measured the sky background signal (taking into account also a dark count rate of $1.8 \times 10^3\,\mathrm{s}^{-1}$ for the sensors) by moving the telescope 10 arcsec away from the target towards the east direction twice during the observation, for about 30 s each time. We obtained an average count rate of $\mathrm{BKG}_{TNG} = 34953 \pm 86\,\mathrm{s}^{-1}$, representing a contribution of more than 90% of the total count rate ($\mathrm{R}_{TNG} = 38560.6 \pm 6.5\ \mathrm{s}^{-1}$) collected by pointing the telescope in the direction of SAX J1808. A reference star, TYC 7403−655−1 (RA = 18:07:56.38, DEC = −36:55:07.35, $V = 12.19$ mag) located 432 arcsec away from SAX J1808 was also simultaneously observed to monitor the atmospheric variations as well as to verify the absence of spurious periodic signals due to instrumental noise at the pulsar spin frequency. As it occurred also in previous observing runs, the SiFAP2 clock drifted by $\Delta t = 5.2$ ms with respect to the time measured by two Global Positioning System (GPS) pulse-per-second signals used to mark the beginning and the end of the observation. We corrected the arrival times assuming that the drift evolved following a linear function of time. This procedure already proved to be efficient in recovering the pulse frequency of both the Crab pulsar and the millisecond pulsar PSR J1023+0038 [Ambrosino et al., 2017, Papitto et al., 2019]. Laboratory tests showed that the thermal jitter of the SiFAP2 system clock could be safely neglected because its relative uncertainty for ms spin periods is several tens of times smaller than our measurements [Ambrosino et al., 2017]. The photon arrival times obtained in this way were then referred to the Solar System Barycenter (TDB time system) using the position of the optical counterpart provided by Hartman et al. [2008] and the geocentric location of the TNG (X =

5327447.4810 m, Y = −1719594.9272 m, Z = 3051174.6663 m), along with the JPL DE405 ephemeris.

Ultraviolet observation

We observed SAX J1808 with the Space Telescope Imaging Spectrograph (STIS, GO/DD-15987, PI Miraval Zanon) on board the Hubble Space Telescope (HST) starting on 28 August 2019 at 21:47 (UTC) during the latest stage of the outburst. The UV light curve of the source acquired with STIS is shown in Fig. 2.4. The spectroscopic observation was performed in *TIME-TAG* mode with 125 μs time resolution for about 2.2 ks by means of the NUV-MAMA detector. We used the G230L grating equipped with a 52×0.2 arcsec slit ensuring a spectral resolution of R∼500 over the nominal range (first order). The total count rate collected by the instrument was T_{HST} = 2016.74±0.95 s^{-1}, with a background contribution of about 30% (BKG_{HST} = 653.36±0.54 s^{-1}). The background signal was estimated by selecting photons in the STIS slit channels outside the source region and averaging them. The resulting value was then normalised to the total number of slit channels.

X-ray observations

The X-ray Timing Instrument [Gendreau et al., 2016] (XTI) on board the *Neutron Star Interior Composition Explorer* [Gendreau and Arzoumanian, 2017] (NICER) observed the SAX J1808 outburst [Bult et al., 2019] from 30 July until 16 September 2019 for a total exposure time of 387.7 ks. The events across the 0.2–12 keV band were processed and screened using HEASOFT version 6.28 and NICERDAS version 7a. We applied standard cleaning and filtering criteria, selecting only the time intervals during which the pointing offset from the nominal source position was smaller than 0.015 deg, the source was

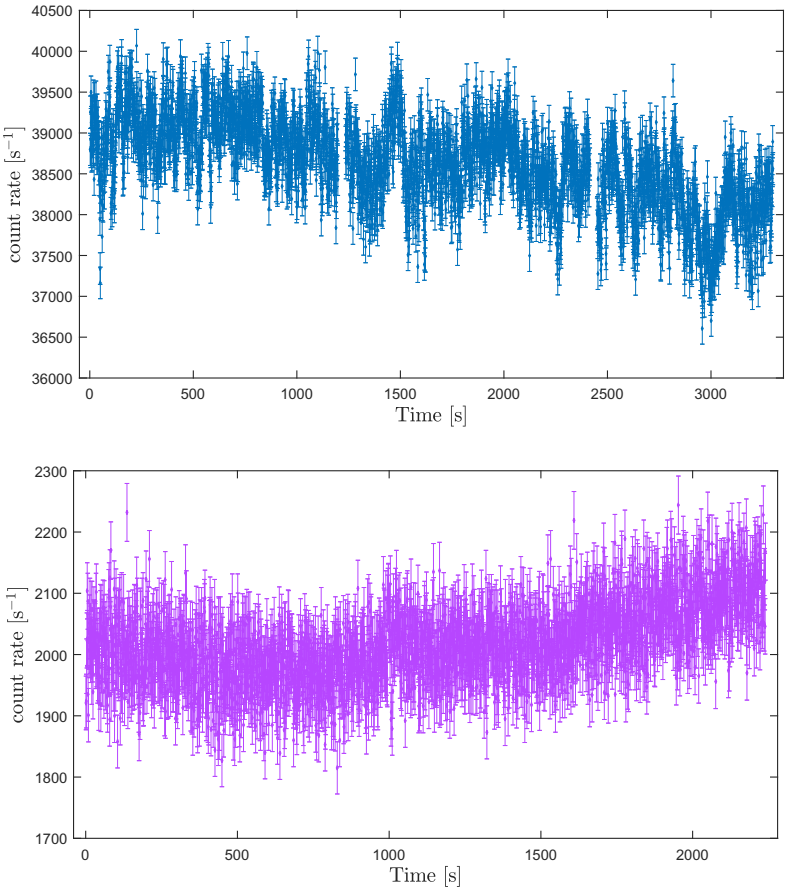

Figure 2.4: *Top*: Light curve of SAX J1808.4−3658 acquired with SiFAP2 on August 7, 2019 during a total exposure time of 3.3 ks. The time on the x-axis represents the elapsed time since 58702.9382176 MJD(UTC). The orbital phase interval is 0.04–0.49. *Bottom*: Light curve of SAX J1808.4−3658 acquired with STIS on August 28, 2019 during a total exposure time of 2.2 ks. The time on the x-axis represents the elapsed time since 58723.9080081 MJD(UTC). The observed orbital phase interval is -0.06–0.25. Both light curves are plotted with a bin time of 1 s; error bars are 1-σ.

at least 30 deg away from the Earth limb (at least 40 deg in the case of a Sun-illuminated Earth) and the International Space Station was outside the South Atlantic Anomaly. The photon arrival times were corrected for the motion in the Solar System barycentre (TDB time system) using the position of the optical counterpart [Hartman et al., 2008] and JPL DE405 ephemeris. The X-ray light curve of the source outburst from 2019, August 7 to August 31 is shown in Fig. 2.1. We removed Type-I X-ray bursts occurred in the time intervals 58704.81059-58704.81186 MJD and 58716.08876-58716.09104 MJD.

2.1.3 Timing analysis.

We measured the X-ray pulsar spin and orbital parameters by analysing the observations performed by NICER between August 7 and 31 (i.e., MJD 58702–58726). We corrected the arrival times using the orbital parameters previously measured [Bult et al., 2019]. We folded 1 ks-long segments of NICER data in 16 phase bins around a preliminary estimate of the pulse period [Bult et al., 2019]. We fitted the pulse profiles with a single sinusoidal component, modeled the evolution of the pulse phases with a function composed of a third-order polynomial and terms resulting from corrections to the orbital parameters (see, e.g. [Papitto et al., 2011]), and obtained the timing solution listed in Table 2.1, characterized by a χ^2 of 550 for 378 degrees of freedom, indicating a formally unacceptable fit.However, even adopting higher-order polynomials, the fit quality did not improve significantly. No trend is apparent in the residuals shown in the bottom panel of Fig. 2.5, and we attribute the high fit reduced χ^2 to the phase timing noise that is known to affect the phases observed from this and other AMXPs [Patruno and Watts, 2021]. The X-ray timing solution derived here is only aimed at performing a search for optical/UV pulses, and modelling such a timing noise component is beyond the scope of this paper. However, we note that Bult et al. 2019 derived a tim-

ing solution measuring the pulse phases in each continuous good time interval (generally longer than 1 ks) and considering either a second-order polynomial or a flux-adjusted phase model in an attempt to model the timing noise, and obtained similar values of the fit 2 than that reported here. The different models used by those authors explain the slight differences between their ephemeris and the ones we obtained. In any case, we checked that our results do not change when using their ephemeris.

Since the TNG observation lasted 3.3 ks, the spacing of Fourier independent frequencies was $\delta\nu_{TNG} = 3.0 \times 10^{-4}$ Hz. This is $\sim 10^4$ times coarser than the uncertainties on the X-ray spin frequency evaluated at the epoch of the TNG observation ($\sigma_\nu(T_{TNG}) = 3.4 \times 10^{-8}$ Hz, see Table 2.1). After both the barycentric correction and the demodulation for the pulsar orbital motion had been applied, only a single trial frequency had to be searched in the TNG dataset to investigate the presence of a coherent signal at the same frequency as determined from the analysis of the X-ray data. We calculated the Fourier power density spectrum of the TNG light curve and measured a Leahy normalised [Leahy et al., 1983] power of 33.6 at a frequency of 400.97522(15) Hz. The single-trial probability associated to random white noise fluctuations is $p = 5.1 \times 10^{-8}$. We note that no significant peak at the expected pulsar spin frequency was found out neither in the power density spectrum of the light curve in which orbital demodulation was not applied nor in the reference star light curve. A precise knowledge of the spin and orbital ephemeris were thus essential for detecting the optical (and UV) coherent modulation at the spin period.

To refine the measurement of the frequency of the optical pulse, we performed an epoch folding search [Leahy, 1987] adopting 10 phase bins and a period resolution of $\delta P_{TNG,EFS} = 9.4 \times 10^{-11}$ s measuring a chi-squared value of $S_{max} = 38.6$ with a corresponding best-fitting period of $P_{TNG,EFS} = 0.00249391967(45)$ s. The 1-σ uncertainty reported in parentheses was computed [Leahy, 1987] by using the equa-

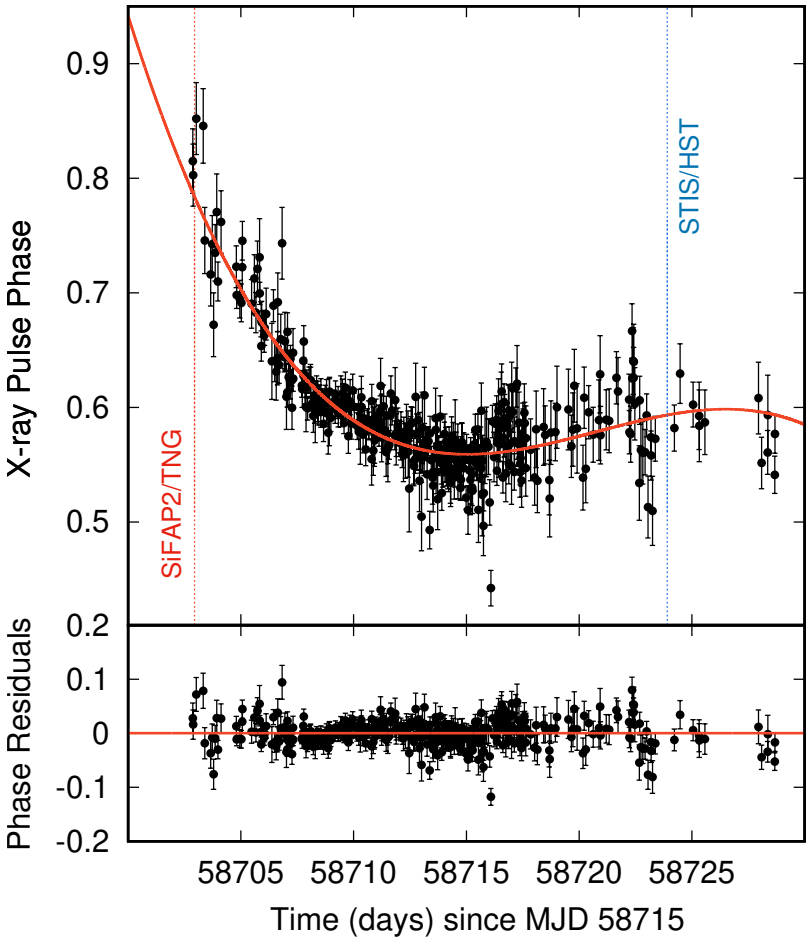

Figure 2.5: *Top*: X-ray pulse phases measured from XTI/NICER data. The red line shows the best fitting third-order polynomial function. The dashed red and blue vertical lines mark the epochs of SiFAP2/TNG and STIS/HST observations. *Bottom*: Residuals with respect to the best-fitting solution.

tion $\sigma_P = P^2/(2T_{exp})(S_{max}/(n-1)-1)^{-0.63}$, where T_{exp} is the total exposure time of the TNG optical observation. In addition, we also performed the bin-free Z_n^2 test [Buccheri et al., 1983] assuming a purely sinusoidal profile shape ($n = 1$), obtaining a value of $Z_1^2 = 34.3$ associated to a best-fitting folding period of $P_{TNG,Z_1^2} = 0.00249391976(62)$ s. This value is compatible with that estimated from the X-ray data within the uncertainties. We reported the computed chi-squared distribution with the best-fitting Gaussian model in Fig. 2.6. We then folded the TNG optical light curve using the X-ray pulse parameters, and modelled the pulse profile obtained in this way using a single sinusoidal component with a rms amplitude of $(0.0515 \pm 0.0055)\%$. Taking into account the background (see above), we then estimated the source rms amplitude as $A_{TNG}^{rms} = (0.551 \pm 0.061)\%$.

Folding at the same spin frequency the SiFAP2/TNG light curve as well as the XTI/NICER light curve extracted over the time interval between August 7 at 19:18:49 and August 8 at 00:34:55 UTC (a subset of observation ids. 2050260109 and 2050260110) highlighted a phase difference of $\Delta\phi = 0.554 \pm 0.023$, corresponding to a time lag of $\tau = 1.385 \pm 0.057$ ms (see Fig. 2.3). [Papitto et al., 2019] estimated a SiFAP2 absolute timing accuracy of $< 60\,\mu$s, whereas the corresponding NICER values is $< 0.3\,\mu$s, both much lower than the uncertainty affecting the lag measured. To estimate the effect of any residual relative timing uncertainty caused by, e.g., the uncertainty on the time dependence of the SiFAP2 clock drift, we assumed that the frequency of the optical and X-ray signals were exactly equal, and estimated the phase uncertainty driven by a frequency drift of an amount equal to the measurement error ($\sigma_\nu = 5 \times 10^{-5}$ Hz), obtaining a maximum lag of 0.4 ms. Future observations ensuring a full-orbit coverage will confirm the significance and magnitude of the pulse lag.

Hints for slight variations of the optical pulse amplitude were found, although their significance is low. The observed (i.e. not subtracted for the background) rms amplitude varied between $(0.071 \pm 0.012)\%$

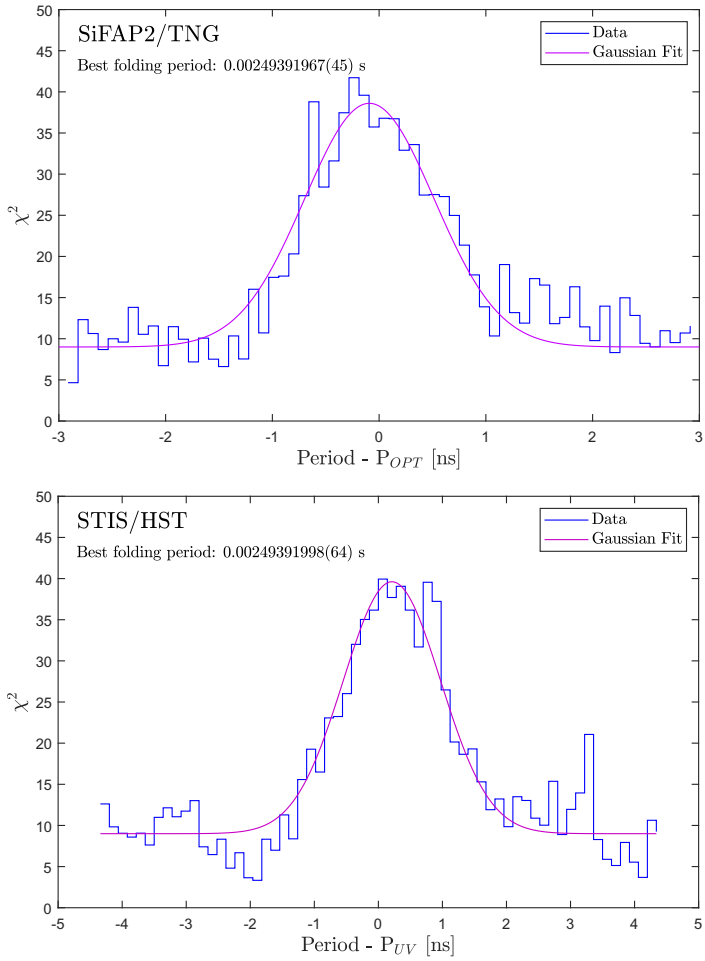

Figure 2.6: Epoch folding search curves of the optical (*top*) and ultraviolet (*bottom*) light curves of SAX J1808.4−3658. χ^2 values as a function of 63 trial periods around the NS spin period are shown in blue. The best-fitting Gaussian models are plotted in light purple. We used 10 phase bins and a period step of 9.4×10^{-11} s and 1.4×10^{-10} s for the optical and ultraviolet datasets, respectively.

and (0.037±0.013)% over 0.8 ks-long intervals. The TNG optical observation covered about one half the orbital period, from phase 0.04 to 0.49, that is, from shortly after ascending node (phase 0) to close to descending node (phase 0.5). The coherent signal was detected at all phases, although the maximum rms amplitude was detected when the pulsar was close to the ascending node. Given the intrinsic weakness of the signal, the TNG optical observation was too short to allow us to derive the orbital parameters of the optical pulse from a pulse timing analysis of that data set. To confirm the association of the optical coherent signal with the pulsar in SAX J1808, we then determined the variation of the signal strength by varying the orbital parameters adopted in the correction of the photon arrival times with respect to the values measured from the analysis of the X-ray pulsations.

We rerun the epoch folding periodicity search of the light curves by allowing the epoch of the ascending node ($T_{\rm asc}$), and the projected semi-major axis ($x = a \sin i/c$) to vary over a grid of values spaced by $\delta T_{\rm asc} = 2.5$ s and $\delta x = 1 \times 10^{-3}$ lt-s. The folding period was allowed to vary. The distributions of chi-squared values associated to the best folding period computed by varying independently $T_{\rm asc}$ and x are reported in Fig. 2.7 and in Fig. 2.8, respectively. We performed a Gaussian fitting on both the chi-squared distributions obtaining the position of the two centroids at $\Delta T_{\rm asc} = -(4.4 \pm 2.3)$ s, and $\Delta(asin(i)/c) = -(0.32 \pm 0.33)$ lt-ms. However, we caution that a coverage of an entire orbital cycle seems warranted to draw firm conclusions on the significance of a possible offset between the two pulse profiles.

We then analysed the ultraviolet events obtained from the observation performed with STIS. We corrected the position of slit channels thanks to an external custom function (`https://github.com/Alymantara/stis_photons`) and selected events (i.e. ToAs) belonging to channels of the slit within the 991−1005 (edges excluded) interval to isolate the source signal and minimise the background contribu-

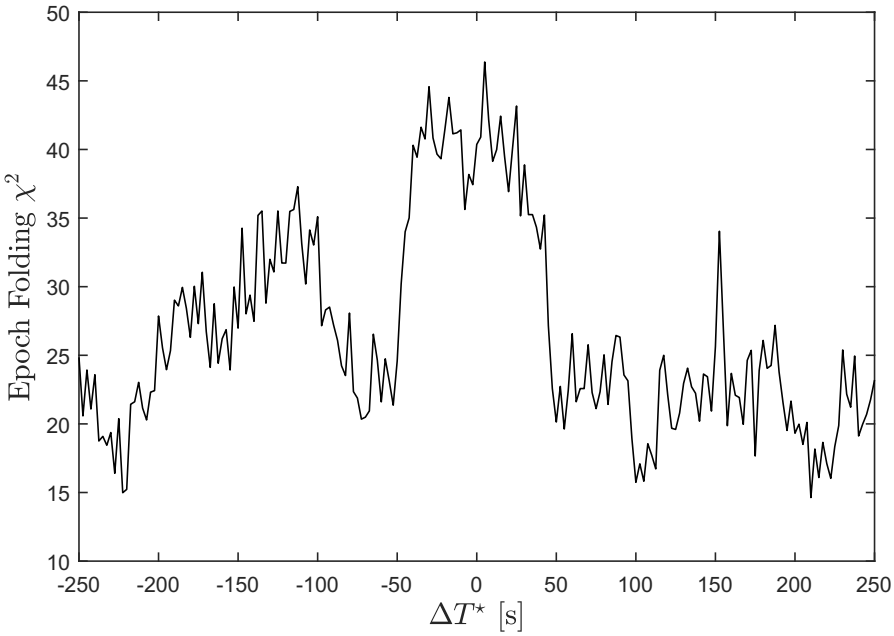

Figure 2.7: Distribution of chi-squared values obtained by varying the pulsar ascending node epoch ($T_{\rm asc}$). The distribution was obtained with an epoch folding search with $n = 8$ phase bins around the spin period expected at the epoch of the SiFAP2 observation from the X-ray analysis corrected with the value of the projection of the semi-major axis and differing by $\Delta T_{\rm asc}$ from the best fitting value. The analysis covers a shift of $\pm 250\,$s around $T_{\rm asc}$ with a time step of 2.5 s.

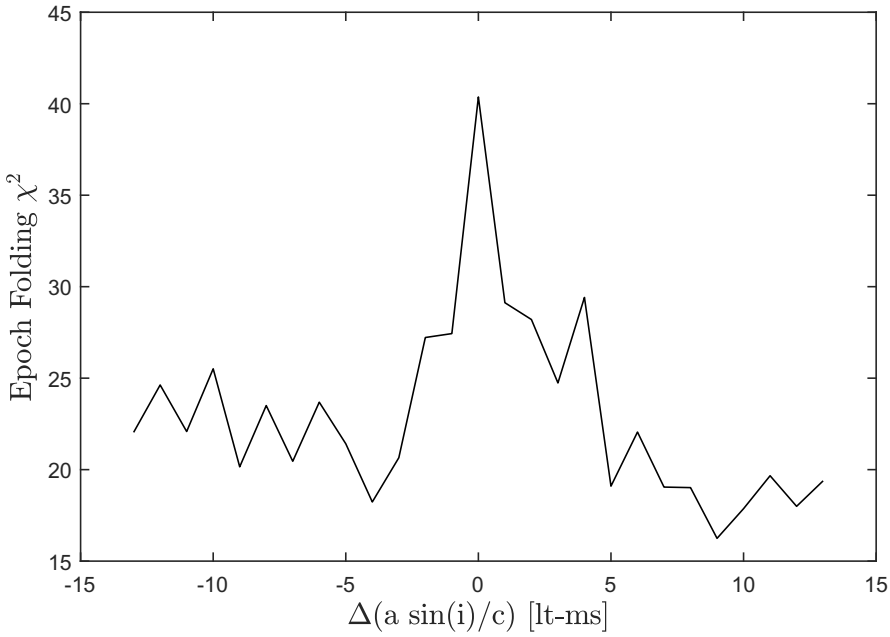

Figure 2.8: Distribution of chi-squared values obtained by varying the projection of the semi-major axis of the pulsar ($asin(i)/c$). The distribution was obtained with an epoch folding search with $n = 8$ phase bins around the spin period expected at the epoch of the SiFAP2 observation from the X-ray analysis corrected with the value of the time of ascending node and differing by $\Delta(asin(i)/c)$ from the best fitting value (see Table 2.1). The analysis covers a shift of ± 13 lt-ms around $asin(i)/c$ with a step of 1 lt-ms.

tion. We also selected the 165–310 nm wavelength interval to avoid noisy contribution due to the poor response of the G230L grating at the edge wavelengths. The list of good ToAs was corrected to the SSB by using the *ODELAYTIME* task (subroutine available in the *IRAF/STDAS* software package) and the JPL DE200 ephemeris.

We applied the same procedure as previously done for SiFAP2 data on the STIS dataset to search for the UV pulsed emission from SAX J1808. After having demodulated the UV photons ToAs by correcting them for the Rømer delays due to the orbital motion, we computed the Fourier power density spectrum. We found a Leahy normalised [Leahy et al., 1983] power of 26.1 at a frequency of 400.97518(22) Hz indicating coherent UV pulsations around the expected pulsar spin frequency with an associated single-trial probability of 2.3×10^{-6}. As in the case of the optical dataset, no significant peak at the expected pulsar spin frequency was found in the power density spectrum of the non-demodulated light curve. We then performed an epoch folding search using $n = 10$ phase bins and a period resolution of $\delta P_{HST,EFS} = 1.4 \times 10^{-10}$ s. We measured a chi-squared value of $S_{max} = 39.6$, and a best-fitting period of $P_{HST,EFS} = 0.00249391998(64)$ s, well in agreement, within the uncertainties, with the period from the X-ray data. The 1-σ uncertainty reported in parentheses was computed as in the optical dataset. We reported the computed chi-squared distribution with the best-fitting Gaussian model in Fig. 2.6. We performed the bin-free Z^2_n test with a $n = 1$ component, deriving a value of $Z^2_1 = 29.0$ associated to a best-fitting folding period of $P_{HST,Z^2_1} = 0.00249391997(98)$ s. We then folded the HST ultraviolet data at the best period obtained from the X-ray timing analysis (see Tab. 2.1), and plotted the background-subtracted pulse profile in the inset of Fig. 2.2. We described the shape of the UV modulation with a single Fourier component with rms fractional amplitude $\mathrm{A}^{rms}_{HST} = (2.65 \pm 0.67)\%$; note, however, that the rise to the peaks of the modulation was somewhat slower than the decay.

2.1.4 Spectral energy distribution

Fig. 2.9 shows the spectral energy distribution (SED) of the total and pulsed emissions in the optical, UV, and X-ray bands during the August 7, 2019 observations.

The optical and UV magnitudes were corrected for interstellar extinction using the empirical relation [Foight et al., 2016] $A_V = N_{\rm H}/(2.87 \pm 0.12) \times 10^{21}$ cm^{-2}, where $N_{\rm H} = 2.1 \times 10^{21}\,{\rm cm}^{-2}$ is the hydrogen column density along the line of sight to SAX J1808 [Di Salvo et al., 2019]. We used the extinction curves by [Fitzpatrick, 1999] to obtain the reddening A_λ in different bandpasses [Schlafly and Finkbeiner, 2011]. The optical monitoring data in B, V, R, i' bands[2] were taken with the 2-m Faulkes Telescope South (at Siding Spring, Australia) and Las Cumbres Observatory (LCO) 1-m robotic telescopes in Chile, South Africa and Australia (see [Elebert et al., 2009, Tudor et al., 2017]). The Faulkes/LCO magnitudes were calculated using the 'X-ray Binary New Early Warning System' (XB-NEWS; see [Russell et al., 2019, Pirbhoy et al., 2020] for details) data analysis pipeline. To estimate the optical flux of SAX J1808 at the epoch of our SiFAP2 observation, we interpolated the data of the LCO/Faulkes light curve.

The SAX J1808 outburst was also monitored with the Ultraviolet and Optical Telescope (UVOT [Roming et al., 2005]) on board the *Neil Gehrels Swift Observatory* [Gehrels et al., 2004] using different UV filters. The UV counterpart was detected in ten consecutive observations carried out between August 6 and September 14. The dereddened magnitude measured in the UVOT.UVM2[3] filter on August 7 (central wavelength of 224.6 nm and full-width at half-maximum of 49.8 nm) was 14.4±0.1 mag.

For the X-ray band, we extracted the background-subtracted spec-

[2] B, V, R in the Vega system and i' in the AB system.
[3] *Swift*/UVOT.UVM2 in the Vega system.

trum from the same event file used above to evaluate the phase difference between the X-ray and optical pulses, employing the *nibackgen3C50* background modelling tool available at `https://heasarc.gsfc.nasa.gov/docs/nicer/tools/nicer_bkg_est_tools.html` (total exposure time of ~ 2.7 ks). We assigned the latest versions of the NICER redistribution matrix ("nixtiref20170601v002.rmf") and ancillary response file ("nixtiaveonaxis20170601v004.arf") to the spectrum, and grouped it so as to contain at least 200 counts in each energy channel. The spectral analysis was performed with the Xspec package [Arnaud, 1996] (version 12.11.1) and was limited to the energy band between 0.5 and 5 keV, where the source was above the background.

The SED, from optical and UV wavelengths to X-rays, is well fitted by a continuum model consisting of the sum of a blackbody, modeled by *bbodyrad* in Xspec, and a Comptonisation component, modeled with *nthcomp* [Życki et al., 1999]. To account for the effects of photoelectric absorption by neutral matter in the interstellar medium, we included in the spectral fit the Tuebingen–Boulder model, adopting the photoionisation cross-sections from [Verner et al., 1996] and the chemical abundances from [Wilms et al., 2000]. The equivalent hydrogen column density was held fixed at $N_{\rm H} = 2.1 \times 10^{21}\,{\rm cm}^{-2}$ in the spectral fit [Papitto et al., 2009, Di Salvo et al., 2019]. Results are listed in Table 2.2. In this case, the best-fitting value of the blackbody temperature is $kT_{\rm BB} = 332 \pm 4\,{\rm eV}$, with an estimated radius of the (spherical) emission region of $3.58 \pm 0.08\,{\rm km}$ for a distance to the source of 3.5 kpc. For the *nthcomp* component, we fixed the electron temperature and photon index to the best-fitting values found for the broad-band X-ray spectrum ($kT_{\rm e}$ fixed at 50 keV and the photon index fixed at 1.9 [Sanna et al., 2019], corresponding to an optical depth of about 2 for the Comptonisation region). We obtained a seed-photon temperature of $kT_{\rm seed} = 1.48 \pm 0.03\,{\rm eV}$, in the hypothesis of a blackbody spectrum for the seed photons. We can therefore evaluate the radius of the emitting (spherical) region of the seed photon spectrum

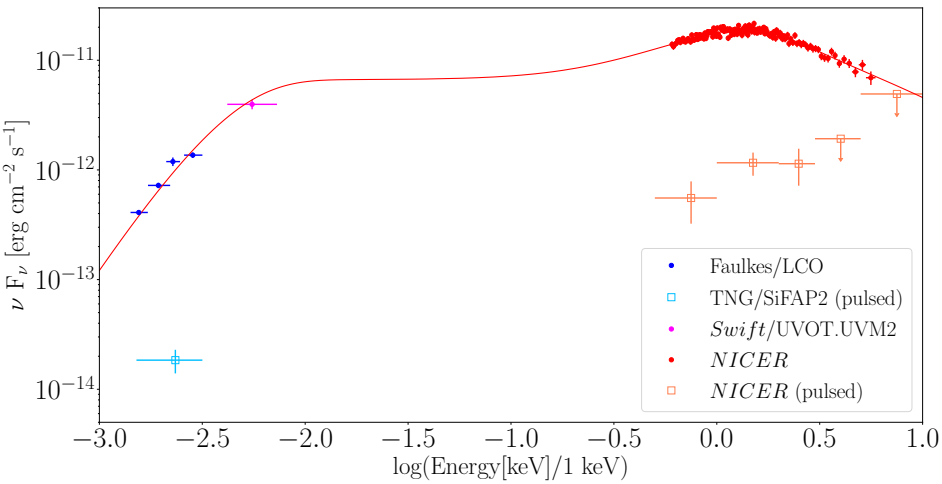

Figure 2.9: Spectral energy distributions (SEDs) for the total and pulsed emissions of SAX J1808.4−3658 on August 7, 2019 corrected for interstellar extinction. The total X-ray fluxes observed by XTI/NICER are plotted using red points. The UV/optical fluxes measured with *Swift*-UVOT.UVM2 and LCO/Faulkes are shown with magenta and blue points, respectively. For the analysis of the LCO/Faulkes data we used a new real-time data analysis pipeline, the X-ray Binary New Early Warning System [Russell et al., 2019]. The pulsed X-ray fluxes observed by XTI/NICER are computed over the 0.5–1, 1–2, 2–3, 3–5 and 5–10 keV energy bands, and are plotted using orange squares. Upper limits are marked by arrows. The average optical pulsed flux observed with SiFAP2/TNG is plotted with a light blue square. The red solid line indicates the best-fitting composite model of the SED for the total emission (*diskir* model in Xspec).

by using the relation given by [in 't Zand et al., 1998]. We find a radius $\sim 10^{10} - 10^{11}$ cm, which is compatible with the inferred size of the accretion disc in this system. This may indicate that the source of seed photons for the Comptonisation may come from the outer regions of the system, which may contribute to most of the optical/UV emission of the source. This is in agreement with the widely accepted paradigm that most of the optical/UV emission in (black hole or NS) LMXB systems is produced in the outer regions of the accretion disc as the result of X-ray reprocessing [Vrtilek et al., 1990, van Paradijs and McClintock, 1995, Russell et al., 2006].

In order to obtain a more physical interpretation of the broad-band emission of SAX J1808, we fitted the SED using a model that accounts for the emission of a truncated accretion disc irradiated by a hot Comptonising accretion flow (*diskir* [Gierliński et al., 2002] in the Xspec notation). In this model, the X-ray emission consists of thermal radiation from the disc and a hard tail produced by Comptonisation of soft seed photons in a hot plasma of energetic electrons. A fraction of this radiation is intercepted by the outer regions of the disc, reprocessed and re-emitted in the optical and UV bands.

This model often describes well the broad-band emission of bright LMXBs. The column density was again fixed to $N_{\rm H} = 2.1 \times 10^{21}\,{\rm cm}^{-2}$ in the spectral fit. We obtained a statistically acceptable description of the data, with a reduced chi-squared of $\chi^2_{\rm red} = 0.89$ for 152 degrees of freedom (d.o.f.). Results are listed in Table 2.3. According to this model, the inner disc has an intrinsic (i.e., not irradiated) temperature of ~ 200 eV and a radius of ~ 25 km (inferred from the model normalisation and assuming an inclination angle of $\sim$50°, as derived from modeling of the multi-band light curve in quiescence using a Markov chain Monte Carlo technique [Wang et al., 2013]). The inner disc provides the seed photons Comptonised by the hot electron cloud close to the NS (possibly the accretion column) producing the main Comptonisation continuum observed in the X-ray band; the electron

Table 2.2: Spectral fit parameters of SAX J1808.4−3658 from optical and UV bands to the X-ray band using the absorbed *bbodyrad* plus *nthcomp* model in Xspec.

Parameter	Value
Absorption column density ($N_{\rm H}$)	$2.1 \times 10^{21}\,{\rm cm}^{-2}$ (fixed)
Black-body temperature ($kT_{\rm BB}$)	$332 \pm 4\,{\rm eV}$
Radius of black-body emission region ($R_{\rm BB}$)$^{(a)}$	$3.58 \pm 0.08\,{\rm km}$
Electron cut-off temperature ($kT_{\rm e}$)$^{(b)}$	50 keV (fixed)
Asymptotic power-law photon index (Γ)$^{(c)}$	1.9 (fixed)
Seed-photon temperature ($kT_{\rm seed}$)	$1.48 \pm 0.03\,{\rm eV}$
Normalisation ($N_{\rm nthComp}$)	$(5.8 \pm 0.1) \times 10^{-3}$
Luminosity (L_X)$^{(d)}$	$6.22^{+0.05}_{-0.04} \times 10^{34}\,{\rm erg\,s^{-1}}$
Reduced chi-squared, $\chi^2_{\rm red}$(d.o.f.)	1.15 (152)
Null-hypothesis probability	0.097

Parameters derived from the spectral modelling of data acquired by NICER/XTI, Faulkes/LCO and *Swift*-UVOT on August 7, 2019 close to the epoch of the SiFAP2 observations. Uncertainties on each parameter are quoted at a confidence level of 1σ, whereas upper limits are reported at a confidence level of 3σ.
$^{(a)}$ The radius of the black-body emission region was evaluated assuming a source distance [Galloway and Cumming, 2006] of 3.5 kpc.
$^{(b-c)}$ The narrow energy band adopted for the spectral modelling (0.5–5 keV) does not allow tight constraints on the parameters of the Comptonised component. Therefore, in the spectral fits, the electron cut-off temperature was held fixed to $kT_{\rm e} = 50\,{\rm keV}$, a value comparable to those typically measured in the broad-band spectra of AMXPs (including SAX J1808.4−3658 [Di Salvo et al., 2019]); the asymptotic power-law photon index was fixed to $\Gamma = 1.9$, that is, the value measured using an observation with the *NuSTAR* satellite on 10–11 AugustSanna et al. [2019].
$^{(d)}$ X-ray luminosity. It was evaluated over the 0.5–10 keV range using the convolution model *cflux* in Xspec, assuming a distanceGalloway and Cumming [2006] of 3.5 kpc and isotropic emission.

Table 2.3: Spectral fit parameters of SAX J1808.4−3658 from optical and UV bands to the X-ray band using the absorbed *diskir* model in Xspec.

Parameter	Value
Absorption column density ($N_{\rm H}$)	$2.1 \times 10^{21}\,{\rm cm}^{-2}$ (fixed)
Temperature of the unilluminated inner disc ($kT_{\rm in}$)	$191^{+22}_{-21}\,{\rm eV}$
Asymptotic power-law photon index (Γ)	2.76 ± 0.06
Electron cut-off temperature ($kT_{\rm e}$)$^{(a)}$	50 keV (fixed)
Luminosity ratio ($L_{\rm Compt}/L_{\rm disc}$)$^{(b)}$	$4.2^{+2.1}_{-1.2}$
Fraction of reprocessed emission ($f_{\rm in}$)$^{(c)}$	10 % (fixed)
Fraction of reprocessed emission ($f_{\rm out}$)$^{(c)}$	$7.1^{+1.5}_{-1.2}$ %
Inner disc radius ($R_{\rm in}\sqrt{\cos i}$)$^{(d)}$	$21.9^{+2.3}_{-2.2}\,{\rm km}$
Inner radius of illuminated disc ($R_{\rm irr}$)$^{(e)}$	$1.1\,R_{\rm in}$ (fixed)
Outer disc radius (Log[$R_{\rm out}/R_{\rm in}$])$^{(f)}$	4.19 ± 0.06
Luminosity (L_X)$^{(g)}$	$5.68^{+0.05}_{-0.04} \times 10^{34}\,{\rm erg\,s^{-1}}$
Reduced chi-squared, $\chi^2_{\rm red}$(d.o.f.)	0.891 (152)
Null-hypothesis probability	0.828

$^{(a)}$ The narrow energy band adopted for the spectral modelling (0.5–5 keV) does not allow tight constraints on this parameter. Therefore, in the spectral fits, it was held fixed to $kT_{\rm e} = 50$ keV, a value comparable to those typically measured in the broad-band spectra of AMXPs.
$^{(b)}$ Ratio between the luminosity of the Comptonised component and that of the non-illuminated disc.
$^{(c)}$ Fraction of bolometric flux which is intercepted and reprocessed in the inner ($f_{\rm in}$) and outer ($f_{\rm out}$) disc. The former was fixed at 10 % in the spectral fits.
$^{(d)}$ Inner radius of the accretion disc. It was evaluated assuming a source distance [Galloway and Cumming, 2006] of 3.5 kpc and adopting a color correction factor [Kubota et al., 1998]. i is the disc inclination.
$^{(e)}$ Radius of the inner disc region that is illuminated by the corona. It was fixed at $1.1\,R_{\rm in}$ in the spectral fits.
$^{(f)}$ Ratio between the outer and the inner disc radii.
$^{(g)}$ X-ray luminosity. It was evaluated over the 0.5–10 keV range using the convolution model *cflux* in Xspec, assuming a distance [Galloway and Cumming, 2006] of 3.5 kpc and isotropic emission.

temperature of this component has been fixed to the value found from modelling of the X-ray spectrum [Di Salvo et al., 2019], while the photon index was allowed to vary (best-fitting value of $\Gamma = 2.76 \pm 0.06$). A fraction $7.1^{+1.5}_{-1.2}\%$ of this hard flux is reprocessed in the outer disc, whose radius is about 10^4 times larger than the inner disc radius, $R_{\rm out} \sim 10^{10}$ cm. This is comparable to the size of the Roche lobe of the NS and thus the size of the disc.

In order to investigate the origin of the pulsed emission in the optical/UV band, we also extracted the pulsed SED on August 7–8, 2019. For the X-ray band, we firstly evaluated the values for the background-subtracted pulse rms amplitudes over the energy ranges 0.5–1, 1–2 and 2–3 keV, as well as the 3σ upper limits over the ranges 3–5 and 5–10 keV. We calculated the de-absorbed X-ray fluxes over these same energy ranges by extrapolating the best-fitting model for the total emission (pulsed plus unpulsed), and multiplied them by the corresponding values (or upper limits) of the pulse rms amplitude to obtain integrated pulsed fluxes. We then multiplied the values so evaluated for the ratio between the mid-point energy of the interval and the width of the energy interval to derive pulsed fluxes (and upper limits) in νF_ν units. To convert the pulsed optical fluxes into νF_ν units, we multiplied dereddened fluxes by the filter full-width at half-maximum (89 nm, 84 nm, 158 nm and 154 nm for the B, V, R, and i'[4] filters, respectively). We then co-added the fluxes in the four different bands to obtain one single value for the pulsed flux covering the SiFAP2 operating band (320–900 nm) and multiplied such value by the optical pulse fractional amplitude. A total of 4 SED data points were obtained in this way (see Fig. 2.9), not enough to perform a meaningful modeling. We could test just two-parameters models on these data, such as blackbody, thermal emission from the disc, bremsstrahlung, and power-law. A power-law model fit to the SED data points for

[4]We converted the AB magnitude of filter i' in the Vega system.

the pulsed optical and X-ray emissions yields a reduced chi-squared value of $\chi^2_{\rm red} = 0.4$ for 2 d.o.f, and a functional dependence of the form $\nu\, F_\nu \propto \nu^{(0.62\pm0.04)}$.

2.1.5 Models

Here, we discuss the possible origin of optical and UV pulsations, after extracting and modelling the SED.
Thermal emission from the NS surface has already been proposed to explain the relatively bright UV emission from the binary MSP PSR J0437−4715 Kargaltsev et al. [2004]. In SAX J1808, the thermal black-body radiation should originate from warm concentric rings surrounding the polar caps. This thermal radiation would be pulsed as consequence of the lighthouse effect. However, an extremely high temperature on the NS surface would be required to generate the observed pulsed flux in the UV and optical bands. Given the strong upper bound on the area of the emitting region on the NS surface (less than $\sim 100\,{\rm km}^2$), the required temperature should be $>1\,{\rm MeV}$, which clearly rules out the hypothesis of the thermal nature for the pulsed radiation.

For the coherent signals not to be smeared out by light travel time delays, projection of their emission region along the line of sight should be smaller than $cP_{\rm spin}/2 \sim 300 - 400\,{\rm km}$, where c is the speed of light in vacuum. Another possible interpretation for the origin of the optical/UV pulsed emission is that the pulsed Comptonisation component induces a pulsed optical/UV emission from the outer disc regions at a distance of $R_{\rm out} \sim (2-3)\times 10^{10}\,{\rm cm}$ from the pulsar. The hard X-ray emission arising from the polar cap irradiates the outer disc like a lighthouse, and the high inclination angle of the system ($i \sim 50°$Wang et al. [2013]) may give rise to a geometrical modulation of this emission (see Fig. 2.10 for a schematic representation). If the UV/optical pulsations arose from optically thick

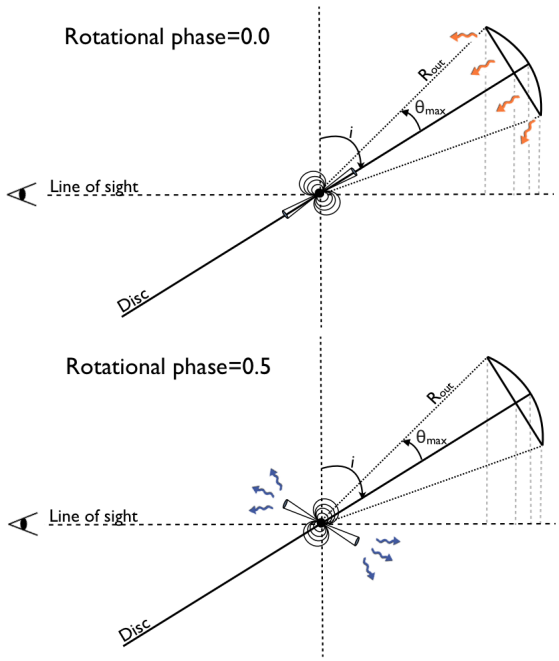

Figure 2.10: Schematic representation of the reprocessing model for the optical and ultraviolet pulsations. *Top*: For a small angle between the NS magnetic axis and the disc plane, the hard X-ray photons emitted close to the NS polar caps intercept the outer regions of the geometrically thick accretion disc (at a distance $R_{\rm out}$ from the pulsar) in the opposite direction with respect to the observer's line of sight. The X-ray photons are reprocessed and re-emitted at optical and ultraviolet energies (see orange arrows), and are partly directed along the line of sight. In this configuration, the observed pulsed emission is minimum in the X-ray band, and maximum in the optical and ultraviolet bands (this corresponds to a rotational phase of $sim0.0$ according to the convention adopted in Fig. 2.3). *Bottom*: At a separation of about half a rotational cycle (or multiples), the fraction of hard X-ray photons radiated along the observer's line of sight is maximum, and is not geometrically occulted by the disc (see blue arrows). In this configuration, the observed pulsed emission is maximum in the X-ray band, and minimum in the optical and ultraviolet bands (this corresponds to a rotational phase of $\sim$0.5 according to the convention in Fig. 2.3). In both panels, i denotes the inclination angle of the system and θ_{max} the maximum aperture angle of the cap at a distance $R_{\rm out}$ from the pulsar.

emission or reprocessing, the $\sim 2.5 \times 10^{31}\,\mathrm{erg\,s^{-1}}$ optical pulsed luminosity would imply a temperature of $\approx 2(l/300\,\mathrm{km})^{-2}\,\mathrm{keV}$, where l is the size of the emitting region and a bolometric luminosity of $\approx 10^{41}(l/300\,\mathrm{km})^{-6}\,\mathrm{erg\,s^{-1}}$, making this model untenable. Moreover, the maximum size of this region limits the amount of energy that can be re-emitted for reprocessing of X-ray pulsations in the outer region of the disc ($R_{\mathrm{out}} \sim (2-3)\times 10^{10}\,\mathrm{cm}$) to $\sim 10^{29}\,\mathrm{erg\,s^{-1}}$ in the 320−900 nm band, even in the most favorable case of an inclination of 90°. The problem with this interpretation would be exacerbated if reprocessing or energy release in optically thick matter occurred in regions of size comparable to the characteristic scales of SAX J1808, namely the NS radius ($R_{\mathrm{NS}} \sim 10\,\mathrm{km}$), the inner disc boundary close to the corotation radius ($r_c = (GM_{\mathrm{NS}}P_{\mathrm{spin}}^2/4\pi^2)^{1/3} \sim 32\,\mathrm{km}$) or the light cylinder radius ($r_{lc} = cP_{\mathrm{spin}}/2\pi \sim 120\,\mathrm{km}$); in fact all these regions are smaller than $\sim 300\,\mathrm{km}$.

Hot electrons in the post-shock region of the accretion column will emit cyclotron photons at a fundamental energy of $E_{\mathrm{cyc}} \sim 4(r/R_{\mathrm{NS}})^{-3}\,\mathrm{eV}$, for a surface magnetic field of SAX J1808 of $B \sim 3.5 \times 10^8\,\mathrm{G}$ [Burderi et al., 2006]. If the optically thick regime extended up to n-th cyclotron harmonic, a Rayleigh-Jeans spectrum would result up to the corresponding energy [Thompson and Cawthorne, 1987]. For SAX J1808 the maximum expected luminosity would be $L_{\mathrm{cyc(opt)}} \sim 10^{29}\,\mathrm{erg\,s^{-1}}$ in the 320–900 nm band, and $L_{\mathrm{cyc(UV)}} \sim 6 \times 10^{29}\,\mathrm{erg\,s^{-1}}$ in the 165–310 nm band, i.e. more than two orders of magnitude lower than the measured values. Therefore it can also be excluded that self-absorbed cyclotron emission in the accretion column is responsible for the optical/UV pulsed flux of SAX J1808, unless emission in these bands is strongly beamed, which is deemed unlikely given the high pulse duty cycle. Also, pencil beaming due to the reduction of the cyclotron opacity for photons propagating along the field lines [Basko and Sunyaev, 1975] is expected at energies much lower than E_{cyc}, i.e. below the optical band within which we observed. These limitations would

no longer hold if the optical/UV pulsed emission were produced by a coherent emission process [Melrose, 2017], whose specific intensity can vastly exceed that of thermal emission. However we note that coherent emission from rotation-powered pulsars is characterised by a steep power-law like radio spectrum and is not expected to operate at much higher frequencies.

Similar to the case of isolated rotation-powered pulsars [Pacini and Salvati, 1983], synchro-curvature radiation [Harding et al., 2018, Torres, 2018] by relativistic electrons and positrons accelerated by the rotating NS magnetosphere might give rise to the optical and UV pulsations of SAX J1808. In this interpretation, the efficiency with which SAX J1808 converts the spin-down power into pulsed UV and optical luminosity would be $\eta_{UV} \sim 1 \times 10^{-2}$ and $\eta_{opt} \sim 6 \times 10^{-4}$, respectively, the former being about 100 times larger than that of the Crab pulsar in the UV (165–310 nm) and B bands [Mignani, 2011]. Such a high efficiency is much larger than that usually observed for isolated rotation-powered pulsars, and points toward the existence of a synergistic physical process.

Models based on magneto-hydrodynamic simulations Parfrey and Tchekhovskoy [2017] predict that the NS magnetic field lines coupled to the disc within the corotation radius are rapidly twisted, pushed outwards and forced to open Parfrey et al. [2016], a phenomenon possible only in AMXPs with high magnetic diffusivity discs. In this picture the rotation-powered mechanism would not be inhibited by the presence of the accretion disc; rather its power would increase (as compared to discless pulsars) owing to the opening of additional magnetic field lines and the corresponding flux enhancement across the light cylinder surface. This leads to an increase of the spin-down torque applied to the NS and a stronger electromagnetic pulsar wind Parfrey and Tchekhovskoy [2017]. A net spin-down rate of order $\sim -1 \times 10^{-13}\,\mathrm{Hz\,s^{-1}}$ would be expected in the case of SAX J1808. We note that a comparably large spin-down torque and rate may

arise from magnetic field lines threading the disc beyond the corotation radius Kluźniak and Rappaport [2007]. If the high optical and UV pulsed luminosities of SAX J1808 result from such an enhanced rotation-powered mechanism, this must co-exist (or alternate on timescale shorter than those required to detect pulsations with current instrumentation) with the accretion-powered mechanism that produces the X-ray pulsations.

Alternatively, the power of the so-called *striped wind* [Coroniti, 1990] may also be enhanced by the same disc-magnetosphere interaction. In this model, part of the pulsar spin-down power is carried away in the form of low-frequency waves consisting of stripes of toroidal magnetic field; these structures propagate along the equatorial plane of the pulsar and are converted into a wind of relativistic magnetized plasma beyond the light cylinder radius through magnetic reconnection. In this framework, the optical and UV pulsations from SAX J1808 would arise from beamed synchrotron radiation by heated charged particles moving close to the light cylinder radius [Kirk et al., 2002]. Here, synchrotron radiation is optically thin to emission in the UV and optical bands, as synchrotron self-absorption occurs below [Rybicki and Lightman, 1979] $E_{\rm break} \sim 0.04\,{\rm eV}$. Optical/UV pulsed emission from synchrotron radiation is still expected at distances $\lesssim 600\,{\rm km}$ from the NS, considering that the synchrotron cooling timescale is shorter than $P_{\rm spin}/2$. The efficiency of this process could be enhanced at the termination shock between the pulsar wind and the accretion disc [Papitto et al., 2019, Veledina et al., 2019, Campana et al., 2019].

An intriguing feature is the half cycle shift between the optical and the X-ray pulsations from SAX J1808. It is tempting to consider the possibility that matter accretion takes place only on one pole of the NS, thus giving rise to the pulsed X-ray signal, whereas accretion is inhibited on the opposite side and a rotation-powered mechanism gives rise to the optical/UV pulsation in anti-phase. A dipole magnetic

field whose center is shifted from the center of the NS might make this possible.

2.1.6 Conclusion

In this work we analysed the XTI/NICER, SiFAP/TNG and STIS/HST data of SAX J1808 during its 2019 outburst. We first detected ever optical and UV pulses at the pulsar spin period simultaneously with X-ray pulsations in an AMXP.

Before SAX J1808, fast optical pulsations were detected only from the transitional millisecond pulsar PSR J1023+0038 [Ambrosino et al., 2017] while it was lingering in an X-ray sub-luminous disc state at an average (0.5–10 keV) X-ray luminosity of $L_X \sim 4 \times 10^{33}\,\mathrm{erg\,s^{-1}}$. The pulsed optical luminosity was high also in that case ($\approx 10^{31}\,\mathrm{erg\,s^{-1}}$), considering that the source was releasing a spin-down power of $4.3 \times 10^{34}\,\mathrm{erg\,s^{-1}}$ in the radio pulsar state. Optical and X-ray pulses were almost phase aligned and detected only during the so-called *high* X-ray luminosity mode in which the source spends $\sim 70\%$ of the time, but were seen to suddenly disappear in the lower luminosity mode, suggesting a common underlying process [Papitto et al., 2019]. Both the optical and X-ray pulsations observed from PSR J1023+0038 are thought to originate from synchrotron radiation in the intrabinary shock just beyond the light cylinder radius, where the wind of relativistic particles ejected by the pulsar meets the accretion disc [Papitto et al., 2019, Veledina et al., 2019, Campana et al., 2019]. In particular, [Papitto et al., 2019] and [Veledina et al., 2019] suggested that the multiwavelength phenomenology of PSR J1023+0038 could be due ultimately to the presence of an active rotation-powered in the system and its interaction with an accretion disc truncated just outside the light cylinder radius.

On the other hand, optical pulsations from SAX J1808 were detected in an intermediate stage of the outburst, when the X-ray lu-

minosity had not yet peaked. The corresponding X-ray luminosity exceeded that of PSR J1023+0038 by about an order of magnitude ($L_X \sim 6 \times 10^{34}\,\mathrm{erg\,s^{-1}}$). Optical pulses lagged the X-ray ones by $\sim 1.4\,\mathrm{ms}$, i.e. they were almost in anti-phase. During this outburst and the previous ones, the X-ray spectral and timing properties of SAX J1808 did not show any evidence for transitions to a non-accreting regime. These arguments suggest that its X-ray, UV and optical pulses can be hardly explained by invoking the same physical mechanism.

The widely accepted paradigm is that a pulsar could be either accretion or rotation-powered. In the accretion-powered case the intrusion of high-density accreting plasma into the magnetosphere would easily suppress the acceleration of particles in the magnetosphere and the resulting emission [Shvartsman, 1970, Lipunov, 1987]. However, the optical/UV pulsations we have detected in SAX J1808 are hardly interpreted in terms of accretion, and rather favor a magnetospheric interpretation. We conclude that for the first time we have an evidence that emission due to particle acceleration in the magnetosphere of a pulsar (and associated to a rotation-powered mechanism) can take place even when the magnetosphere is engulfed with accreting matter.

This discovery opens a novel observational window in the study of accreting NSs in low mass X-ray binaries, as the higher sensitivity afforded by optical and UV fast photometric observations may allow the discovery of coherent pulsations in sources and regimes for which X-ray pulsations have remained undetected.

3

Transitional millisecond pulsars

The work presented in this chapter is published in the following articles:

- Campana, S.; **Miraval Zanon, A.**; Coti Zelati, F.; Torres, D. F.; Baglio, M. C.; Papitto, A.; *"Probing X-ray emission in different modes of PSR J1023+0038 with a radio pulsar scenario"*, A&A Letter 2019, 629, L8, https://doi.org/10.1051/0004-6361/201936312
- **Miraval Zanon, A.**; Camapana, S.; Ridolfi A.; D'Avanzo, P.; Ambrosino, F.; *"X-ray study of high-and-low luminosity modes and peculiar low-soft-and-hard activity in the transitional pulsar XSS J12270–4859"*, A&A 2020, 635, A30, https://doi.org/10.1051/0004-6361/201936356

3.1 Probing X-ray emission in different modes of PSR J1023+0038 with a radio pulsar scenario

Transitional pulsars provide us with a unique laboratory to study the physics of accretion onto a magnetic NS. PSR J1023+0038 is the best studied of this class. We investigate the X-ray spectral properties of J1023 in the framework of a working radio pulsar during the X-ray active state. We modelled the X-ray spectra in three modes (low, high, and flare) as well as in quiescence, to constrain the emission mechanism and source parameters. The emission model, formed by an assumed pulsar emission (thermal and magnetospheric) plus a shock component, can account for the data only adding a hot dense absorber covering ∼30% of the emitting source in high mode. The covering fraction is similar in flaring mode, thus excluding total enshrouding, and decreases in the low mode despite large uncertainties. This provides support to the recently advanced idea of a mini-pulsar wind nebula (PWN), where X-ray and optical pulsations arise via synchrotron shock emission in a very close (100 km, comparable to a light cylinder), PWN-like region that is associated with this hot absorber. In low mode, this region may expand, pulsations become undetectable, and the covering fraction decreases.

Introduction

PSR J1023+0038 (hereafter J1023) was discovered as a peculiar magnetic cataclysmic variable with radio emission [Bond et al., 2002]. Subsequent observations carried out with the Green Bank Telescope showed that the source in 2007 was a radio millisecond pulsar [Archibald et al., 2009]. Between 2007 and 2013 J1023 appeared as an eclipsing

1.69-ms radio pulsar in a 4.75-h binary orbit. In June 2013 a transition took place, with the disappearance of the radio pulses and the reappearance of the accretion disc, with a strong double-peaked $H\alpha$ emission lines Halpern et al. 2013, Stappers et al. 2014. During the currently X-ray active state, a puzzling behaviour has been observed across the multi-wavelength spectrum: J1023, as well as the other transitional pulsars, alternates between a high mode, during which X-ray pulsations are detected (with a pulsed fraction of $\sim 8\%$) to a low mode, during which X-ray pulsations are not detected ($3\,\sigma$ upper limit of $< 2.7\%$) and the source is dimmer (in X-rays) by a factor of ~ 7 Archibald et al. 2009, 2010, 2015, Papitto and Torres 2015, Bogdanov et al. 2015, Campana et al. 2016.

Transitions from high to low mode occur very quickly, on a ~ 10 s timescale in X-rays [Bogdanov et al., 2015]. Similar rectangular dips occur in the optical and UV light curves Shahbaz et al. 2015, Papitto et al. 2019. A radio flare is often observed at the egress of the low mode [Bogdanov et al., 2018]. A flaring mode appears too during the X-ray active state, with bright flares occurring randomly and reaching a luminosity a factor of ~ 10 larger than in the high mode with no detectable X-ray pulsations ($< 1.5\%$, Archibald et al. [2015]).

The detection of X-ray pulsations during the active state, led several authors to speculate that these pulsations were caused by accretion of matter onto the NS surface Linares 2014, Takata et al. 2014, Archibald et al. 2015, Bogdanov et al. 2015, Papitto and Torres 2015, Campana et al. 2016, Jaodand et al. 2016b, Coti Zelati et al. 2018. Mechanisms involving the action of the NS rotating magnetosphere (i.e. propeller) were invoked to explain this astonishing behaviour and the fastness of the transition across modes Papitto et al. 2014, Linares 2014, Papitto and Torres 2015, Campana et al. 2016.

Observations with the SiFAP ultra-fast photometer recently revealed optical pulsations in J1023. Optical pulsations were detected at a low level ($\sim 1\%$ pulsed fraction) in the high mode, at a lower

amplitude in the flaring mode, but not in the low mode (Ambrosino et al. 2017, Papitto et al. 2019; see also Zampieri et al. [2019b], who used a different fast photometer, Aqueye+). The detection of optical pulsations during the high mode of J1023 at such a high flux level is left unexplained if based on accretion [Ambrosino et al., 2017]. The most promising explanation for the optical pulsations in the accretion scenario should involve cyclotron emission in the accretion column. However, this mechanism fails to account for the observed pulsed luminosity by a factor of > 40 [Papitto et al., 2019]. Pulsed emission has also been detected in the hard X-ray energy range with *NuSTAR* [Papitto et al., 2019].The spectrum of the pulsed emission can be described by a single power-law from optical to hard X-rays, with the same overall spectrum as the primary emission.

Papitto et al. [2019] suggested that optical and X-ray pulses during the high mode are produced by synchrotron emission from the intra-binary shock that forms where a striped pulsar wind meets the accretion disc, just outside the light cylinder. During the low mode, this intra-binary shock moves away from the light cylinder so that the deposited energy is not enough to generate pulsations (but see Veledina et al. [2019] for a slightly different interpretation). This new framework comprises a radio pulsar always at work during the active state, and pulsations that come not from the accretion of matter on the NS surface but that are ultimately amenable to the rotational energy losses (see also Coti Zelati et al. [2014]). Papitto et al. [2019] also suggested that the flaring mode could be ascribed to a complete enshrouding of the radio pulsar.

Here, we reconsider our accretion scenario for J1023 [Campana et al., 2016], in light of these new discoveries. Based on X-ray data collected with the *XMM-Newton* satellite, we shall here test on the possible continuous presence of an active radio pulsar. We also add flaring mode data that were previously neglected.

3.2 XMM-Newton data analysis

We take the start from the same data set presented in Campana et al. [2016]. To these spectra obtained for J1023 in low and high mode (six *XMM-Newton* observations with the pn in timing mode and the MOS in small window mode), as well as in quiescence (one *XMM-Newton* observation and one *Chandra* observation), we added the flaring mode data of the six *XMM-Newton* observations.

The low energy part of the X-ray spectrum will be of crucial importance in the spectral modelling (see below). For this reason, we consider only MOS data in the spectral fitting. Indeed, pn data in timing mode are trustable only starting from 0.6 keV, thus biasing the spectral fit toward the continuum, disadvantaging the absorption component.

In brief, data were grade-filtered using pattern 0-12 for MOS data, and FLAG==0 and #XMMEA_EM options. Proton flares were filtered out using the standard recipe. The source events were extracted using an 870-pixel circular region. Following Bogdanov et al. [2015], good time intervals were generated for the low mode for a source count rate (pn+2 MOS) in the 0.0-2.1 c s^{-1} interval, for the high mode in the 4.1-11 c s^{-1}, and for the flaring mode in $>$ 15 c s^{-1}. The respective ancillary and redistribution files were then generated for each spectrum. MOS spectra (0.3-10 keV) were rebinned to 100 counts per energy bin. MOS data comprise about 0.5 million of photons. Given the very large signal to noise of our spectra, we added a systematic error of 2% to each spectral bin.

3.3 Physical scenario

The physical scenario driven by the new optical observations involves an active pulsar during the active state, in all modes. Building the

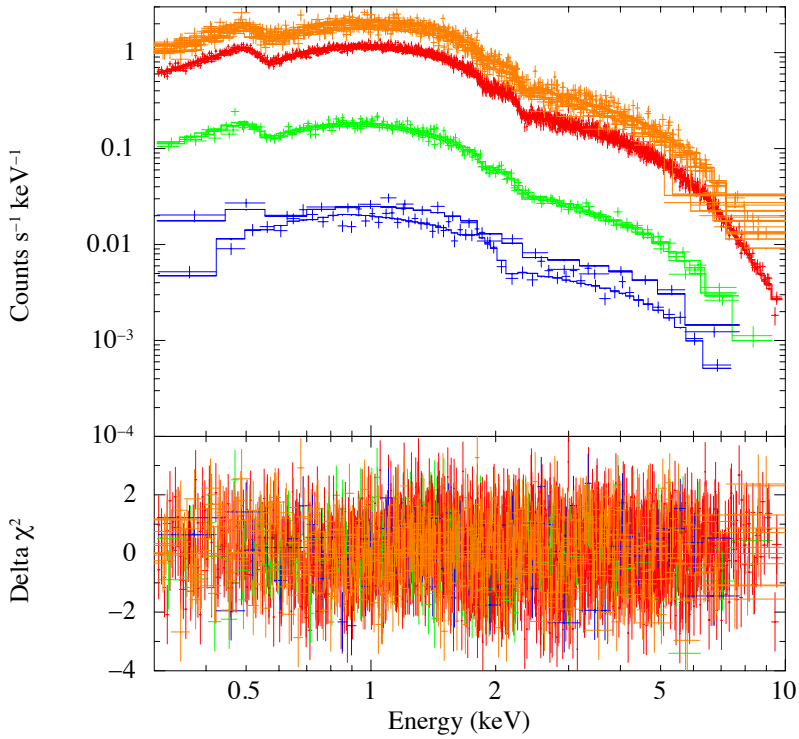

Figure 3.1: *XMM-Newton* spectra of J1023. Spectra are in the top panel. Orange refers to flare data, red to high mode data, green to low mode data, and blue (one *XMM-Newton* and one Chandra) to data in quiescence. In the lower panel residuals are shown with the same colour coding.

overall spectrum, the spectral component that we assume is present in all the spectra (quiescent, low mode, high mode, and flaring mode) will be the one associated with the pulsar. We model this as the contribution from a hot spot (a NS atmosphere model with free radius, NSATMOS, Heinke et al. [2013]) and a magnetosphere (power-law, PL1). If a pulsar is active, its relativistic particle wind will interact with the surrounding medium to produce high energy photons in a shock front (shock emission). This has been deeply investigated in the context of radio pulsars in binary systems Arons and Tavani 1993, Tavani and Arons 1997, Takata et al. 2014, 2017. This shock emission, which will be modelled with a power-law component, depends on the geometry and density of the shock front. Therefore, we need a different shock emission component for the high and low mode spectra. This component is largely dominant in the high mode spectrum, but in the low mode spectrum, both the shock and the pulsar components are comparable. The power-law is fixed in shape and normalisation for each low mode observation and for each high mode observation. Finally, to account for flare emission we added a different power-law component, with the same photon index but with different normalisation, in order to account for the different flare levels. These prescriptions set the source spectrum in all four modes: quiescent, low, high, and flare. This emission is observed to be absorbed by the interstellar medium (the absorption model `tbabs` is used to model it, equally for all the modes).

Fitting all the different mode data together with this overall model returns a very poor fit (reduced $\chi^2 = 1.18$ for 2619 degrees of freedom, corresponding to a null hypothesis probability of 10^{-10}). Wavy residuals in the spectral fit are present with a downturn at low energies. These residuals might be ascribed to the matter close to the light cylinder, which causes a distinctive absorption pattern. To account for this, we included the photo-ionised absorption model `zxipcf`. This component should be absent during quiescence and may vary among the three

modes: while the column density (i.e. the amount of matter along the line of sight) should be the same, the ionisation parameter $\xi = L/nr^2$ (where L is the ionising luminosity, n the density of the medium, and r the distance of the medium), as well as the covering factor f, could be different. We would a priori expect a larger ionisation and covering factor in the high mode with respect to the low mode values. This inference comes from Papitto et al. [2019], where they suggested that in high mode matter is close to the light cylinder, whereas during low mode episodes matter is pushed further out, preventing the pulsations to occur. Papitto et al. [2019] proposed that during the flaring mode events the source would be completely enshrouded, what has to result in a large covering factor.

3.4 Spectral fitting

We fit the MOS12 data of quiescence, low, high, and flaring modes (plus one Chandra spectrum for the quiescence of J1023) with the spectral model `tbabs × zxipcf × (nsatmos + powerlaw + powerlaw)`, as detailed in the previous section. An inter-calibration constant was also included. Results are summarized in Table 3.1.

Fig. 3.1 shows the result of our fitting procedure. The overall fit is (relatively) good with a reduced $\chi^2 = 1.07$ for 2612 degrees of freedom (corresponding to a formal 0.5% null hypothesis probability). We remark, however, that these data were collected across several years so that small changes in the spectral parameters could be envisaged, degrading the goodness of the fit. For a NS mass of $1.4\,M_\odot$ and radius 10 km, the hot emission region has a temperature of $\log(T/K) = 5.85^{+0.13}_{-0.10}$ (obtained for $\Delta\chi^2 = 2.71$) and fraction of the emitting surface of $f = 0.16^{+0.18}_{-0.07}$. The magnetospheric power-law is hard as often observed in radio pulsars with a photon index of $\Gamma_{\rm mag} = 1.06^{+0.06}_{-0.08}$. The 0.3-10 keV unabsorbed quiescent luminosity is 1.3×10^{32} erg s^{-1}

Table 3.1: Spectral fit parameters.

Parameter	Flaring mode	High mode	Low mode	Quiescence
Column density (10^{20} cm^{-2})	$5.0^{+0.3}_{-0.2}$	tied	tied	tied
Col. dens. Hot absorber (10^{22} cm^{-2})	$23.4^{+5.7}_{-1.0}$	tied	tied	0
Covering fraction ($f_{\rm cov}$)	$0.27^{+0.07}_{-0.05}$	$0.27^{+0.04}_{-0.01}$	$0.18^{+0.15}_{-0.06}$	0
Ionisation par. ($\log \xi$)	$1.4^{+0.8}_{-1.5}$	$1.9^{+0.1}_{-0.2}$	$1.9^{+0.2}_{-2.0}$	0
Shock emission photon index	$1.76^{+0.02}_{-0.02}$	$1.82^{+0.01}_{-0.01}$	$1.99^{+0.02}_{-0.03}$	–
Thermal component $\log(T/K)$	tied	tied	tied	$5.85^{+0.13}_{-0.10}$
Emitting fraction f	tied	tied	tied	$0.16^{+0.18}_{-0.07}$
Magnetospheric emission ($\Gamma_{\rm mag}$)	tied	tied	tied	$1.06^{+0.06}_{-0.08}$
Absorbed flux (10^{-12} erg cm^{-2} s^{-1}) 0.3-10 keV	50.2	13.6	1.99	0.54
Unabsorbed flux (10^{-12} erg cm^{-2} s^{-1}) 0.3-10 keV	69.2	18.6	2.54	0.56
Luminosity (10^{32} erg s^{-1}) 0.3-10 keV	156	42.2	5.76	1.27

Errors are calculated with $\Delta\chi^2 = 2.70$. The fit provided a $\chi^2_{\rm red} = 1.07$ for 2612 degrees of freedom.
Fluxes for the flaring mode refer to a mean of the 5 spectra (with a very small standard deviation of 4%).
Luminosity has been calculated adopting a distance of 1.37 kpc [Deller et al., 2012].

(adopting a distance of 1.37 kpc, Deller et al. 2012), with the non-thermal component making 92% of the total (see Table 3.1).

The high mode has, in addition, a power-law component with photon index $\Gamma_{\rm high} = 1.82 \pm 0.01$. The 0.3-10 keV high mode luminosity is 4.2×10^{33} erg s^{-1} with the power-law making 97% of the total. In the low mode, the power-law component flattens to $\Gamma_{\rm low} = 1.99^{+0.02}_{-0.03}$. The 0.3-10 keV low mode luminosity is 5.8×10^{32} erg s^{-1} with the power-law making 22% of the total. The flaring mode reaches a higher (mean) luminosity 1.6×10^{34} erg s^{-1}, with the power-law component with $\Gamma_{\rm flare} = 1.76^{+0.02}_{-0.02}$ making the entire flux (Table 3.2).

Interesting results are obtained for the absorption components. The interstellar absorption is $5.0^{+0.3}_{-0.2} \times 10^{20}$ cm^{-2}, consistent with tabulated values [Willingale et al., 2013]. The intra-binary absorption component is set to zero for quiescence (and if left free to vary is < 0.5, 90% confidence level). When J1023 is active, the hot absorber has a large column density of $2.34^{+0.59}_{-0.09} \times 10^{23}$ cm^{-2}. This is tied to all the modes. In the low mode the ionisation parameter is $\log \xi = 1.9^{+0.2}_{-2.0}$ with a large error. The covering factor of this hot absorber is $0.18^{+0.15}_{-0.06}$. In contrast in high mode, the ionisation parameter is comparable $1.9^{+0.1}_{-0.2}$ (even if with a much smaller error) but the covering factor is larger $f_{\rm cov} = 0.27^{+0.04}_{-0.01}$. This should testify for an absorber closer to the source in high mode and further away in low mode. Interestingly, during the flaring mode, the ionisation parameter drops somewhat $1.4^{+0.8}_{-1.5}$ (still within the errors), and the covering factor remains consistent with the high mode value, $0.27^{+0.07}_{-0.05}$. This indicates that during the flaring mode the source is not fully enshrouded by this hot medium. Instead, flares may be due to disc or companion star activity, possibly related to magnetic reconnection.

Table 3.2: Percentage of the contribution of spectral components to the overall unabsorbed 0.3-10 keV luminosity.

State	NSA	Magn. Em.	PL
Flaring mode (1.6×10^{34})	0%	0%	100%
High mode (4.2×10^{33})	0%	3%	97%
Low mode (5.8×10^{32})	6%	72%	22%
Quiescence (1.3×10^{32})	8%	92%	–

3.5 Conclusions – Part I

In this work we have analysed the *XMM-Newton* and *Chandra* X-ray spectra of the transitional pulsar J1023. These spectra encompass all the states showed by J1023: the quiescent and active, conjugated in three flavours, low, high, and flaring mode. The rationale guiding our fit was the recently discovered optical pulsations Ambrosino et al. 2017, Papitto et al. 2019. These pulsations are present during the high mode only, and do not have a neat explanation in terms of accretion of matter onto the NS. Accretion models fail by at least an order of magnitude to account for the observed pulsed luminosity [Ambrosino et al., 2017]. A model in which X-ray pulsations occur during the high mode (only) has been put forward by Papitto et al. [2019]. This model involves a pulsar being always at work during the active state of J1023, and ultimately relates the pulsation to the rotational power.

Our X-ray spectral analysis tries to account for the observed spectra in the radio pulsar scenario. It is by no means unique (e.g. see Campana et al. [2016] for a different working spectral model), but it aims at testing whether a pulsar can be at work at all times. We find that the spectra can be modelled with a typical pulsar spectrum (thermal component plus a magnetospheric component), needed to account for the quiescent and low mode spectra, plus a power-law

component, which dominates the high and flaring mode spectra but it is also needed for modelling the low mode spectra.

This power-law component can be interpreted in terms of shock emission between the relativistic pulsar wind and the incoming material in the high and low mode. As expected it is flatter ($\Gamma \sim 2$) at lower luminosity (low mode) and steeper at higher luminosity ($\Gamma \sim 1.8$), as observed in pulsars interacting with massive companions, as PSR B1259+63 [Tavani and Arons, 1997]. The shock front in the low mode lies at larger distances from the light cylinder region, the geometry for generating pulsations is not favourable and a classical shock is expected. In the high mode, instead, the front gets close to the light cylinder, and pulsations may be generated according to the mechanism proposed by Papitto et al. [2019] and the shock emission gets harder. The fact that the shock component is by far the dominant one in the high mode supports this 'mini'- pulsar wind nebula (PWN) interpretation advanced by Papitto et al. [2019].

In this scenario, the pulsations are not magnetospheric, but are still related to the rotation power. Pulses arise via synchrotron emission in a very close, 'mini' PWN-like region of the dimension of the light cylinder ($\sim$ 100 km). Optical pulsations come from this mechanism too, thus alleviating the problem of high conversion efficiency into the optical band. As J1023 changes to the low mode, the PWN expands and pulsations vanish. Our picture is in contrast with Veledina et al. [2019], who suggested that the low mode might be associated with propeller. As shown by simulations [Parfrey et al., 2017], in the propeller state the covering angle of the surrounding medium should increase, at variance with our modelling.

In the optical, there is evidence for the presence of an accretion disc at large distances from the NS. This disc will be truncated and evaporated by the pulsar pressure just outside the light cylinder in the high mode (solution for this kind of disc geometry exist, Eksİ and Alpar [2005]. In the low mode, the disc is pushed further out to recol-

lapse again at transition. In agreement with this, the covering factor of this hot ambient medium related to the accretion disc intercepts a larger fraction of the emitting region in the high mode (being closer) than in the low mode (being more distant).

There have been suggestions that the flaring mode might correspond to a complete enshrouding of the pulsar. However, even if the power-law index is flatter in the flaring mode, the covering fraction of the hot surrounding medium remains at a level comparable to the one of the high mode. We suggest instead magnetic reconnection in the disc or even in the disc/star as a possible cause of flaring activity. Indeed, pulsations were not detected in X-ray during the flaring mode, but they were in the optical. The pulsed fraction is lower than in the high mode by a factor of ~ 5, but similar in shape, whereas the X-ray flux increases by a factor of ~ 4, suggesting that dilution might be an explanation. In Sect. 3.6 we investigate the flaring mode of another transitional pulsar XSS J12270–4859 in more detail, which occurs with a soft and hard spectrum de Martino et al. 2015, Miraval Zanon et al. 2020.

The most intriguing characteristic of the proposed spectral model is the presence of a hot medium. Indirect evidence for the presence of this medium comes from the detection of narrow emission and absorption lines in the RGS spectra of J1023. These lines were described in Coti Zelati et al. [2018], even if it was not possible to search for differences among low and high mode, due to limited statistics. The N VI triplet allowed to set a lower limit on the particle density of $n > 10^{11}$ cm^{-3}, suggesting a dense medium. Clearly, our identification of a unique medium with a single density (and ionisation parameter) is an oversimplification of a medium that could be more complex, stratified in latitude and turbulent. Despite these caveats, our spectral fitting provides a supportive indication to the proposed pulsar/mini-PWN scenario.

3.6 X-ray study of high/low luminosity modes and peculiar low-soft/hard activity in the transitional pulsar XSS J12270−4859

XSS J12270−4859 (henceforth J12270) is the first low-mass X-ray binary to exhibit a transition, taking place at the end of 2012, from an X-ray active state to a radio pulsar state. The X-ray emission based on archival *XMM-Newton* observations is highly variable, showing rapid variations ($\sim$ 10 s) from a high X-ray luminosity mode to a low mode and back. A flaring mode has also been observed. X-ray pulsations have been detected during the high mode only. In this work we present two possible interpretations for the rapid swings between the high and low modes. In the first scenario, this phenomenon can be explained by a rapid oscillation between a propeller state and a radio-ejection pulsar state, during which the pulsar wind prevents matter from falling onto the NS surface. In the second scenario, a radio pulsar is always active, the intra-binary shock is located just outside the light cylinder in the high mode, while it expands during the low mode. At variance with other transitional pulsars, J12270 shows two instances of the low mode: a low-soft and low-hard mode. Performing an X-ray spectral analysis, we show that the harder component, present in the low-hard spectra, is probably related to the tail of the flare emission. This supports the understanding that the flare mechanism is independent of the high-to-low mode transitions.

Introduction

J12270 was discovered as a hard X-ray source during the *Rossi X-ray Timing Explorer* (RXTE) survey [Sazonov and Revnivtsev, 2004a] but its nature was unclear for a few years. Initially, the source was

thought to be a cataclysmic variable (CV), similarly to J1023 [Masetti et al., 2006, Butters et al., 2008], owing to the presence of double-horned emission lines, typical of an accretion disc. Further observations showed a peculiar X-ray variability with an unusual dipping and flaring behaviour (Saitou et al. 2009; de Martino et al. 2010). Therefore, several authors suggested that J12270 was instead a NS in a LMXB (Pretorius 2009; Saitou et al. 2009; de Martino et al. 2010; Hill et al. 2011). The detection of J12270 by *Fermi*-LAT [de Martino et al., 2010] further garbled the identification of J12270 within the Galactic zoo.

J12270 had a stable emission at all wavelengths from discovery until the end of 2012, when a decrease in its X-ray flux occurred (Bassa et al. 2014; Bogdanov et al. 2014). A radio pulsar, PSR J1227−4853, was discovered in 2014 with the Giant Metrewave Radio Telescope (GMRT) at 607 MHz, and associated with J12270 [Roy et al., 2014], proving the transitional pulsar nature of J12270. Roy et al. [2015] found that PSR J1227−4853 is spinning at 1.69 ms and has a relatively low magnetic field of 1.4×10^8 G. γ-ray pulsations, after the transition, were detected using $\sim$1 year *Fermi*-LAT data (Johnson et al. 2015).

The pulsar signal is eclipsed for a large fraction of the orbit ($\sim$ 40%) at 607 MHz, probably due to free-free absorption by the intra-binary plasma emanated from the companion star. During the radio pulsar state the X-ray emission is strongly modulated at the $\sim$ 6.9 hr orbital period [de Martino et al., 2015]. The companion mass is in the range 0.17-0.46 $M_\odot$ and the distance, estimated from the dispersion measure, is $\sim$ 1.4 kpc. An optical polarimetric analysis was performed using the ESO New Technology Telescope (NTT) at La Silla (Chile) during the radio pulsar state. Baglio et al. [2016] did not detect any significant polarisation from the system, with 3-σ upper limit of 1.4% (in R-band), as expected being the source in its millisecond radio pulsar state. J12270 is the first binary for which it has been possible to observe the transition from an X-ray active state to a radio pulsar

state.

After the detection of a MSP, (back) searches for pulsations at other wavelengths led to the detection of significant X-ray pulsations in the *XMM-Newton* data (Papitto and Torres 2015). During the X-ray active state, J12270, like J1023, shows strong X-ray variability, swinging between three different modes: a high luminosity mode in which X-ray pulsations are detected at an rms of $(7.7 \pm 0.5)\%$; a low luminosity mode, during which no pulsations are detected (with an upper limit on rms amplitude of 5.9%); and a flaring mode with no pulsations too [Papitto and Torres, 2015]. Transitions between high and low modes are rapid, with a timescale of ~ 10 s [de Martino et al., 2013]. At variance with any other tMSP, J12270 shows two different low modes: low-soft and low-hard. As presented in de Martino et al. [2010, 2013] soft- and hard-low modes stand apart in the intensity-hardness ratio diagram. In this work, two possible physical scenario are presented to interpret the puzzling behaviour exhibited during the X-ray active state: one involving a transition between a propeller and a radio pulsar (Campana et al. 2016; Linares 2014) and the other one considering an active radio pulsar all the time (Coti Zelati et al. 2014; Takata et al. 2014; Papitto et al. 2019; Campana et al. 2019). Using *XMM-Newton* observations carried out during both the X-ray active state and radio pulsar state, and selecting low, high (and flare) X-ray emission modes, we test these scenarios on J12270. In Sect. 3.7 we describe the two physical scenarios and their relative spectral models. In addition, we investigate the behaviour between low-soft and low-hard modes through spectral analysis, looking if the low-hard mode spectra can be accounted for by the addition of a further spectral component. In Sects. 3.8–3.10 we describe our data set and the related spectral analysis. In Sect. 3.11, we discuss the results and we present future perspectives.

3.7 Two possible physical scenarios

In this section, we present two possible physical scenarios that could explain the rapid variability between high and low luminosity modes.

3.7.1 Pulsations due to accretion onto the NS surface in a propeller-ejection scenario

In this scenario the X-ray active state is characterised by two different accretion modes: propeller and radio-ejection. This scenario has been developed for J1023 and has been shown to properly account for its properties (Campana et al. 2016). In the propeller, the inflowing disc matter is halted at the magnetospheric boundary, acting as a centrifugal barrier. Converting the high mode observed luminosity to a mass accretion rate with a typical efficiency of 20%, we would obtain a magnetospheric radius of $r_{\rm m} \sim 105$ km (using a factor ξ=0.5 for the conversion from spherical to disc accretion Campana and Di Salvo 2018; see Table 3.3). This is larger than the light cylinder radius ($r_{\rm lc} = cP/2\pi$= 80 km, where P is the NS rotational period), indicating that matter should not even reach the magnetosphere and it should instead be expelled from the system. To force the magnetosphere toward the NS, we must suppose the presence of an advection-dominated flow, in which the dissipated energy is stored rather than being irradiated [Narayan and Yi, 1994, Narayan, 1996]. This results in a larger disc pressure, allowing matter to reach the magnetospheric boundary. A small fraction of this material might then leak through the centrifugal barrier, reach the NS surface and generate the X-ray pulsations. In this picture, this corresponds to the high mode (Campana et al. 2016).

If the accretion rate decreases, the disc pressure decreases and the magnetospheric radius expands. When this radius becomes comparable to the light cylinder radius, the radio-ejection mode sets in and

Table 3.3: Estimate of mass loss rate from X-ray luminosity and characteristic radii of J12270. We assume B $\sim 1.36 \times 10^8$ G [Roy et al., 2015].

Parameter	High mode	Low mode	Quiescence
$L_{X(0.3-10\ \mathrm{keV})}$ (erg s^{-1})	4.2×10^{33}	6.2×10^{32}	1.1×10^{32}
$\dot{M}$ (g s^{-1})	2.3×10^{13}	3.3×10^{12}	-$^{(*)}$
$r_{\mathrm{m}}^{(\dagger)}$ (km)	105	181	-$^{(*)}$
$r_{\mathrm{c}}^{(**)}$ (km)	24	24	24
r_{lc} (km)	80	80	80
State (propeller/ejection model)	propeller	radio-ejection	radio pulsar

$^{(\dagger)}$ derived as $L_X R/GM$, where M and R are the NS mass and radius, G is the gravitational constant; $^{(*)}$ we do not compute $\dot{M}$ and r_{m} for the quiescent state because the X-ray luminosity is not related to mass accretion; $^{(**)}$ r_{c} is the corotation radius

matter is expelled (e.g. Campana et al. 1998; Burderi et al. 2001). This corresponds in our picture to the low mode. The timescale for this high-low transition (and vice versa) is the free-fall timescale close to the light cylinder, which nicely fit the observed timescale (Coti Zelati et al. 2018; Veledina et al. 2019). A radio pulsar, even if reactivated, will be hardly observable due to the large amount of ionised material present in the system.

Finally, the radio pulsar quiescent state is attained when the mass accretion rate further decreases, the pulsar is able to eject all the incoming matter and the system emits in the X-ray band with a flux one order of magnitude lower (see Table 3.3). We note that this scenario can account for the high and low luminosity modes only. Flares might originate from a mechanism unrelated to the magnetospheric boundary transitions, such as magnetic reconnection in the disc or in the companion (e.g. Campana et al. 2004; Zurita et al. 2003).

This physical scenario (which is not a detailed model, nor it is

unique) can be translated into a spectral model to be tested by fitting X-ray data [Campana et al., 2016]. The high luminosity mode is characterised by:
a) a power law non-thermal component (accounting for the propeller shock);
b) a multi-temperature accretion disc, characterised by a free temperature and an inner radius (`diskbb` model). The disc temperature $T(r)$ is proportional to r^{-p} (where r is the disc radius and p is a free parameter) and we fixed $p = 0.5$ to approximate an advection-dominated flow [Narayan and Yi, 1994];
c) a heated polar cap with free radius and temperature (`nsatmos` model), to account for matter accreting onto the NS[1].

In the low(-soft) luminosity mode the radio pulsar emission and the disc component co-exist, so the model is more complex and is characterised by:
a) a power law due to a non-thermal emission (Γ), as in the high mode but with a different spectral index. This component might arise from the shock interaction between the incoming matter from the accretion disc and the pulsar wind;
b) a disc component, with the same $T(r) \propto r^{-0.5}$ curve, where the inner radius of the disc have to result larger than $r_{\rm lc}$;
c) a heated polar cap with the polar cap radius of the same size as in the high mode and allowing for the possibility of cooling;
d) a secondary power (Γ_P) law accounting for the non-thermal magnetospheric pulsar emission.

The low-soft mode is considered here, because it occurs more frequently than the low-hard, and because it is more similar to the low mode of J1023.

Finally, the quiescent state is determined only by the pulsar emis-

[1]Technically, `nsatmos` model is for a cooling NS atmosphere, but is has been shown to describe fairly well also low-level accretion.

sion (both thermal and non-thermal). All the parameters in the quiescent state (power law and polar cap radius including their normalisation) are then fixed to those of the pulsar in the low-soft mode. All spectra have been corrected for interstellar absorption using the same hydrogen column density (N_H).

3.7.2 Pulsations from an intra-binary shock in a shock emission scenario

The need for an alternative scenario comes from the discovery of optical pulsations in J1023 [Ambrosino et al., 2017]. Actually, there is no known mechanisms able to account for the large pulsed optical luminosity in J1023, involving the accretion of matter onto the NS surface (the best model, based on cyclotron emission falls by a factor $\gtrsim 35$ Ambrosino et al. 2017). Papitto et al. [2019] proposed that optical and X-ray pulsations are produced in intra-binary shocks when the relativistic wind of the pulsar interacts with the in-flowing matter close to the light cylinder. In the new physical picture (presented for J1023 in Sect. 3.3 Campana et al. 2019) the radio pulsar is always active, even during the X-ray active state, and the source of power for the pulsations is its rotational energy. The relativistic pulsar wind, interacting with the surrounding medium, produces high energy photons. Optical and X-ray pulsations are produced by synchrotron emission in the intra-binary shock, just beyond the light cylinder, at a distance $k\, r_{\rm lc}$, with k =1-2 [Papitto et al., 2019]. Veledina et al. [2019] also suggested that during the high luminosity mode the disc is truncated outside the light cylinder radius and the wind-disc interaction generates synchrotron radiation. The position of the termination shock can change. In particular, we expect that in the low luminosity mode the shock's radius expands, causing the disappearance of X-ray and optical pulsations. This hypothesis in J1023 is supported by the presence

of radio flares in correspondence with the X-ray low luminosity modes [Bogdanov et al., 2018]. Radio flares are interpreted as rapid ejections of plasma by the active radio pulsar. Papitto et al. [2019] suggested instead that during the low mode, matter is accreted onto the NS and that flares might come from a complete enshrouding of the pulsar. At variance with the previous scenario, it seems natural here to include flare mode data into the spectral fits, to investigate this possibility.

The spectral model for this scenario could be parametrised by the following composite spectral model. The pulsar is always active, also during the X-ray active state. For this reason all modes (flare, high, and low) and the quiescence are characterised by the NS thermal and non-thermal emission. The NS magnetospheric non-thermal emission is modelled by a power law with spectral index $\Gamma_{\rm mag}$. The NS thermal emission, produced by polar caps with free radius and temperature, is parametrised by the `nsatmos` model. All free parameters (spectral index $\Gamma_{\rm mag}$, NS temperature and radius) are equal for all modes and the quiescence. In addition flare, high, and low modes are modelled by a second power law due to a further non-thermal emission, probably coming from the shock. The associated spectral index $\Gamma_{\rm shock}$ should be different in all modes because it depends on the geometry and density of the shock, hence it is a free parameter. A model with only these components is not able to reproduce the X-ray spectral data of J1023 (see Campana et al. 2019). One possibility is to include a partially ionised material enshrouding the pulsar modelled by the XSPEC model `zxipcf`. This should account for the presence of matter close to the pulsar. This spectral component depends on the amount of matter along the line of sight (equal for all three modes), the ionisation parameter $\xi = L/nr^2$ (where L is the source luminosity, n the density of the medium and r the distance of the medium), and the covering fraction f. Both ξ and f should be different for all three modes, varying luminosity, and distance of the shock, at least. The overall model is then composed as follows:

a) a power law non-thermal component accounting for the shock emission, different for the three modes (flare, high, and low modes);
b) a heated polar cap with free radius and temperature (`nsatmos` model) common to all modes and including the quiescent state, accounting for the pulsar polar cap thermal emission;
c) a power law non-thermal component common to all modes and including the quiescent state, accounting for the pulsar magnetospheric emission;
d) a partially ionised absorption component, different for the three modes, accounting for the inner edge disc absorption.

3.7.3 Low-soft and low-hard modes

J12270, besides showing the distinctive behaviour between low and high modes characteristic of transitional pulsars, has also presented an unusual activity in the low mode, showing a soft and hard instance [de Martino et al., 2010, 2013]. Concerning the spectral analysis of the low-hard and low-soft modes, given the much lower statistics, we were forced to considered simpler spectral models. Given that the low-hard mode is definitely brighter than the low-soft mode, we explored the possibility that the low-hard mode can be described as the superposition of an additional spectral component on top of the stable low-soft one. We tested three different composite models. In all of these models we expect a common emission, described by a power law, and an additional component for the low-hard spectra only, that causes the variation in spectral shape.

We consider three different additive models to single power law describing the low-soft spectra. We add either a bremsstrahlung component (`bremss` or `mekal`, as for the tail of a magnetic flare), a blackbody thermal emission (as footprints of hotter regions in the disc), or another power law (underlining our ignorance in the process).

3.8 Observations

J12270 was observed four times by *XMM-Newton* between 2009 and 2014. In our analysis, we considered only the first three observations (see Table 3.4) performed with the EPIC cameras (MOS and pn). We excluded the last observation (Obs. ID. 0729560801) since the source had a flux 1.6 times higher than the previous observation during quiescence [de Martino et al., 2015]. A variation in the quiescent flux of a MSP is not expected, nor observed in other MSPs and J1023. Given the construction of our models, we can only attain one single quiescent value. Fitting a variable quiescent flux would require the addition of another spectral component, which is not allowed by the quality of the data. We decided to show the results concerning the lowest quiescent flux. We repeated the same fitting procedure considering the brighter quiescent observation, finding that spectral parameters change by less than 10%. A follow-up discussion is presented in Section 3.11. In the first and third observation (Obs. ID. 0551430401 and 0727961401) both the EPIC-pn and the EPIC-MOS cameras operated in imaging full window mode using thin filters. The observation performed on 2011 Jan. 01 (Obs. ID. 0656780901) was made in fast timing mode with the EPIC-pn camera only. The first two sets are widely discussed in de Martino et al. [2010] and in de Martino et al. [2013]. The last observation (2012 December 29) is described in Bogdanov et al. [2014], de Martino et al. [2015], and Papitto and Torres [2015].

3.9 Data reduction

The data were processed with the *XMM-Newton* Science Analysis Software (SAS) version xmmsas_20170719_1539-16.1.0 and the latest calibration files. EPIC data were processed with `emproc` and `epproc` tasks. The data were filtered selecting pattern 0-12 (0-4) for MOS

Table 3.4: Summary of *XMM-Newton* observations used in this analysis. MOS counts are the sum of MOS1 and MOS2 counts.

Obs. ID.	Obs. start	Instr.	Duration (ks)$^{(*)}$	Flare mode dur.-ks (cts)	High mode dur.-ks (cts)	Low-soft mode dur.-ks (cts)	Low-hard mode dur.-ks (cts)
0551430401	2009-01-05	pn	24.9	0.8 (6019)	16.7 (29662)	2.7 (792)	1.1 (694)
		MOS	30.4	0.9 (3408)	18.6 (19155)	3.0 (461)	1.2 (455)
0656780901	2011-01-01	pn	29.2	1.1 (10778)	19.1 (71128)	4.2 (3032)	0.9 (1381)
		MOS	30.6	1.1 (3486)	18.9 (20733)	4.1 (664)	0.8 (426)
0727961401	2013-12-29	pn	27.9	Quiescence (1544)			
		MOS	34.4	Quiescence (1382)			
0729560801	2014-06-27	MOS	40.8	Quiescence (2448)			

$^{(*)}$ The sum of exposures in different modes is lower than the total exposure time, since we selected pure modes, excluding the transition intervals.

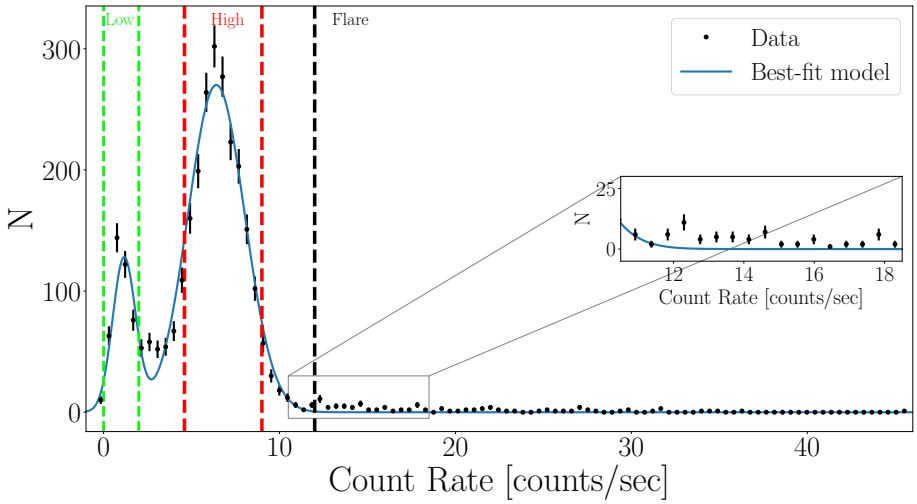

Figure 3.2: Distribution of the background-subtracted J12270 count rate obtained from 20-s binned lightcurves from the 2009 January and 2011 January *XMM-Newton* EPIC data. We define the region between 0 cts s^{-1} and 2 cts s^{-1} as the low-soft mode, while the region between 4.6 cts s^{-1} and 9 cts s^{-1} is the high mode. Higher than 12 count s^{-1} we define flare mode. In the zoomed plot we can see that the double Gaussian fit does not interpolate data during the flares.

(pn) and FLAG == 0. We filtered the last observation (Obs. ID. 0727961401) that is affected by proton flares by excluding time intervals during which the overall count rate was greater than 10 cts s^{-1} for the EPIC-MOS data, and greater than 50 cts s^{-1} for the EPIC-pn data. We used a region centred on the source with radius of 570, 676, and 312 pixel to extract EPIC-MOS (respectively for Obs. ID. 0551430401, 0656780901 and 0727961401) light curves and spectra. Background events were extracted from a similar region located on the same CCD with no sources. In the first two observations, the source was too bright and EPIC-MOS data were affected by pile-up. To reduce this effect, we excised the innermost region of the source with a radius of 150 and 140 pixel (respectively for Obs. ID. 0551430401 and 0656780901). The EPIC-pn events in fast timing mode were extracted from RAWX=29-50 px (Obs. ID. 0656780901) while events in imaging full window mode were extracted from 570 and 263 pixel region (Obs. ID. 0551430401 and 0727961401). No pile-up is present in the EPIC-pn data.

For each observation we extracted source and background light curves of the three CCD cameras and we binned all of them with the same time resolution of 20 s. We combined background-subtracted and exposure-corrected EPIC 0.3-10 keV light curves by using the `epiclccorr` tool. The final light curves (see de Martino et al. 2010, de Martino et al. 2013 and also Fig. 3.3) are characterised by the three source modes described above. Fig. 3.2 shows the distribution of count rates of the 2009 January and 2011 January observations. We defined the interval 0.0-2.0 cts s^{-1} (selected in the time intervals 54836.70128259-54837.01239370 MJD for Obs. ID. 0551430401 and 55562.29653722-55562.61031037 MJD for Obs. ID. 0656780901) as the low-soft mode (see Fig. 3.3), while the interval 4.6-9.0 cts s^{-1} the high mode range. We found a bimodal distribution of the count rates (as presented in Bogdanov et al. 2015 for J1023), with the low-soft and high mode seen as peaks at $\approx$ 1 cts s^{-1} and $\approx$ 7 cts s^{-1},

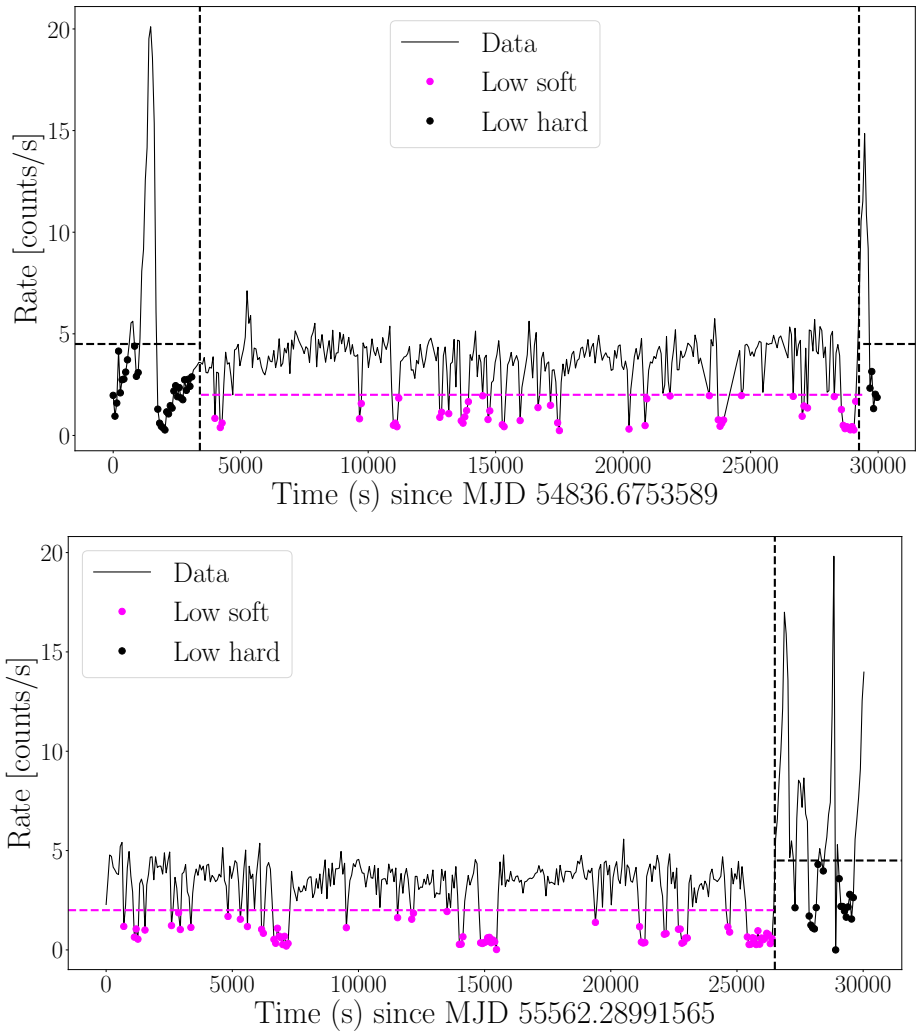

Figure 3.3: Top: EPIC-pn light curve (Obs. ID. 0551430401) in the 0.3-10 keV band with a time binning of 70 s. Bottom: EPIC-pn light curve (Obs. ID. 0656780901) in the 0.3-10 keV band with a time binning of 70 s. Magenta points refer to low-soft mode, while black points refer to low-hard mode.

respectively. For the low-soft and low-hard spectral analysis we defined the region between 0.0-4.5 cts s^{-1} as the low-hard mode. As seen in Fig. 3.3 low-hard modes are observed following flares and are selected only during the time intervals 54836.67414139-54836.70128259 MJD and 54837.01239370-54837.02171083 MJD for Obs. ID. 0551430401, 55562.61031037-55562.64217380 MJD for Obs. ID. 0656780901.

Spectra were extracted using intervals indicated above only for the first two observations because in the third observation the source was in a rotation-powered quiescent state. Redistribution matrix files (RMF) and ancillary response files (ARF) were extracted using `rmfgen` and `arfgen` tasks for all the spectra. ARF and RMF files for MOS1 and MOS2 data were summed for each observation. EPIC spectra were rebinned with FTOOL `grppha` in order to have 30 counts/bin. EPIC-MOS data were fitted in the 0.3-10 keV energy range, while (timing) EPIC-pn data in the 0.6-10 keV range.

We used XSPEC version 12.9.1p [Arnaud, 1996] for fitting our data. In order to give a possible physical interpretation of state changes, we separated *XMM-Newton* data into a flare mode (2 ks), a high mode (37 ks), a pure low mode (low-soft, 7 ks), and quiescent state (34 ks).

We corrected all the spectra for the absorption using `tbabs` model [Wilms et al., 2000] with `vern` cross sections [Verner et al., 1996] and `wilm` abundances. We used the same absorbing column density for all the observations in the propeller-ejection model and in the shock emission model.

3.10 Spectral fitting

3.10.1 Propeller-ejection scenario

In the spectral fit of high and low modes (see Fig. 3.4), mainly due to poorer statistics as compared to J1023, we have to exclude the

disc component since it is too weak and is not required to model the overall spectrum. We only estimate a limit for the disc temperature and the inner disc radius (see Table 3.5). This has been estimated by adding this spectral component to the fit and derive the corresponding upper limits. The *XMM-Newton* spectral fit with the composite model described in Section 3.7.1 (excluding the accretion disc) worked well with $\chi^2_{red} = 1.09$ for 2276 degrees of freedom[2] (see Table 3.5 and Fig. 3.4), resulting in a null hypothesis probability of 0.1%.

During the propeller state of J12770 (i.e. the high mode) the emission is dominated by a non-thermal component ($\sim$ 97%) described by a power law with index $\Gamma = 1.46 \pm 0.04$ (error calculated with $\Delta\chi^2$=2.71). A very small fraction of the flux ($\sim$ 3%) is given by the NS thermal emission. In the radio-ejection state (i.e. the low-soft mode) the radio pulsar turned on and its flux contribution, due to non-thermal emission, achieved $\sim$ 18% of the total unabsorbed flux. This contribution is described by a power law with index $\Gamma_P = 1.0 \pm 0.1$. The dominant flux contribution ($\sim$ 81%) also in this state is described by a power law with index $\Gamma = 1.67 \pm 0.07$. A very low contribution ($\sim$ 1%) is given by the NS thermal emission. In the radio pulsar state (i.e. the quiescence) the non-thermal emission is described by the same (by definition of the model) power law with Γ_P. This emission could come from the radio pulsar magnetosphere or from shocks, since we observed a modulation of X-ray emission at the orbital period. The NS thermal component contributed to 5.4% of the total flux. One might wonder if all these spectral components are needed. Indeed, they are all needed as far as are nested as specified in Section 3.7.1. The weakest component present in all the spectra is the thermal emission from the NS. Its significance is estimated to 4.4-σ, by means of

[2]The statistics of the spectra is very high. In this situation, calibration uncertainties play a role. It is common practice to add (in quadrature) a 2% systematic uncertainty to each spectral channel, as recommended in Smith et al. (2015) (see `http://xmm2.esac.esa.int/docs/documents/CAL-TN-0018.pdf`).

Table 3.5: Spectral fit parameters of J12270 using the first composite model presented in Section 3.7.1. The fit provides a $\chi^2_{\rm red}$= 1.09 for 2276 degrees of freedom with an additional systematic error of 2%. For each parameters errors are 90% confidence level ($\Delta\chi^2$ =2.71). NS emission radius is computed assuming a 1.4 kpc source distance, a 1.4 $M_\odot$ NS mass and a 10 km NS radius.

Parameter	High mode	Low mode	Quiescence
N_H (10^{20} cm^{-2})	$9.5^{+1.2}_{-1.1}$	tied all	tied all
Power law Γ	1.46±0.04	1.67 ± 0.07	-
Disc T (*) (eV)	<100	<89	-
Disc norm N_d (*)	>220	>339	-
NS atmos. T (eV)	193^{+42}_{-73}	97^{+22}_{-28}	tied Low mode
NS atmos. Radius (km)	1.0^{+6}_{-1}	tied all	tied all
NS power law Γ_P	-	1.0 ±0.1	tied Low mode

(*) We estimated an upper limit for the disc components excluding them from the fit since the inefficient disc component is too weak for being constrained.

an F-test.

3.10.2 Shock emission scenario

In the shock emission scenario, as discussed in Section 3.7.2, we considered all modes (i.e. flare, high, low modes and quiescence, see Fig. 3.5). Following Campana et al. [2019] for J1023, we first selected only MOS data because the low energy part of the X-ray spectrum is very important to model the hot absorption component (modelled within XSPEC with `zxipcf`). However, the statistics of the J12770 spectra is lower and the Galactic absorption higher with respect to the J1023 dataset to constrain this hot component. At variance with J1023, lacking here the soft absorption component, we included in the

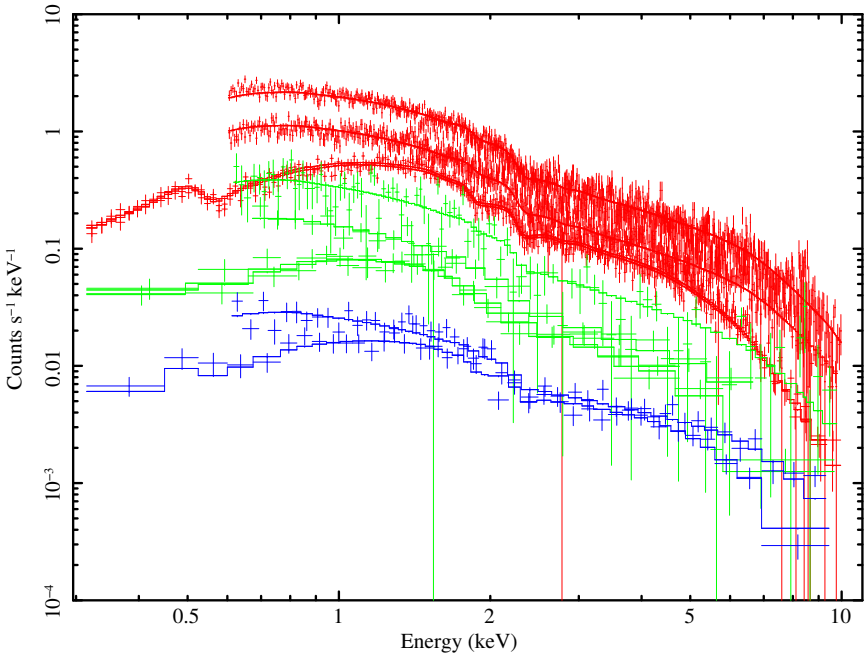

Figure 3.4: *XMM-Newton* EPIC-pn and EPIC-MOS spectra. Spectral fit of the propeller-ejection model. Red spectra are referred to the high mode, green spectra to the low mode, and blue one to the quiescent state. Spectra in energy range 0.6-10 keV are referred to the pn camera and spectra in energy range 0.3-10 keV are referred to the MOS camera.

spectral fits also the pn data. Therefore, we used exactly the same data for both scenarios for quiescence, low, and high mode data. Figure 3.5 and Table 3.6 show the result of the composite spectral model described in Section 3.7.2 using both pn and MOS data. The spectral fit has a $\chi^2 = 1.07$ for 2877 degrees of freedom, with a null hypothesis probability of 0.2% (including a 2% systematic uncertainty). The NS emission, even if present in all states, appears significant only in the low mode and during the quiescence. In the low luminosity mode the magnetospheric emission achieved the 16.9% of the total unabsorbed flux, while during the quiescence the 93.5% (see Table 3.7). This non-thermal component is parametrised by a power law with a hard spectral index $\Gamma_{\rm mag} = 1.0 \pm 0.1$. By construction, being the pulsar always active, the unabsorbed flux coming from the magnetospheric component is constant in high mode, low mode and quiescence ($\sim$0.9 $\times 10^{-12}$ erg s^{-1} cm^{-2}). Instead, the NS thermal component is irrelevant in the flare and high modes. It gives a low contribution in the low mode ($\sim$1%) and the 7% of the total unabsorbed flux during the quiescence. The NS emission region has a temperature of 110^{+45}_{-100} eV and the fraction of surface emitting is $f > 0.01$. In the flare and high luminosity modes the major flux contribution (99.3% and 97.2%) is given by the second power law, associated with the shock emission. The relative spectral indices are $\Gamma_{\rm shock} = 1.61 \pm 0.02$ for the flare mode and $\Gamma_{\rm shock} = 1.54 \pm 0.01$ for the high mode. The high mode spectral index is consistent with the photon index $\Gamma = 1.5$ predicted by a simple model of shock heating followed by fast synchrotron cooling of the post-shock plasma [Veledina et al., 2019]. Also in this model the weakest component present in all the spectra is the thermal emission from the NS. Its significance is 3.3-σ, by means of an F-test.

The residuals of the fit show the presence of a weak emission line close to 6.5 keV, that could indicate the presence of Kα emission line during the X-ray active state. This line is expected in an accretion disc. We added a Gaussian to fit this component, with a line width

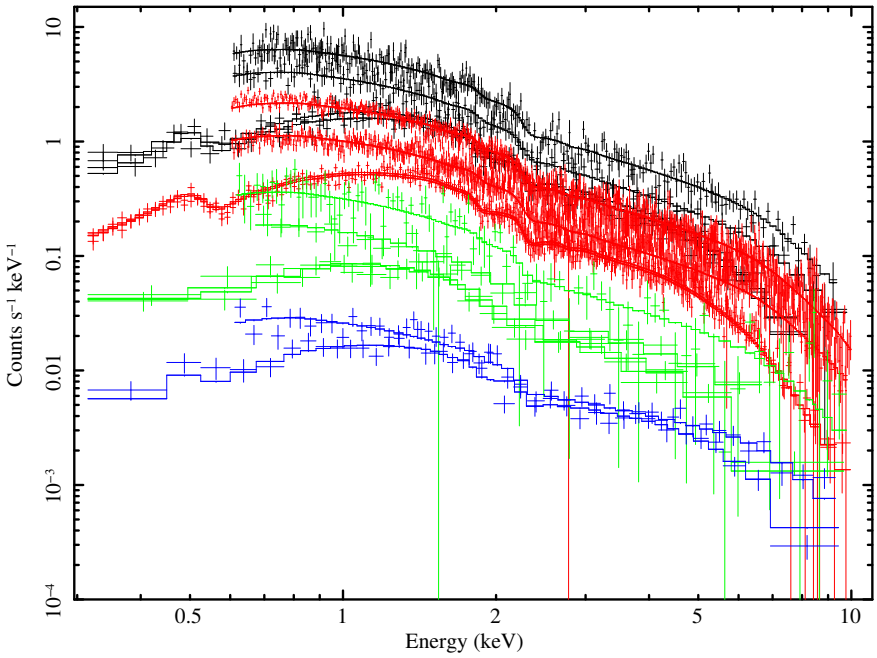

Figure 3.5: *XMM-Newton* EPIC-MOS spectra. Spectral fit of the shock emission model. Black spectra are referred to the flare mode, red spectra to the high mode, green spectra to the low mode, and blue one to the quiescent state. Spectra in energy range 0.6-10 keV are referred to the pn camera and spectra in energy range 0.3-10 keV are referred to the MOS camera.

Table 3.6: Spectral fit parameters of J12270 using the second composite model presented in Section 3.7.2. The fit provides a $\chi^2_{\rm red} = 1.07$ for 2877 degrees of freedom with an additional systematic error of 2%. For each parameters errors are 90% confidence level ($\Delta\chi^2$ =2.71).

Parameter	Flare mode	High mode	Low mode	Quiescence
N_H (10^{22} cm^{-2})	0.103± 0.005	tied all	tied all	tied all
Power law $\Gamma_{\rm shock}$	1.61±0.02	1.54 ±0.01	1.68 ±0.07	-
Thermal comp. $\log(T/K)$	tied all	tied all	tied all	$6.10^{+0.17}_{-0.38}$
Emitting fraction f	tied all	tied all	tied all	$0.008^{+0.35}_{-0.006}$
NS power law $\Gamma_{\rm mag}$	tied all	tied all	tied all	1.0±0.1

fixed to zero, consistent with the instrumental spectral resolution. The Kα line equivalent widths are equal to 65 eV in the flare mode, 59 eV in the high mode, and 362 eV in the low mode. We allowed the line normalisation to take negative and positive values in order to assess the Fe Kα significance via the F-test [Protassov et al., 2002]. The spectral fit improved significantly with the additional Gaussian component ($\Delta\chi^2$=23 for 3 degrees of freedom). The presence of this component is then supported by the F-test whose $p-$value is 5.8×10^{-5} (equivalent to 3.9-σ). A more detailed study on statistical significance would require Monte Carlo simulations as presented in Kosec et al. [2018]. We note that for such a large $\Delta\chi^2$ the line is always highly significant.

Finally, we tested what happens if we leave free the absorption column density in the flare mode: the two values (flare and all the other modes) are fully consistent.

3.10.3 Soft and hard low modes

Concerning the analysis of low-soft and low-hard modes, we tried the three spectral models discussed in Section 3.7.3. The first model with the additional bremsstrahlung emission (see Section 3.7.3) does not

Table 3.7: 0.3-10 keV flux of the three different luminosity modes and quiescence of J12270. Percentage of the contribution of spectral components in the first and the second model. Fluxes refer to the mean of the MOS detectors. Unabsorbed luminosities are calculated assuming a distance equal to 1.4 kpc.

Parameter	Total/ spectral components	Flare mode	High mode	Low mode	Quiescence
			Propeller-ejection model		
Absorbed flux (10^{-12} erg s^{-1} cm^{-2})	Total	-	$16.5^{+0.9}_{-0.9}$	$2.4^{+0.2}_{-0.2}$	$0.43^{+0.02}_{-0.03}$
Percentage of contribution to the unabsorbed flux	Power law		97.2 %	81.1 %	-
	Ineffic. disc(*)		0.0 %	0.0 %	-
	NS thermal		2.8 %	1.1 %	5.4 %
	Magn. Power law		-	17.8 %	94.6 %
Unabsorbed flux (10^{-12} erg s^{-1} cm^{-2})	Total	-	18.1	2.7	0.46
Luminosity (10^{32} erg s^{-1})	Total	-	42.2	6.2	1.1
			Shock model		
Absorbed flux (10^{-12} erg s^{-1} cm^{-2})	Total	$36.3^{+1.1}_{-1.1}$	$16.3^{+0.2}_{-0.2}$	$2.4^{+0.1}_{-0.1}$	$0.43^{+0.03}_{-0.04}$
Percentage of contribution to the unabsorbed flux	Shock emission	99.3%	97.2%	81.8%	-
	NS thermal	0.0%	0.2%	1.3%	6.5%
	Magnetospheric emission	0.7%	2.6%	16.9%	93.5%
Unabsorbed flux (10^{-12} erg s^{-1} cm^{-2})	Total	40.9	18.1	2.7	0.46
Luminosity (10^{32} erg s^{-1})	Total	95.5	42.4	6.4	1.1

(*) We obtained only an upper limit on the 0.3-10 keV flux of the thermal inefficient disc component. Fluxes refer MOS data.

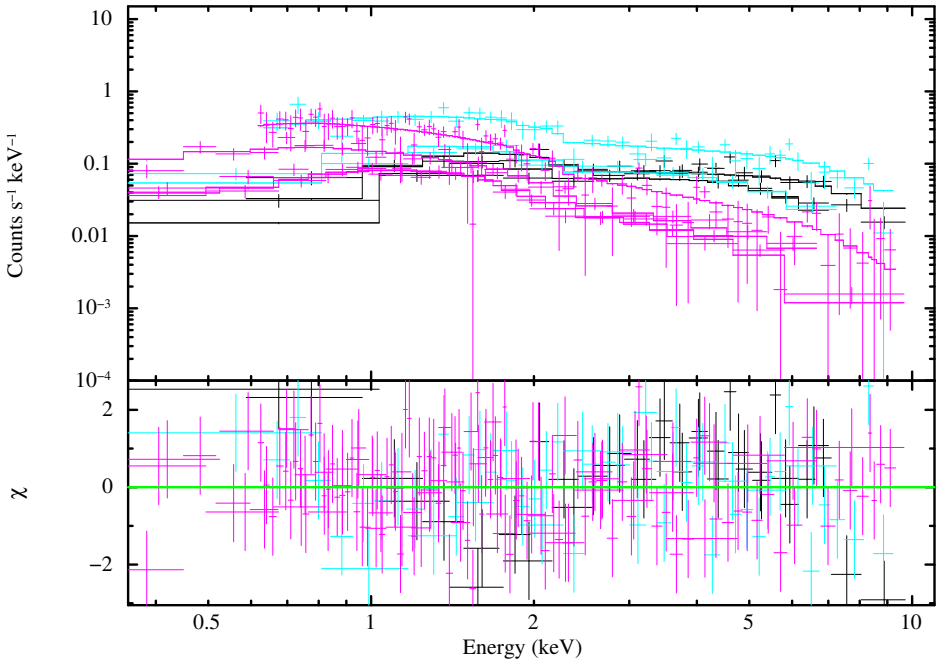

Figure 3.6: *XMM-Newton* EPIC-pn and EPIC-MOS spectra. Black spectra are referred to the low-hard mode (Obs. ID. 0551430401), light blue spectra to the low-hard mode (Obs. ID. 0656780901) and magenta one to the low-soft mode. Spectra in energy range 0.6-10 keV are referred to the pn camera and spectra in energy range 0.3-10 keV are referred to the MOS camera. The residuals are plotted in the low panel.

Table 3.8: Spectral fit parameters of J12270 low mode spectra (see Section 5.3). Errors are 90% confidence level ($\Delta\chi^2$ =2.71) for each parameters. The fit provides a $\chi^2_{\rm red} = 1.20$ with 237 degrees of freedom.

Parameter	Low-soft mode	Low-hard mode (ID. 0551430401)	Low-hard mode (ID. 0656780901)
N_H (10^{22} cm^{-2})	0.11±0.03	$0.8^{+0.3}_{-0.2}$	$0.20^{+0.1}_{-0.1}$
Power law Γ_1	1.62 ± 0.09	tied all	tied all
Power law Γ_2	–	$0.2^{+0.2}_{-0.2}$	$0.5^{+0.1}_{-0.2}$

reproduce the data: for `mekal` model we got $\chi^2_{\rm red} = 3.97$ for 238 degrees of freedom. The addition of a black body or a second power law to the power law did not produce an acceptable fit either: $\chi^2_{\rm red} = 1.51$ or $\chi^2_{\rm red} = 1.76$ for 239 degrees of freedom, respectively.

We then left the column density of the low-hard spectra free to vary with respect to the low-soft spectra. The fit with the addition of a black body worked well, with a $\chi^2_{\rm red} = 1.05$ for 238 degrees of freedom and a null hypothesis probability of 27.7%. However, the radius of the emitting region is very small ($\sim$ 1 km) and with a very high temperature ($\sim 10^7$ K). The physical reason for such a small radius and high temperature is difficult to envisage.

The best composite model is the one with the sum of two power laws and free column density for the low-hard spectra. The spectral fit (see Fig. 3.6 and Table 3.8) has a $\chi^2_{\rm red} = 1.20$ for 237 degrees of freedom and a null hypothesis probability of 1.7%. The absorption N_H in the low-hard mode is consistent with the low-soft one for the second observation and much higher (factor of $\sim 7-10$) during the first observation. This is hard to interpret, too. The first power law, equal for the two modes (low-hard and low-soft), has an index $\Gamma_1 = 1.62 \pm 0.09$, consistent with the value $\Gamma = 1.67 \pm 0.07$ computed in the propeller-ejection scenario in the low mode (see Table 3.5) and with $\Gamma_{\rm shock} = 1.68 \pm 0.07$ in the shock emission scenario (see Table 3.6).

Table 3.9: Spectral fit parameters of J12270 using the first composite model presented in Section 3.7.1. The fit provides a $\chi^2_{\rm red}$= 1.1 for 2255 degrees of freedom with a a null hypothesis probability of 0.08 % and an additional systematic error of 2%. For each parameters errors are 90% confidence level ($\Delta\chi^2$ =2.71). NS emission radius is computed assuming a 1.4 kpc source distance, a 1.4 $M_\odot$ NS mass and a 10 km NS radius.

Parameter	High mode	Low mode	Quiescence
N_H (10^{20} cm^{-2})	$9.6^{+1.2}_{-1.1}$	tied all	tied all
Power law Γ	$1.47^{+0.03}_{-0.04}$	$1.78^{+0.28}_{-0.18}$	-
Disc T (*) (eV)	<100	<89	-
Disc norm N_d (*)	>220	>339	-
NS atmos. T (eV)	188^{+43}_{-73}	99^{+33}_{-40}	tied Low mode
NS atmos. Radius (km)	1.0^{+7}_{-1}	tied all	tied all
NS power law Γ_P	-	1.0 $\pm$0.1	tied Low mode

(*) We estimated an upper limit for the disc components excluding them from the fit since the inefficient disc component is too weak for being constrained.

The second power law varies for the two low-hard spectra and in both cases is very hard with an index $\Gamma_2 = 0.2 \pm 0.2$ for the first observation (Obs. ID. 0551430401) and $\Gamma_2 = 0.5^{+0.1}_{-0.2}$ for the second observation (Obs. ID. 0656780901).

3.10.4 Spectral fittings with brighter quiescent observation

Here we report the spectral fit parameters of J12270 using the brighter quiescent observation (Obs. ID. 0729560801) instead of the fainter one (Obs. ID. 0727961401). This observation performed on 2014 June 27 (see Table 3.4) was made in fast timing mode with the EPIC-pn

Table 3.10: Spectral fit parameters of J12270 using the second composite model presented in Section 3.7.2. The fit provides a $\chi^2_{\rm red} = 1.07$ for 2856 degrees of freedom with a a null hypothesis probability of 0.3 % and an additional systematic error of 2%. For each parameters errors are 90% confidence level ($\Delta\chi^2$ =2.71).

Parameter	Flare mode	High mode	Low mode	Quiescence
N_H (10^{22} cm^{-2})	0.106± 0.006	tied all	tied all	tied all
Power law $\Gamma_{\rm shock}$	1.62±0.02	1.57 ±0.02	$1.93^{+0.28}_{-0.20}$	-
Thermal component $\log(T/K)$	tied all	tied all	tied all	$6.24^{+0.15}_{-0.26}$
Emitting fraction f	tied all	tied all	tied all	$0.005^{+0.02}_{-0.004}$
NS power law $\Gamma_{\rm mag}$	tied all	tied all	tied all	0.9±0.1

camera and in imaging full window mode using thin filters with the EPIC-MOS cameras. In these spectral fits we selected only MOS data because during quiescence the source is too faint to be detected with EPIC-pn camera operating in timing mode. In Table 3.9 we report the results of the first composite model presented in Section 3.7.1 and in Table 3.10 the results of the second composite model described in Section 3.7.2. Spectral parameters change by less than 10% using the second observation during the quiescence.

3.11 Conclusions – Part II

We analysed the X-ray spectra in the 0.3-10 keV range of the transitional pulsar XSS J12270−4859. Our observations were taken before and after the state transition from X-ray active state to quiescence (radio pulsar) state, which took place in Nov-Dec 2012.

We proposed two different physical scenarios to explain the rapid variability between high and low modes. In the first scenario, the high-low mode transitions are accounted for by propeller to radio-ejection states (with the X-ray pulsations accretion-powered), in the second

scenario (shock emission scenario) by an approaching or receding inner disc just outside the light cylinder (with the X-ray pulsations rotation-powered).

These scenarios were developed for J1023 (Campana et al. 2016; Campana et al. 2019). The two spectral models fit the overall set of *XMM-Newton* observations sufficiently well, especially considering the large amount of data. There is a slightly small statistical preference for the shock emission scenario. At variance with J1023, we do not detect here the presence of an accretion disc in the propeller-radio ejection scenario, nor do we find signs of a hot absorber in the shock emission scenario. This is mainly due to the lower statistics with respect to J1023, which continues to be in the X-ray active state, whereas J12270 is now in the quiescent state. Contrary to J1023, we find signs of the presence of an iron Kα emission line close to 6.5 keV, in the shock emission scenario. This might originate in the innermost region of the accretion disc.

Another difference with J1023 is the presence of two different spectral instances of the low mode. We performed a spectral analysis by comparing the different spectral shapes during the low-soft and low-hard modes, in order to try to understand the physical process that drives the spectral change. We considered a spectral model with one component common to the two modes and an additional one for the low-hard mode only. We took a power law as common component. Only the addition of a second power law spectrum for the low-hard mode (see Table 3.8) and a variable absorption column density gave acceptable spectral fits. We think that this harder component can be correlated with the tail of the flare emission, even if the variable absorption is difficult to explain.

It is important to note that a transition to the low mode occurred also during a flare. This implies that the emission mechanism related to low mode is able to temporarily stop or at least perturb the flare, even if not completely, since some emission remains (i.e. low-

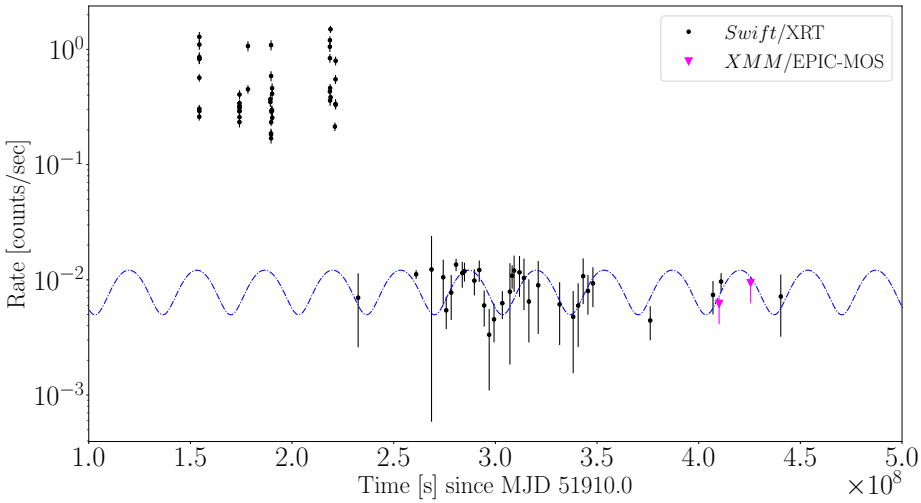

Figure 3.7: *Swift*/XRT count rate light curve of J12270. The two *XMM-Newton* observations were plotted with magenta triangles. These data were extrapolated to XRT counts through spectral modelling, including the uncertainty in the *XMM-Newton* flux. The overall X-ray light curve shows J12270 bright in the X-ray band at early times, and then a turn off to quiescence. During quiescence, a clear variability is apparent in the light curve.

hard mode). After this, the flare is able to restart again, so that the quenching induced by the low mode transition is not ultimate. At the same time a tail or a residual emission of the flare is still present during the low-hard mode, meaning that the quenching is not complete or instantaneous. This provides a clear indication that flares are unrelated to high-and-low mode transitions.

J12270 is currently in its quiescent state, with pulsations detected in the radio band outside extended eclipses close to the pulsar's superior conjunction. In our analysis we excluded the last *XMM-Newton*

observation (Obs. ID. 0729560801), performed in the radio pulsar state since it shows a slightly increased flux (factor ~ 1.6) with respect to a similar observation (Obs. ID. 0727961401) taken one year before during the radio pulsar state. We discarded this observation, because our primitive scenarios allows only for a fixed quiescent luminosity. We investigated in more details this puzzling behaviour. We built the *Swift* XRT light curve with the on-line generator[3] [Evans et al., 2009] (see Fig. 3.7). Interestingly, the quiescent light curve shows a variability by $\sim 40\%$ in the count rate. We also converted the two quiescent *XMM-Newton* fluxes into XRT count rates, including in the error budget the uncertainties in the flux, providing two more points. The *XMM-Newton* count rate was converted into a *Swift*/XRT rate using PIMMs (v4.10b) and the above spectral parameters, and including the error on the *XMM-Newton* flux (conveying the spectral fit uncertainties), which provides the major contribution to the error budget. A fit with a constant value provides an unsatisfactory fit with a reduced $\chi^2 = 1.8$ with 34 d.o.f. A sinusoidal modulation provides a $3.5\,\sigma$ improvement in the fit by means of an F-test ($\chi^2 = 1.1$ with 31 d.o.f.). The period is 387 ± 7 d. We note that the two *XMM-Newton* observations almost sample the entire rate variability. We can only speculate on the nature of this putative periodicity, whose interpretation is not straightforward. One possibility is the precession of the NS with an asymmetric relativistic wind, which will then interact with different efficiencies with the material outflowing from the companion. Further observations and monitoring would be needed to better investigate this periodicity.

[3] `https://www.swift.ac.uk/user_objects/`

4

Eclipsing millisecond pulsars

The work presented in this chapter is published in the following article:

- **Miraval Zanon, A.**; D'Avanzo P.; Ridolfi A.; Coti Zelati F.; Campana S.; Tiburzi C.; de Martino D.; Muñoz Darias T.; Bassa C.G.; Zampieri L.; Possenti A.; Ambrosino F.; Baglio M.C.; Burgay M.; A. Burtovoi, Michilli D.; Papitto A.; Zucca P.; *"Evidence of intra-binary shock emission from the redback pulsar J1048+2339"*; accepted for publication to A&A, `https://arxiv.org/abs/2103.06317`

4.1 Evidence of intrabinary shock emission from the redback pulsar J1048+2339

We present simultaneous multi-wavelength observations of the 4.66 ms redback pulsar PSR J1048+2339. We perform phase-resolved spectroscopy with the ESO-VLT in order to search for signatures of a residual accretion disc and/or intra-binary shock emission, constrain the companion radial velocity semi-amplitude (K_2), and estimate the neutron star mass ($M_{\rm NS}$). Using the FORS2-VLT intermediate-resolution spectra we measure a companion velocity of $291 < K_2 < 348\,{\rm km\,s^{-1}}$ and a binary mass ratio of $0.209 < q < 0.250$. Combining our results for K_2 and q we constrain the mass of the neutron star and the companion to $(1.0 < M_{\rm NS} < 1.6)\sin^{-3}i\,M_\odot$ and $(0.24 < M_2 < 0.33)\sin^{-3}i\,M_\odot$, respectively, where i is the system inclination. The Doppler map of the Hα emission line exhibits a spot feature at the expected position of the companion star and an extended bright spot close to the inner Lagrangian point. We interpret this extended emission as the effect of an intra-binary shock originating from the interaction between the pulsar relativistic wind and the matter leaving the companion star. The mass loss from the secondary star could be either due to Roche-lobe overflow or to the ablation of its outer layer by the energetic pulsar wind. Contrastingly, we find no evidence for an accretion disc. We report on the results of SRT and LOFAR simultaneous radio observations at three different frequencies (150 MHz, 336 MHz and 1400 MHz). No pulsed radio signal is found in our search. This is probably due to both scintillation and the presence of material expelled from the system which can cause the absorption of the radio signal at low frequencies. The confirmation of this hypothesis is given by another SRT observation (L-band) taken in 2019, in which a pulsed signal is detected. Finally, we report on an attempt to search for optical pulsations using IFI+Iqueye mounted at the 1.2 m Galileo telescope at the

4.1. EVIDENCE OF INTRABINARY SHOCK EMISSION FROM THE REDBACK PULSAR J1048+2339

Asiago Observatory.

Introduction

PSR J1048+2339 (hereafter J1048) was discovered with the Arecibo telescope in a search for high-latitude Fermi unidentified sources [Cromartie et al., 2016]. Deneva et al. [2016] classified it as a RB system using multi-wavelength observations. J1048 is a 4.66-ms-spinning NS with a spin-down power of 1.2×10^{34} erg s^{-1}. It is part of a tight binary system with an orbital period of 6.01 hours and it is located at a distance of about 1.7 kpc [Deneva et al., 2020]. Its companion star has a mass of $\sim$0.4 $M_{\odot}$ and an effective temperature $T_{eff} \sim 4200$ K [Yap et al., 2019]. The inclination of the system is not well-constrained. Yap et al. [2019] fix the inclination to a theoretical upper limit of 76° because X-ray eclipses in *Chandra* data are not observed. Contrastingly, spectroscopic studies from Strader et al. 2019 show that either the system must be close to edge-on ($i \geq 83^{+7}_{-10}$ degrees), or the pulsar mass must be higher than 2 $M_{\odot}$. The system exhibits radio eclipses for a large fraction of the orbit ($\sim$50 %, Deneva et al. 2016, 2020). The radio pulsar has a γ-ray counterpart, 4FGL J1048.6+2340, which shows γ-ray pulsations at a statistical significance of $\sim8\sigma$ [Deneva et al., 2020]. Optical and X-ray studies [Cho et al., 2018, Yap et al., 2019] reveal a strong orbital modulation with rapid variations: the optical light curve changes from an ellipsoidal to a sinusoidal-like profile in less than 14 days. The average optical magnitudes when the pulsar wind heating dominates are $r' \sim 19.4$ mag and $g' \sim 20.7$ mag [Yap et al., 2019]. Instead, when the orbital modulation is dominated by ellipsoidal modulation, the system is fainter by 0.3-0.4 mag. The X-ray light curve is also strongly modulated with a minimum centered at $\phi = 0.0$, which corresponds to the inferior conjunction of the companion star in our convention. Optical spectra acquired with the 4-m SOAR telescope show the most intense variability yet observed for any RBs

[Strader et al., 2019]. The strong emission lines in some instances appear double-peaked, sometimes single-peaked and are absent at other orbital phases. The multi-epoch poor orbital phase sampling precludes a secure origin of the emission lines region.

In this Chapter we present a multi-wavelength campaign of J1048. Using Very Large Telescope (VLT), Sardinia Radio Telescope (SRT), Low-Frequency Array (LOFAR) telescope, Galileo telescope and *Swift* simultaneous observations carried out during the radio pulsar state, we study the kinematics and geometry of matter in this interacting binary system. In Sect. 4.2 we describe our data set and data reduction steps. In Sect. 4.3 we present the average spectrum, the variability of Hα emission line and the optical light curve, while the radial velocity curves are presented in Sect. 4.4. In Sect. 4.5 we show the Hα Doppler tomography. Sects. 4.6-4.7 are dedicated to radio and optical timing analysis. In Sect. 4.8, we discuss the results and we present future perspectives.

4.2 Observations

In March 2020, we performed a multi-wavelength campaign focused on J1048 with simultaneous observations in the X-ray, UV, optical and radio bands. Table 3.3 lists the observations analysed and discussed in this work. In the following, we describe the data analysis for the different data sets acquired.

4.2.1 Optical and ultraviolet observations

Very Large Telescope

Optical spectroscopic observations of J1048 were carried out on March 19, 2020 at the Observatorio Monte Paranal, using the ESO 8.2 m Antu

Table 4.1: Summary of the observations of PSR J1048+2339.

Telescope/ Instrument	Mode	Band	Start time (UTC)	Exposure (s)
VLT/FORS2	Imaging	R-band	2020 Mar 19 00:49:07	200
VLT/FORS2	grism 1200R+93	575 - 731 nm	2020 Mar 19 00:59:40	19200
SRT-1	Baseband/Search	P(0.3-0.4 GHz)/L(1.3-1.8 GHz)	2019 Aug 26 14:20:28	5400
SRT-2	Baseband/Search	P(0.3-0.4 GHz)/L(1.3-1.8 GHz)	2020 Mar 18 20:10:50	29960
LOFAR	Raw voltages	110-188 MHz	2020 Mar 18 21:01:00	25200
Swift/XRT	Photon Counting	0.3–10 keV	2020 Mar 18 21:43:14	3611
Swift/UVOT	Imaging	$U, B, V, UVW1, UVM2, UVW2$	2020 Mar 18 21:43:18	3475
Galileo/Iqueye	Fast timing	400 - 700 nm	2020 Mar 18 23:26:33	9000

Telescope (UT1) equipped with the FORS2 Spectrograph [Appenzeller et al., 1998]. During the night, the seeing ranged between $0.6 - 0.9''$, with most of the time stable between $0.7 - 0.8''$. A total of sixteen spectra were obtained, covering a complete orbital cycle, using 1200 s long exposures. We used a $1''$ slit, always oriented along the parallactic angle, and the grism and the grism 1200R+93, centered at 6500 Å and with a dispersion of 0.76 Å/pixel. In order to extract the optical light curve, we acquired one or two R-band images with 20 s exposure time, once every two spectroscopic acquisitions, for a total of 10 images.

Image reduction was carried out following standard procedures: subtraction of an averaged bias frame, division by a normalised flat frame. Astrometry was performed using the USNOB1.0 catalogue[1]. Aperture photometry was made with the PHOTOM software part of the STARLINK[2] package. The photometric calibration was done against Stetson standard stars [Stetson, 2000]. In order to minimize any systematic effect, we performed differential photometry with respect to a selection of local isolated and non-saturated reference stars. The reduction and extraction of the spectrum was performed with the ESO-FORS pipeline[3] and the ESO-MIDAS[4] software package. Wavelength and flux calibration of the spectra were achieved using helium-argon lamp and observing spectrophotometric standard stars, respectively, at the beginning and end of the observing run. We further checked stability of the wavelength calibration using night-sky emission lines.

For the cross-correlation of the spectra with late-type templates and the Doppler tomography analysis we employed the MOLLY pack-

[1] http://tdc-www.harvard.edu/catalogs/ub1.html

[2] http://starlink.eao.hawaii.edu/starlink

[3] https://www.eso.org/sci/software/pipelines/fors/fors-pipe-recipes.html

[4] https://www.eso.org/sci/software/esomidas/

age developed by Tom Marsh[5] and the `pydoppler`[6] package [Spruit, 1998], respectively.

Galileo telescope

We observed J1048 with IFI+Iqueye mounted at the 1.2 m Galileo telescope in Asiago, Italy. Iqueye+[7] is a fast photon counter with a field of view of 12.5 arcsec and the capability of time tagging the detected photons with sub-ns time accuracy [Naletto et al., 2009]. The instrument is fiber-coupled with the Galileo telescope by means of a dedicated instrument, the Iqueye Fiber Interface (IFI; Zampieri et al. 2019a). A total of 3 acquisitions (obs. ID 20200319-002631, 20200319-020229, 20200319-032617) were performed on March 18–19, 2020, between 23:26:33.4 and 02:56:18.0 UTC. The first two acquisitions lasted 3600 s and the third 1800 s. The sky background was regularly monitored between on-target observations. The average rate at the position of the pulsar varied between ~ 1300 and ~ 1600 counts s^{-1} because of variations in the sky background. The companion star is not significantly detected.

The data reduction is performed with a dedicated software[8]. The whole acquisition and reduction chain ensures an absolute accuracy of ~ 0.5 ns relative to UTC [Naletto et al., 2009]. The photon arrival times are barycentered using TEMPO2 in TDB time units [Hobbs et al., 2006] and the JPL ephemerides DE421. The position of the pulsar is RA=10:48:43.4183, DEC=+23:39:53.411 at MJD 56897.0 [Deneva et al., 2016]. We corrected for the motion of the pulsar along the orbit using the orbital period $P_b = 0.25051904499812022$ days and projected semi-major axis $x_p = 0.836122$ light-seconds of Deneva

[5] `http://deneb.astro.warwick.ac.uk/phsaap/software/`
[6] `https://github.com/Alymantara/pydoppler`
[7] `https://web.oapd.inaf.it/zampieri/aqueye-iqueye/index.html`
[8] QUEST v. 1.1.5, see Zampieri et al. [2015].

et al. [2016], while the time of passage at the ascending node $T_{\rm asc}$ = 58721.666409 MJD (Barycentric Dynamical Time) was derived from a SRT observation on August 19, 2019 (see Sect. 4.6).

Swift/**UVOT**

The Ultraviolet Optical Telescope (UVOT) [Roming et al., 2005] onboard the Neil Gehrels *Swift* Observatory [Gehrels et al., 2004] observed J1048 with the U (λ_c= 346.5 nm), B (λ_c= 439.2 nm), V (λ_c= 546.8 nm), $UVW1$ (λ_c= 260.0 nm), $UVM2$ (λ_c= 224.6 nm), and $UVW2$ (λ_c= 192.8 nm) filters for ∼3.4 ks on March 18–19, 2020 (see Table 4.2). We performed aperture photometry by using a circular region centered on the source with a radius of 5″ for the UV filters and 3″ for the optical filters. The background emission was extracted from a nearby source-free region. The target was not detected in any of the images. Using the tool `uvotsource` of the *Swift* analysis software in the HEASoft package version 6.28[9], we estimated the following 3σ upper limits on the optical/UV magnitude: $U > 19.9$ mag, $B > 20.3$ mag, $V > 19.3$ mag, $UVW1 > 19.5$ mag, $UVM2 > 19.6$ mag, and $UVW2 > 20.1$ mag (Vega system).

4.2.2 Radio observations

We observed J1048 on two different occasions in the radio band.

On August 19, 2019 we used the 64-m Sardinia Radio Telescope (SRT) to carry out a 1.5-hour-long observation with the dual-band co-axial L/P receiver [Valente et al., 2010]. In the L band ($\sim 1.3 - 1.8$ GHz), the total-intensity signal was recorded every 125 μs with the Australia Telescope National Facility (ATNF) Digital Filterbank Mark III backend (DFB[10]) in search mode. The nominal bandwidth

[9] `https://heasarc.gsfc.nasa.gov/docs/software/heasoft/`

[10] `http://www.jb.man.ac.uk/pulsar/observing/DFB.pdf`

Table 4.2: Summary of the *Swift*/UVOT observations of PSR J1048+2339.

Filter	Start time (UTC)	Net exposure (s)
$UVW1$	2020 Mar 18 21:43:19	288
	2020 Mar 19 03:51:32	299
U	2020 Mar 18 21:46:45	143
	2020 Mar 19 03:53:48	149
B	2020 Mar 18 21:48:30	143
	2020 Mar 19 03:54:58	149
$UVW2$	2020 Mar 18 21:50:17	576
	2020 Mar 19 03:56:09	600
V	2020 Mar 18 21:57:07	143
	2020 Mar 19 04:00:39	149
$UVM2$	2020 Mar 18 21:58:52	383
	2020 Mar 19 04:01:49	397

was chosen to be of 1024 MHz, centered at 1548 MHz and divided into 1024 frequency channels. This setup was chosen to prevent aliasing effects within the actual receiver observing band, which is ~ 500 MHz wide. The P band was instead acquired in baseband mode with the Reconfigurable Open Architecture Computing Hardware[11] (ROACH-1) backend, recording 80 MHz of bandwidth centered at a frequency of 336 MHz. Thanks to the presence of a Gregorian cover mounted, which shields the receiver from radio signals generated by the telescope instrumentation, this observation was mostly free of Radio Frequency Interference (RFI) in both bands.

The second radio observation was carried out in the night between March 18–19, 2020. This time, J1048 was observed simultaneously with the SRT and the Low-Frequency Array telescope (LOFAR, Stappers et al. 2011, van Haarlem et al. 2013), for more than a full orbit. The SRT observation lasted ~ 8.3 hr, and was carried out using exactly the same setup as in the previous observation, with the only difference being that the Gregorian cover was not mounted. This resulted in a higher presence of RFI in these data. LOFAR started the simultaneous observation of J1048 in the VHF band ($110 - 188$ MHz) with the high-band antennae of the LOFAR core about 50 minutes later than SRT, and recorded data for 7 hr. The data were collected as beamformed, 8-bit complex voltages from the two linear polarizations, with a sampling time of 5.12 μs and divided into 400 frequency sub-bands, with a bandwidth of 0.195 MHz each.

4.2.3 X-ray observations

We analysed data sets acquired on March 18–19, 2020 using the *Swift* X-ray Telescope (XRT; Burrows et al. 2005) configured in the photon counting mode (timing resolution of 2.5 s; obs. IDs 00034285004

[11] `http://casper.ssl.berkeley.edu/wiki/ROACH`

and 00034285005). The source was observed for 3.6 ks, summing up the two pointings. The source is barely detected, with a signal-to-noise ratio of $S/N \sim 2.2$ as evaluated by the `sosta` tool in the HEASoft package. Its net count rate is $(2.0 \pm 0.9) \times 10^{-3}$ counts s^{-1} over the 0.3–10 keV energy band (uncertainty at a confidence level of 1σ). Assuming an absorbed power law model with absorption column density of $N_{\rm H} = 2.5 \times 10^{20}$ cm^{-2} and photon index of $\Gamma = 1.5$ [Cho et al., 2018], the above count rate translates into an observed flux of $(9 \pm 4) \times 10^{-14}$ erg cm^{-2} s^{-1} and an intrinsic unabsorbed flux of $(9.5 \pm 4.0) \times 10^{-14}$ erg cm^{-2} s^{-1}, or a luminosity of $(3.3 \pm 1.4) \times 10^{31}$ erg s^{-1} (0.3–10 keV) for a distance of 1.7 kpc [Deneva et al., 2020]. These values are compatible within the uncertainties with those derived by Cho et al. [2018] and Yap et al. [2019] using deeper *Chandra* observations, and indicate that, at the epoch of our multi-band campaign, the system remained in a rotation-powered radio pulsar state.

4.3 Average spectrum and orbital variability

The average optical spectrum of J1048 is dominated by absorption lines typical of late type stars (e.g. TiO λ6161, FeII λ6361 and FeII λ6494) and by the Hα emission line. It is displayed in Fig. 4.1 together with a K8 V template, HD 154712B, that well matches the absorption features (see also Sect. 4.4). One of the typical features of the accretion disc, the HeI λ6678 emission line, is absent. The Hα profile in the average spectrum is complex and appears single-peaked, casting doubts on the presence of an accretion disc.

The Hα emission shows strong variations along the orbit (Fig. 4.2): at some orbital phases it disappears (e.g. at ϕ= 0.42), while at other epochs it appears with a single component (e.g. ϕ=0.63) and sometimes it displays a weak secondary peak (ϕ=0.84). Binary phases are computed using the extremely accurate radio pulsar ephemeris (see

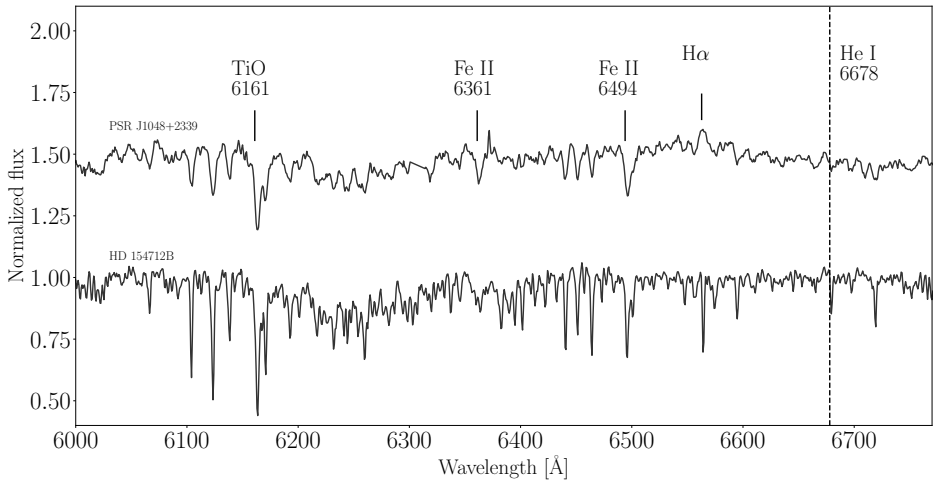

Figure 4.1: The average optical spectrum of PSR J1048+2339 (top spectrum) compared with a K8 V template (HD 154712B, bottom spectrum). Arbitrary vertical offsets have been applied for clarity. Main emission and absorption lines are indicated. The vertical black dashed line represents the rest wavelength of He I λ6678, which is absent in our spectra.

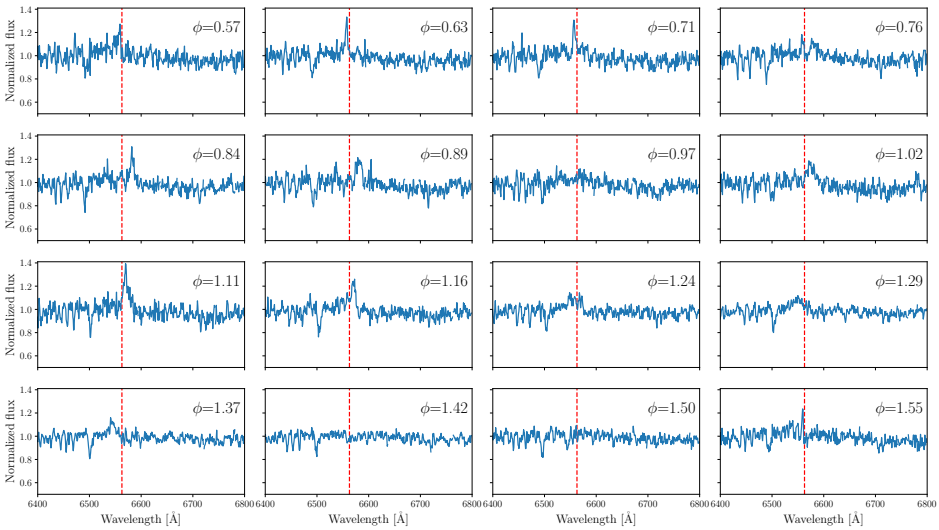

Figure 4.2: Hα emission variability along the whole orbit. The orbit phase increases from left to right, from top to bottom. The vertical red dashed line represents the H$\alpha\lambda$6561 rest wavelength. We use the convention where ϕ=0 is the point where the companion star is closer to the observer.

Sect. 4.6). Given the nearly circular orbit, the choice of the time of the ascending node $T_{\rm asc}$ is arbitrary and we opted to decrement that by $P_b/4$, where P_b is the orbital period, with respect to the one computed from radio ephemeris, so that phase 0 corresponds to the inferior conjunction of the companion star.

Differently from what was found by Strader et al. [2019], in our case the Hα emission is weak and asymmetric, with stronger blue or red components depending on the orbital phase. Near the superior conjunction (ϕ=0.4–0.5), the Hα emission has almost completely vanished or is weakly detected as an absorption feature, while near the inferior conjunction (ϕ=0) two peaks emerge (see Fig. 4.3, left plot). The blue component is weaker and associated with the companion

star that is approaching the Earth. The red component vice versa is emitted by material receding from the Earth along our line-of-sight. This could be ascribed to the material flowing from the donor star towards the pulsar. We constructed the trailed spectrogram, shown in the right panel of Fig. 4.3, to investigate in more detail the orbital line variability. It displays the orbital evolution of the Hα emission line in 16 phase bins. Between phases 0.75 and 0.90, an emission spot with positive velocities that does not trace the orbital motion of the companion star is clearly visible. This is a first indication for the presence of material overflowing from the Roche lobe, confirmed by the Doppler tomography study (see Sect. 4.5). The gas from which the Hα emission originates together with the irradiated companion star are probably responsible for the radio eclipses of J1048 that cover about half of the orbit [Deneva et al., 2016, 2020].

Measurements of the equivalent widths (EWs) of the Hα emission line show a hint of modulation at the orbital period although at low statistical significance ($\sim 1.9\sigma$, see Fig. 4.4, bottom panel). The mean EW of Hα is -3.1$\pm$1.3 Å. In the trailed spectra of Hα in Fig. 4.3 the emission is at maximum at orbital phases 0.1–0.2 and 0.6–0.7. For comparison, we measured the EWs of metallic lines (in the spectral ranges 5970–6291 Å and 6421–6522 Å). The EW curve of metallic lines shows almost a sinusoidal profile with a single peak significance at a 3.9σ, while the EW curve of Hα has a noisy profile. This might be due to the fact that the Hα line is contaminated by extended emission as hinted at by the trailed spectra (Fig. 4.3), while the metallic lines originate only from the companion star.

The simultaneous R-band light curve (Fig. 4.5) shows an asymmetric sinusoidal-like profile with a minimum around $\phi = 0$ and an average magnitude $R \sim 19.3$ mag (Vega). The peak-to-peak amplitude of the light curve is of about 0.9 magnitude. The light curve shape and the magnitude variations along the orbit suggest that the optical emission of the system is dominated by the emission from the

hot face of the companion, heated by the pulsar wind. The curve does not have a pure sinusoidal profile, the minimum is around phase zero as expected, while the maximum precedes phase 0.5.

Differently from what Linares et al. [2018] observed in the RB PSR J2215+5135, we do not find drastic changes in the spectral absorption lines of the irradiated and the cold face of the companion star (Fig. 4.6). In PSR J2215+5135, Balmer and Mg-I triplet absorption lines show strong EW variation as a function of the orbital phase due to the irradiation by the pulsar. The EWs of Balmer and Mg-I triplet absorption lines change by a factor $\simeq 7$ and $\simeq 3$, respectively [Linares et al., 2018]. Indeed, optical photometry of PSR J2215+5135 revealed single humped modulation with magnitude variations of ~ 1.5 mag along the orbit, typical of strongly irradiated system [Breton et al., 2013]. In J1048, the EWs of Hα emission line and of metallic absorption lines vary by a small factor ($\simeq 3$ and $\simeq 2$ respectively) along the orbit and we do not observe large temperature changes between the dark and bright sides of the companion star. The ~ 0.9 mag variation in amplitude observed in the R-band light curve could therefore be attributed to a moderate pulsar irradiation.

4.4 Radial velocity

Following Yap et al. [2019] we cross-correlated the 16 VLT/FORS2 spectra with six K V template stars in the spectral ranges 5970–6291 Å and 6421–6522 Å(taken from Casares et al. 1996), masking the main telluric and interstellar features and the Hα emission line, obtaining six radial velocity curves for each template star. We then performed a (least-squares) sine fit to our radial velocity data, allowing the projected radial velocity semi-amplitude (K_2) and the systemic velocity of the companion star (γ) to vary. We rescaled the error bars of the FORS2 measurements by a factor of 4.3, in order to obtain a reduced

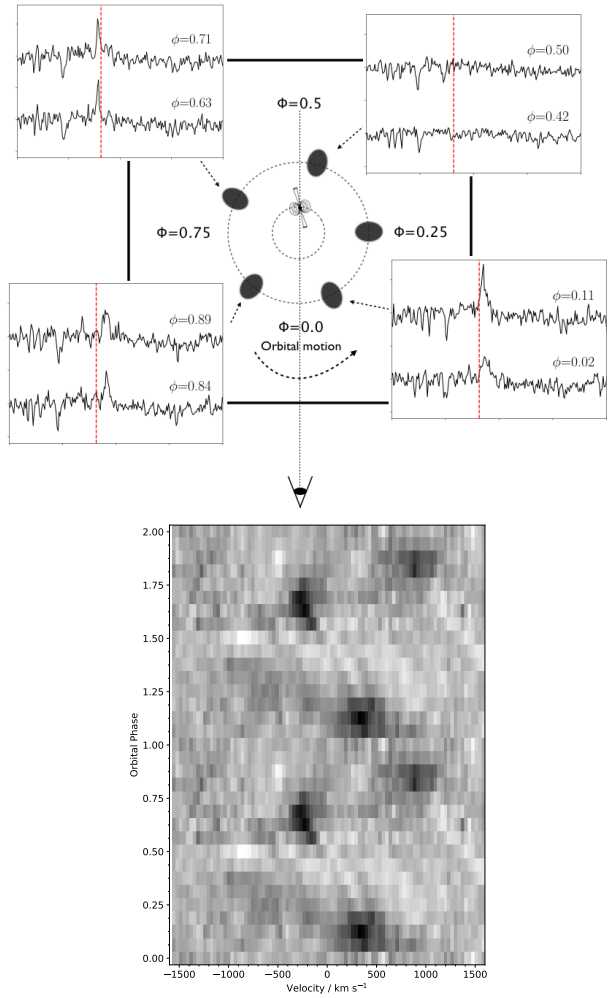

Figure 4.3: Top: A schematic panel of PSR J1048+2339 showing the orbital motion of the companion with Hα variability. The vertical red dashed line represents the Hα λ6561 rest wavelength. Bottom: trailed spectrum showing the orbital evolution of the Hα emission line. The spectra have been normalized to the continuum. Two cycles are shown for clarity.

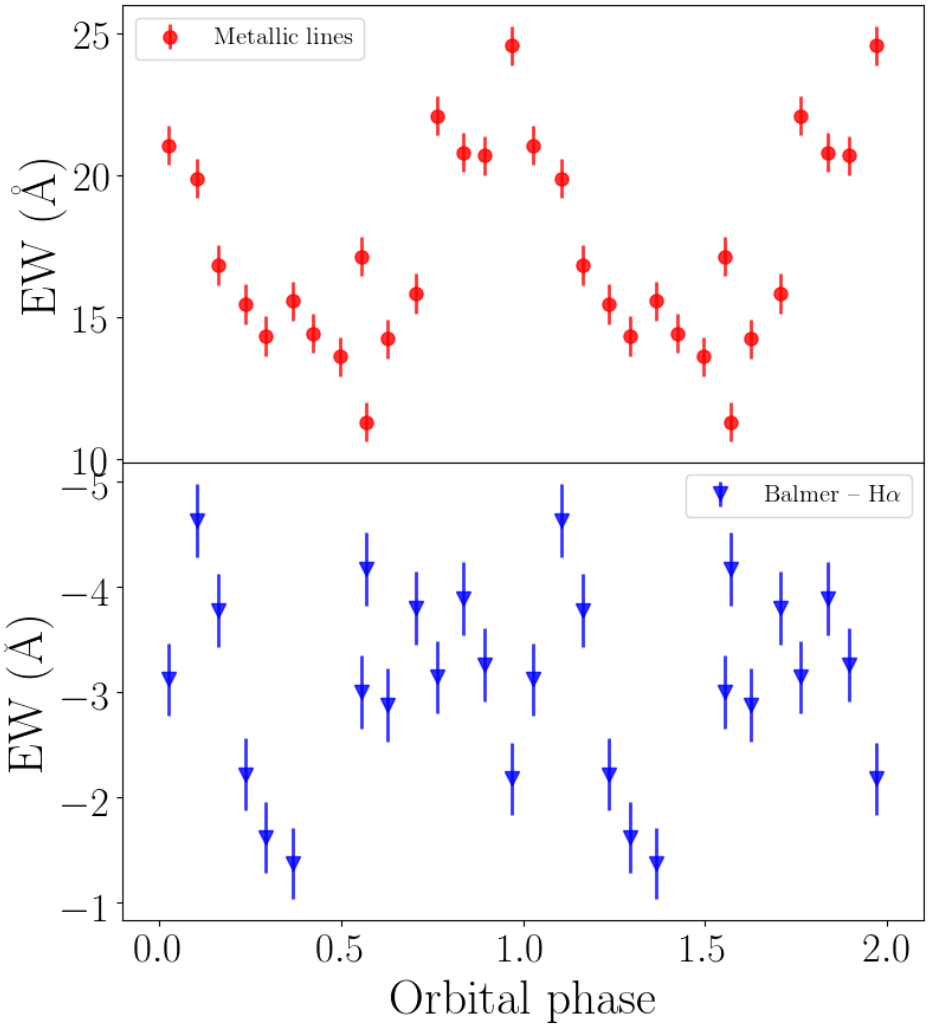

Figure 4.4: Equivalent width of metallic (red dots) and Hα (blue triangles) absorption and emission lines, respectively, as a function of the orbital phase. Two cycles are shown for clarity.

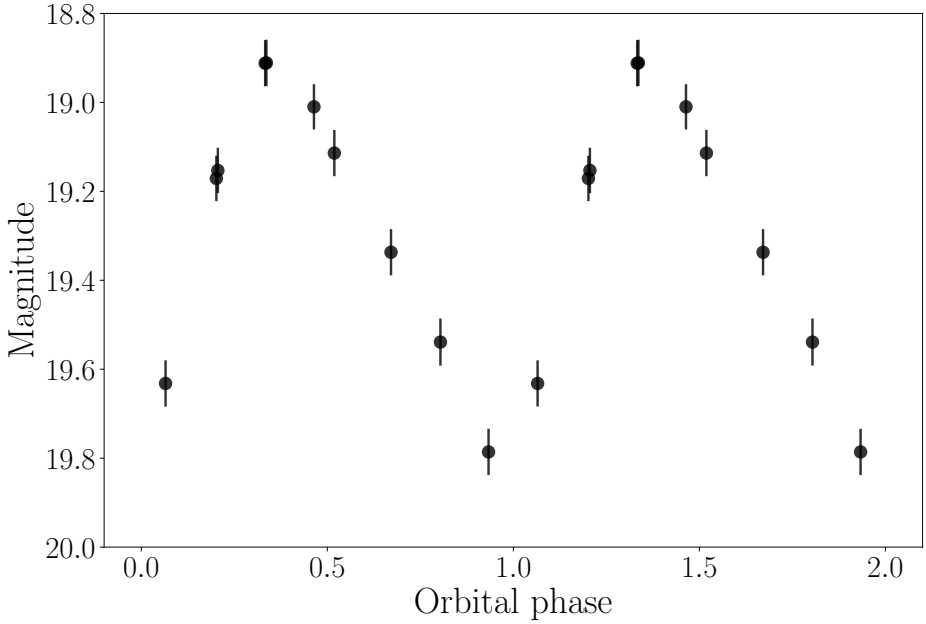

Figure 4.5: Phase-folded R-band light curve of PSR J1048+2339 companion star. The light curve shows a sinusoidal-like modulation with a peak-to-peak amplitude of $\sim$0.9 mag. The minimum is around phase zero as expected, while the maximum slightly precedes phase 0.5. Two cycles are shown for clarity.

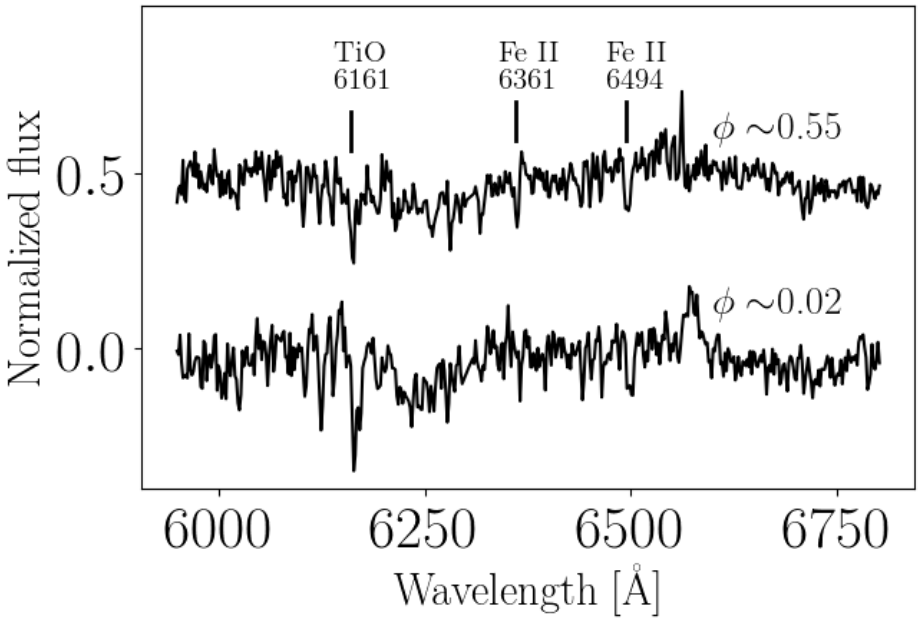

Figure 4.6: Main metallic absorption lines as observed at the inferior conjunction ($\phi \sim 0.02$) and at the superior conjunction ($\phi \sim 0.55$).

Table 4.3: Radial velocity parameters of PSR J1048+2339 with estimates of $1\sigma/68\%$ uncertainties. We rescaled the error bars of the VLT measurements by a factor of 4.3 to obtain a reduced χ^2=1.

Template star	Spectral Type	γ (km s^{-1})	K_2 (km s^{-1})	χ^2/d.o.f	d.o.f
HD 184467	K2 V	-14.4±3.7	339.9±5.4	1.0	13
HD 29697	K3 V	-17.8±3.2	341.0±4.5	1.2	13
HD 154712A	K4 V	-10.2±3.3	341.3±4.7	1.4	13
61 Cyg A	K5 V	-17.9±3.1	341.2±4.4	1.4	13
61 Cyg B	K7 V	-17.2±3.1	342.3±4.4	1.3	13
HD 154712B	K8 V	-10.5±3.1	343.3±4.4	1.0	13

$\chi^2 = 1$. The best match was obtained for the K2 V and K8 V templates, with equal significance (see Table 4.3).

We employed two independent approaches to classify the spectral type of the companion star. In the first one, we compared the ratio of the EW of the absorption lines in J1048 with different stellar templates. We considered the ratios λ6361(FeII)/λ6161 (TiO) and λ6494(FeII)/λ6161 (TiO). Using this criterion, the most likely spectral types are K7 V-K8 V (see Table 4.4).

In an alternative approach, we subtracted different templates appropriately degraded from the target average spectrum. We broadened stellar templates from 10 to 200 km s^{-1}, in steps of 10 km s^{-1} and subtracted the resultant broadened spectra from the J1048 Doppler-corrected average spectrum in the spectral range 6432-6477 Å, using a limb darkening coefficient μ=0.5. This subtraction method allows us to estimate the companion star rotational broadening $V \sin i$. In the optimal subtraction, the stellar template is scaled by a factor

Table 4.4: Line ratios for PSR J1048+2339 and template stars.

Template star	Spectral Type	6361(Fe II)/ 6161(TiO)	6494(Fe II)/ 6161(TiO)
PSR J1048		0.22±0.01	0.34±0.01
HD 184467	K2 V	0.36±0.01	0.56±0.01
HD 29697	K3 V	0.27±0.01	0.52±0.01
HD 154712A	K4 V	0.40±0.01	0.57±0.01
61 Cyg A	K5 V	0.27±0.01	0.45±0.01
61 Cyg B	K7 V	0.30±0.01	0.33±0.01
HD 154712B	K8 V	0.26±0.01	0.36±0.01

$0 \leqslant f_{frac} \leqslant 1$, which represents the fraction of flux from the companion star. We used this quantitative approach to match the observed absorption lines from J1048 to set of templates used before. The best fit was obtained for the template K8 V with a star contribution of $f_{frac} = 0.56\pm0.02$ and a projected rotational velocity for the companion of $v \sin i = 105\pm15\,\mathrm{km\,s^{-1}}$ (see Table 4.5). We verified that this result is not significantly affected by the variation of the limb darkening μ in the range $[0.0, 0.8]$.

Based on the results of these three analyses, we concluded that the most likely spectral type for J1048 is a K8 V star ($T_{eff} \sim 4000\,\mathrm{K}$). This determination is consistent with what was found by Yap et al. [2019] and has an uncertain of a couple of sub-spectral types. We found $K_{2,\mathrm{obs}}$=343.3±4.4 km s^{-1} and γ=-10.5±3.1 km s^{-1} (see Table 4.3 and Fig. 4.7). However, our constraint on $K_{2,\mathrm{obs}}$ does not seem to depend on the fine determination of the spectral type.

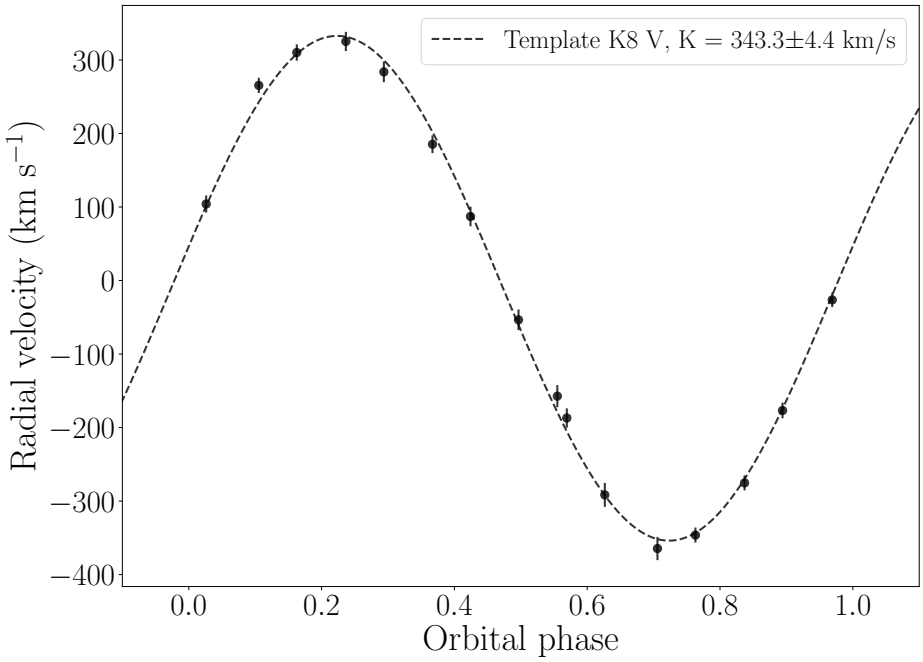

Figure 4.7: Radial velocities of the companion star in PSR J1048+2339 computed using a K8 V template and folded on the ephemeris derived using SRT. The best-fitting sinusoidal radial velocity curve is superposed.

Table 4.5: PSR J1048+2339 spectral classification by direct fitting using the limb darkening coefficient μ=0.5 and the rotational broadening $V \sin i = 105 \pm 15\,\mathrm{km\,s^{-1}}$.

Template star	Spectral Type	f_{frac}	χ^2/d.o.f (59 d.o.f.)
HD 184467	K2 V	1.06±0.06	3.2
HD 29697	K3 V	0.64±0.02	2.9
HD 154712A	K4 V	0.75±0.02	2.4
61 Cyg A	K5 V	0.67±0.02	2.6
61 Cyg B	K7 V	0.60±0.02	2.9
HD 154712B	K8 V	0.56±0.02	2.3

4.4.1 System parameters

Our determination of the mass ratio q and the NS mass relies on the determination of K_2 obtained by the measurement of the Doppler shifts of the absorption lines along the orbital period. This measurement is affected by a systematic error due to the pulsar irradiation, which determines a non-uniform absorption distribution on the stellar surface. The absorption lines formed on the companion photosphere are partially quenched in its irradiated face so that the center of light of these lines is shifted towards the outer face of the companion, causing a systematic shift in the velocity determined at each binary phase. Consequently, the radial velocity curve is not exactly sinusoidal and the K_2 obtained by fitting a sine curve is different from the true dynamical value. In our case, considering only absorption lines in the cross-correlation with stellar templates, the observed K_2 can be overestimated.

As shown in Wade and Horne [1988], we corrected the velocity using the so-called K-correction. The corrected observed radial velocity semiamplitude is:

$$K_{2,\mathrm{corr}}(q) = K_{2,\mathrm{obs}} - \Delta K(q) = K_{2,\mathrm{obs}} - f_K(q)\, V \sin i. \qquad (4.1)$$

Here, f_K is a geometrical correction factor smaller than unity ($0 < f_K < 1$). $f_K = 0$ indicates uniform emission over the donor star and thus no K-correction. If the non-irradiated hemisphere has a uniform absorption line strength and the other hemisphere does not contribute to the observed stellar absorption lines at all, $f_K = 4/3\pi \approx 0.42$ [Wade and Horne, 1988]. Hence, applying the K-correction (Equation 4.1), we get $K_{2,\mathrm{corr}}$=298.7±7.7 km s^{-1}. This is an unrealistic assumption in the case of J1048 that leads to obtain a firm lower limit of K_2, because both hemispheres contribute to the observed absorption lines (see Fig. 4.6). On the other hand, the measured value of $K_2 = 343.3 \pm 4.4$ km s^{-1}, without K-correction, is an upper limit.

Using the NS mass function from Deneva et al. [2016], we derived the semi-amplitude of the pulsar projected radial velocity $K_1 = (2\pi\, c\, x_p)/P_b$=72.7396±0.0003 km s^{-1}, where x_p is the projected semi-major axis of the pulsar orbit and P_b is the orbital period. By combining K_1 and K_2 ($291 < K_2 < 348$ km s^{-1}, at 1σ c.l.), we found a mass ratio $q = M_2/M_{NS} = K_1/K_{2,\mathrm{corr}}$ of $0.209 < q < 0.250$. This implies that the NS mass M_{NS}=$P_b\, K_2^3\, (1+q)^2/(2\pi\, G \sin^3 i)$ is $(1.0 < M_{\mathrm{NS}} < 1.6) \sin^{-3} i\, M_\odot$. Fixing the inclination to the upper limit of 76° due to the absence of X-ray eclipses [Yap et al., 2019], we constrained the NS mass to the range of $1.08 < M_{\mathrm{NS}} < 1.76\, M_\odot$ and the mass of the companion $M_2 = (K_1\, M_{\mathrm{NS}})/K_2$ to the range of $0.27 < M_2 < 0.37\, M_\odot$. We favour values of M_{NS} closer to the more massive scenario, because the irradiation seems to weakly affect the K_2 measurement. On the other hand, assuming the NS mass upper limit of $\sim 2.3\, M_\odot$ [Margalit and Metzger, 2017], we can derive a firm

lower limit inclination of 62° for a non-irradiated system ($f_K = 0$) and of 53° for a strongly irradiated system ($f_K = 4/3\,\pi$).

We note that the values of K_2, $M_{\rm NS}$ and M_2 obtained here are systematically lower than those obtained from Strader et al. [2019]. However, the data of Strader et al. [2019] are spread over four non-consecutive nights (whereas our data were collected over the same night) and they are not adjusted for the K-correction. Without the K-correction, we get an upper limit of $M_{\rm NS} \leqslant 1.76\,M_\odot$ (at 1σ c.l.), compatible within the errors with the value of Strader et al. [2019].

4.5 Hα Doppler tomography

We constructed a trailed spectrogram covering the 6250–6700 Å interval to compare the absorption and emission lines structures (see Fig. 4.8). The absorption features are visible throughout the orbital cycle and trace the companion star motion, while the Hα emission lines fade at some orbital phases (see Sect. 4.3). The derived Doppler image of the Hα emission line computed with the maximum entropy method [Marsh and Horne, 1988] is shown in velocity coordinates in Fig. 4.9. The Roche lobe of the companion and the gravitational free-fall path of the gas stream are superposed over the map. Fig. 4.9 shows the map constructed assuming an inclination $i \sim 76°$ and using the K_2 upper limit with $M_{\rm NS} < 1.76\,M_\odot$ and $q > 0.209$.

This image cannot be interpreted as a time-average map because the data were acquired over one night and the system displays strong variability on very short timescale (few days; Wang et al. 2013, Yap et al. 2019). Therefore, this Doppler map represents the 2D velocity distributions of the Hα emission on March 18–19, 2020.

The map does not show evidence of an accretion disc, but shows a relatively faint spot emission coincident in phase and velocity with the companion star. The S-wave profile component from the companion

is detected in the trailed spectra (see Fig. 4.3), although the emission is not continuous along the orbit. In addition, the Hα map reveals an extended bright spot in the upper left velocity quadrant close to the companion star, suggesting an intra-binary shock created from the interaction between the pulsar relativistic wind and matter leaving the companion star. The proximity of the intra-binary shock to the companion star indicates the presence of material in that region. If the secondary is filling its Roche-lobe the material streams away from L_1, otherwise the companion mass loss mechanism is driven by the ablation of the outer layers of the star by the energetic pulsar wind. Given the orbital separation and the mass ratio q, we can determine the approximate Roche-lobe radius R_L [Eggleton, 1983]. Assuming $i \sim 76^\circ$ we obtain $0.50\,R_\odot < R_L < 0.55\,R_\odot$, comparable to the radius of a K8 V star [Pasinetti Fracassini et al., 2001]. Yap et al. [2019] derived a Roche-lobe filling factor of 0.86 ± 0.02 during a phase of single-peaked optical light curve, casting doubts on whether the secondary is truly filling its Roche-lobe. Given the uncertainty in K_2 and in the dimension of the companion star irradiated by the pulsar wind, our analysis does not favor one mechanism for the mass loss over the other. There is no evidence for emission from an accretion disc, although its formation could take place on a very rapid timescale, as in IGR J18245–2452 [Papitto et al., 2013].

4.6 Radio timing analysis

The raw data taken in baseband mode with the SRT in the P band, and with the LOFAR in the VHF band, were first coherently dedispersed [Bassa et al., 2017] at J1048's nominal dispersion measure (DM) of 16.65 $\mathrm{pc\,cm^{-3}}$. The four Stokes parameters were summed to form total-intensity search-mode files. For the SRT P-band data, these retained a time resolution of 64 μs and 640, 125-KHz-wide frequency

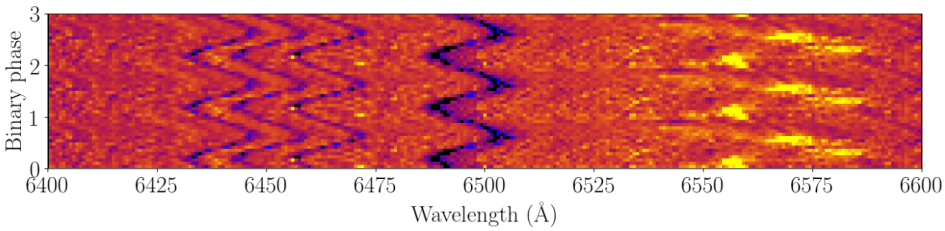

Figure 4.8: The trailed spectra averaged in 16 orbital phase bins revealing the orbital evolution of several absorption features and Hα emission lines. Three orbital phases are shown for clarify.

channels. For the LOFAR VHF-band data, the search-mode files kept a time resolution of 81.92 μs and 1600, 48-kHz-wide channels. As explained in Section 4.2.2, the SRT L-band data were already taken in search mode, so no prior manipulation was needed for them.

Once all the observations were available as search-mode files, we conducted the analysis as follows. For each observation, we first created a mask to filter out the strongest RFI present in the data, using the `rfifind` routine, part of the `PRESTO`[12] pulsar searching package [Ransom et al., 2002]. Taking the mask into account, we then used `PRESTO`'s `prepdata` to generate an RFI-free, frequency-summed dedispersed time series. These were folded using `PRESTO`'s `prepfold` and the ephemeris published by Deneva et al. [2016]. However, it is well known that many RBs and BWs show a strong orbital variability [e.g. Shaifullah et al., 2016, Bak Nielsen et al., 2020, Hebbar et al., 2020], often causing an old ephemeris not to be able to predict the actual orbital phase at a future time. This results in a wrong correction for the orbital Rømer delay [Blandford and Teukolsky, 1976] and, consequently, the pulsed emission can be missed when folding. Following Ridolfi et al. [2016], we overcame this issue by doing a brute-force search in

[12] `https://www.cv.nrao.edu/~sransom/presto`

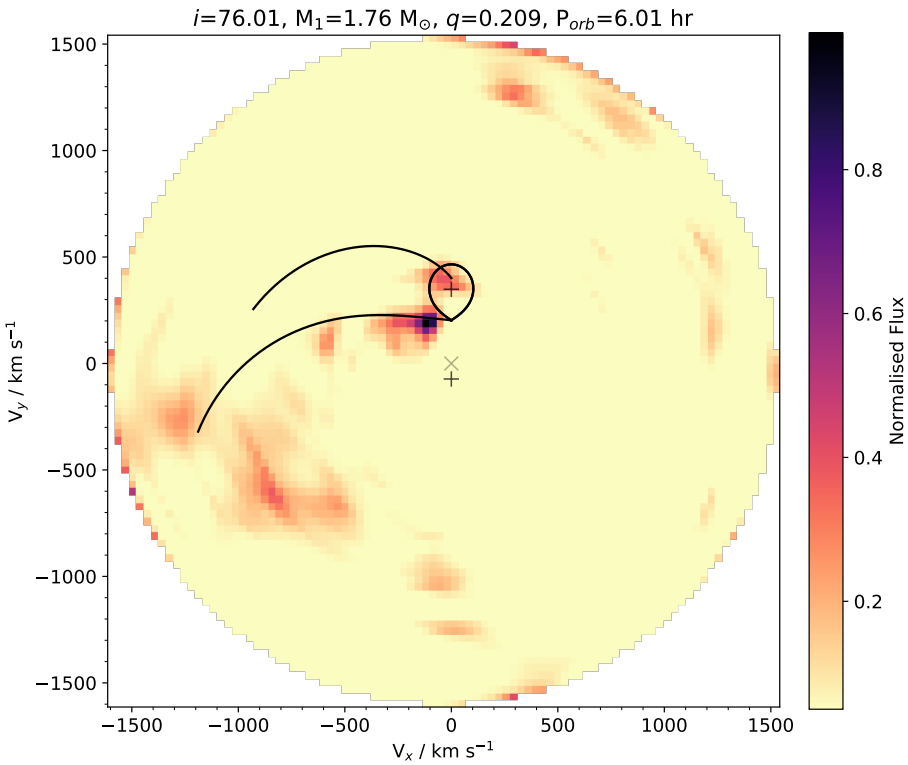

Figure 4.9: Doppler map of the Hα emission lines. We plot the gravitational free-fall gas stream trajectory (lower curve), the Keplerian disc velocity along the stream (upper curve) and the Roche lobe of the donor star using K_1=72.7639 km s^{-1} [Deneva et al., 2016], $i = 76°$ [Strader et al., 2019, Yap et al., 2019], $M_{\rm NS} = 1.76\,M_\odot$ and $q = 0.209$. The plus signs represent, from top to bottom, the companion and the NS, while the '$\times$' sign represents the center of mass. The map was computed for a systemic velocity $\gamma = -10.5$ km s^{-1}.

the time of the ascending node, $T_{\rm asc}$, using `SPIDER_TWISTER`[13] and a step size of $dT_{\rm asc} = 4.655$ s. We obtained a clear detection of J1048 in the L-band observation taken in August 2019 when using a $T_{\rm asc}$ MJD value of 58721.666409(54). This is ~ 28 s later than the $T_{\rm asc}$ value that can be extrapolated from the Deneva et al. [2016] ephemeris. Folding P band data taken simultaneously with the same parameters, however, resulted in a non-detection.

The simultaneous SRT+LOFAR observations of J1048 taken in March 2020 were analyzed in the same way. The only difference was that, given the very long duration of these observations (which covered one full orbit), we also splitted them into 1-hr-long chunks and searched for J1048's pulsations separately in each of them. Still, we were unable to detect J1048 in any of the three radio bands.

The non-detection in the L-band observation of March 2020 can likely be ascribed to interstellar scintillation, which is typically affecting pulsars with very low DMs (such as J1048). This effect randomly enhances or suppresses the observed flux density of the pulsar, with a dependence on the observing frequency. The confirmation that scintillation is indeed important for J1048 is given by the detection of the August 2019 L-band observation (Fig. 4.10): we can see that the J1048's pulsed signal is boosted only in a very narrow band around ~ 1.4 GHz, whereas it is barely detectable in the rest of the band. In addition to scintillation, another mechanism responsible for the non-detection in the P and VHF bands, can be the absorption due to the intra-binary eclipsing material. Partial or total eclipses seen in many BW and RB systems [Rasio et al., 1989a] can be ascribed to the frequency-dependent optical depth of the eclipsing material. The dense layers of ionised material ablated from the donor star are less transparent at low frequencies, determining eclipses in the P and VHF bands [e.g. Polzin et al., 2018]. As a side effect, at low frequencies,

[13] `https://github.com/alex88ridolfi/SPIDER_TWISTER`

the scattering [e.g. Lorimer and Kramer, 2004] can smear the individual pulses, making them broader than the pulsar spin period, but not preventing their detection.

From the non-detections, we can calculate an upper limit on the mean flux density, $S^{\rm mean}$, that J1048 must have had at the time of the observations. To do so, we use the modified radiometer equation [Manchester et al., 1996, Lorimer and Kramer, 2004]

$$S^{\rm mean} = \beta \frac{({\rm S/N})\, T_{\rm sys}}{G\sqrt{n_p t_{\rm int} \Delta\nu}} \sqrt{\frac{\delta}{1-\delta}}\,, \tag{4.2}$$

where $\beta \gtrsim 1$ is a correction factor due to digitization; n_p is the number of polarizations summed; S/N is the pulse signal-to-noise ratio; $T_{\rm sys}$ is the system noise temperature; G is the telescope gain; $t_{\rm int}$ is the integration time; $\Delta\nu$ is the bandwidth; δ is the pulse duty cycle. Table 4.6 lists the values of each parameter for all the radio observations that we used in the $S^{\rm mean}$ estimations. For the August 2019 P band non-detection we estimate $S^{\rm mean}_{\rm P} \lesssim 0.57\,$mJy, whereas in the case of the March 2020 non-detections we find $S^{\rm mean}_{\rm L} \lesssim 0.05\,$mJy, $S^{\rm mean}_{\rm P} < 0.24\,$mJy and $S^{\rm mean}_{\rm VHF} \lesssim 9.21\,$mJy for the P, L and VHF observations, respectively. For the only radio detection available to us (August 2019 L-band observation) we measure $S^{\rm mean}_{\rm L} \sim 1.22\,$mJy.

4.7 Optical timing analysis

We tested the acquired data with IFI+Iqueye for pulsations folding all three observations together with the spin period of the pulsar (0.00466516294153(3) s, extrapolated from Deneva et al. 2016 at MJD 58927.0) and 10 phase bins. The time of passage at the ascending node was fixed at $T_{\rm asc} = 58721.666409\,$MJD (see Sect. 4.6). A χ^2 test with a constant term corresponding to the average count rate was applied

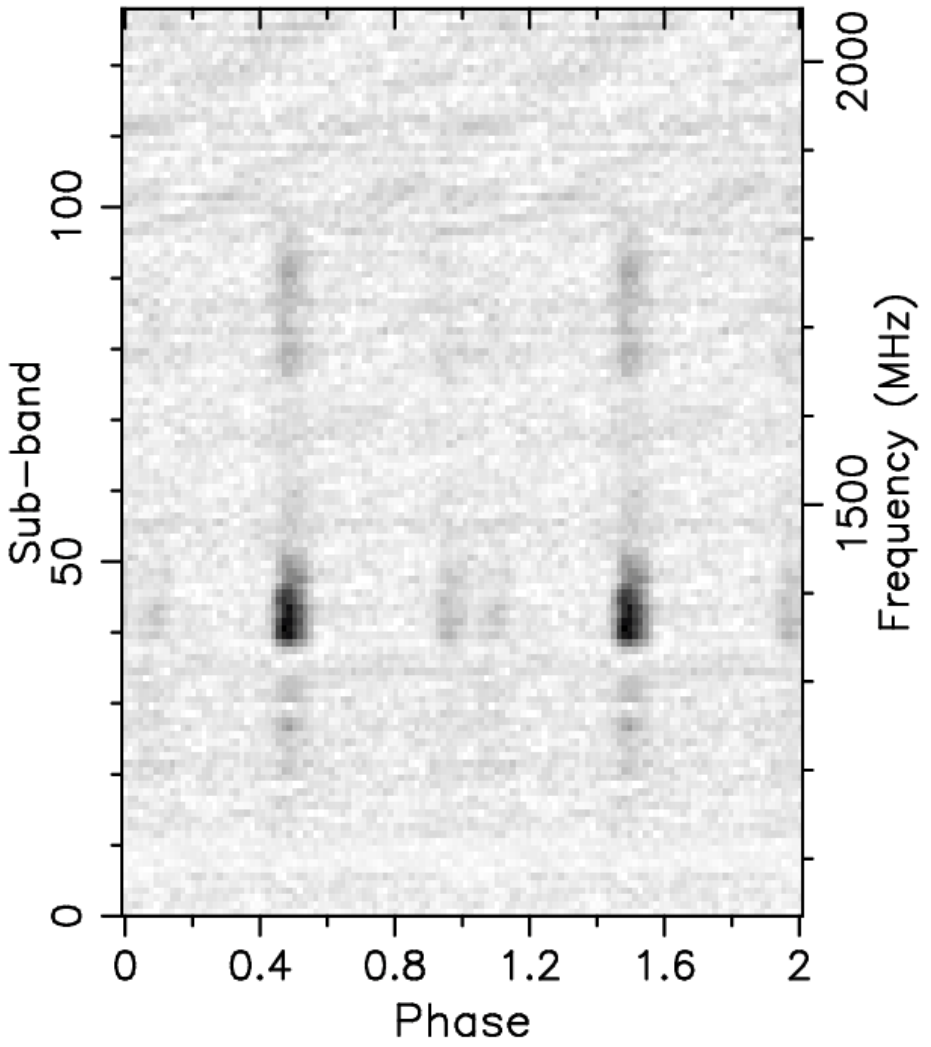

Figure 4.10: Intensity as a function of pulse phase (x-axis) and frequency (y-axis) for the SRT observation performed in the L band on 19 August, 2019. Signal strength is not constant at all frequencies. At ∼1.4 GHz there is a peak of intensity, while below 1.3 GHz and over 1.8 GHz the pulsed signal is almost absent.

Table 4.6: PSR J1048+2339 flux density at 0.1-0.2 GHz, 0.3-0.4 GHz and 1.3-1.8 GHz.

Band	$T_{\rm sys}$ [K]	Gain [K Jy^{-1}]	$\Delta\nu$ [MHz]	$t_{\rm int}$ [s]	n_p	β	$S^{\rm mean}$ [mJy]
L (August 2019)	30[a]	0.55[a]	281	5400	2	1	1.2
P (August 2019)	65[a]	0.52[a]	60	5400	2	1	<0.57
L (March 2020)	30[a]	0.55[a]	400	29960	2	1	<0.05
P (March 2020)	65[a]	0.52[a]	60	29960	2	1	<0.24
0.1-0.2 GHz (March 2020)	892[b]	0.18[c]	76	25200	2	1	<9.2

[a] `https://srt-documentation.readthedocs.io/en/latest/antenna.html#lp-band-filters`
[b] Lawson et al. [1987]
[c] van Haarlem et al. [2013]

to the folded profile. The χ^2 returns a value of 11.5 for 9 degrees of freedom, corresponding to a false positive probability of 24% and a significance of pulsed emission of only 1.2σ. Different choices for the number of phase bins provide similar results.

A conservative upper limit to the optical pulsed emission is derived from the power spectra of the three observations. The maximum excess power in the 0.5-500 Hz frequency range with a time bin of 1 ms corresponds to a root mean square fractional variability of $\sim 0.1\%$ or $\sim 2\,{\rm counts\,s^{-1}}$ for the observed average count rate. For IFI+Iqueye, this translates into a upper limit to any pulsed emission component of ~ 21 mag in the V band.

We performed also an epoch folding search varying the value of $T_{\rm asc}$ for our epoch in an interval between -250 s and +250 s around the value reported above and in steps of 1 s, and folding the event lists with 16 bins per period. No significant signal is detected. The maximum of the χ^2 is ~ 42 for 15 degrees of freedom, corresponding

to a significance of only 1.6σ (for 501 trials).

4.8 Discussion and conclusions

The multi-wavelength observations acquired in March 2020 confirmed the extreme emission variability of J1048 detected by Deneva et al. [2016], Cho et al. [2018], Strader et al. [2019] and Yap et al. [2019]. We observed rapid and strong emission changes in the Hα emission line along the orbit (Fig. 4.2). Using the optical photometry we revealed an average $R \sim$19.3 mag counterpart with orbital variability typical of moderate irradiated systems (Fig. 4.5). The shape of the R-band light curve showed that the modulation was dominated by the pulsar heating and not by ellipsoidal variations. We measured with radio timing analysis a strong orbital variation as in other RB systems [Jaodand et al., 2016a, Ridolfi et al., 2016]; the $T_{\rm asc}$ lagged the predicted value of Deneva et al. [2016] ephemeris by $\sim$28 s.

We measured the radial velocity curve through the cross-correlation with late-type template stars and we set the following constraints to the mass ratio, to the mass of the NS and of the companion star: $0.209 < q < 0.250$, $(1.0 < M_{\rm NS} < 1.6)\sin^{-3}i\,M_{\odot}$ and $(0.24 < M_2 < 0.33)\sin^{-3}i\,M_{\odot}$. Assuming the inclination upper limit of 76° [Yap et al., 2019], we derived a NS mass of $1.08 < M_{\rm NS} < 1.76\,M_{\odot}$. Given the uncertainty on the inclination, we cannot exclude the presence of a high-mass NS. Assuming the NS mass upper limit of $\sim 2.3\,M_{\odot}$, the inclination of J1048 must be $> 62°$ if the system is non-irradiated, and $> 53°$ if it is strongly irradiated. We constrained the spectral type of the donor to a K8 V star ($\sim$4000 K). The companion star contributes 56% to the total light observed at 6400Å, suggesting the presence of an additional diluting source such as an intra-binary shock.

We presented the first Hα Doppler tomography of a RB system in a rotation-powered, radio pulsar state. Doppler tomograms of RBs were

only performed for the two transitional systems PSR J1023+0038 and XSS J12270-4859, but during the disc state [Hakala and Kajava, 2018, de Martino et al., 2014]. The reconstructed Hα Doppler map revealed a significant emission close to the inner Lagrangian point along the gravitational free-fall trajectory of the gas and at the companion star surface (see Fig. 4.9). The extended structure seen in the Hα line is a first and clear evidence of an intra-binary shock emission caused by the interaction of the pulsar wind with material lost from the companion star. Such shocks have been earlier proposed to be responsible for the X-ray orbital variability in MSP binaries [Bogdanov et al., 2005] and their presence has been indirectly confirmed by several observations in different domains [Wadiasingh et al., 2018]. Our detection of a localised emission of Hα line makes J1048 the first RB showing direct evidence of an intra-binary shock emitting at other wavelengths. Whether the secondary star is overflowing its Roche lobe, the observed emission could be produced by the interaction of the gas streaming the L_1 and the pulsar wind. Due to the lack of strong constraints on Roche-lobe filling factor (see Yap et al. 2019), the shock emission could also be due to the interaction of ablated material from the companion and the strong pulsar wind. In this last configuration, and given that the Hα emission comes close to L_1, this could be a signature of matter from the intra-binary shock that are ducted to the companion surface along the magnetic field of the companion star as hypothesized by Sanchez and Romani [2017]. The fact that this system shows variability on different epochs may be compatible with this scenario.

The presence of the intra-binary shock emission can explain the prolonged radio eclipses [Deneva et al., 2016, 2020] and the sporadic appearance of Hα double-peaked emission lines [Strader et al., 2019] observed in J1048. This map confirms the hypothesised scenario in which RBs are characterized by a large amount of material being stripped off the companion star due to the pulsar ablation process [Breton et al., 2013]. The intra-binary shock in J1048 appears to be

closer to the companion than to the pulsar. This evidence contrasts with the recently proposed scenario for the X-ray shock emission in RB systems [Wadiasingh et al., 2018, van der Merwe et al., 2020] in which the intra-binary shock is assumed to be closer to the pulsar. This assumption is supported by the large radio eclipse fractions observed in RBs at pulsar superior conjunction [Archibald et al., 2009, Roy et al., 2015, Deneva et al., 2016], as well as the double-peaked X-ray orbital modulation centered at the pulsar inferior conjunction [Romani and Sanchez, 2016, Al Noori et al., 2018, de Martino et al., 2020]. However, the Doppler map of J1048 suggests that X-ray and Hα emissions do not trace the same region of the intra-binary shock material. Hα emission may trace a portion of intra-binary shock closer to the companion while the X-rays could originate closer to the NS.

The absence of the pulsed radio signal in March 2020 observations cannot be ascribed to a state transition such as the one observed in the tMSPs [Archibald et al., 2009, Papitto et al., 2013], but rather to scintillation and/or absorption phenomena [Gedalin and Eichler, 1993, Thompson et al., 1994, Roy et al., 2015]. At very low frequency (0.1-0.2 GHz) the radio signal could be totally eclipsed by absorption due to the presence of a low-density highly-ionized gas cloud spilling off the companion [Broderick et al., 2016]. Indeed, no increase in the X-ray and optical fluxes were observed and the Hα Doppler map clearly showed the presence of an intra-binary shock and not an accretion disc. The presence of an extended shock front could lead in the near future to the formation of an accretion disc, but as we have observed in the three tMSPs discovered so far, the state transition is not predictable and takes place in a very rapid (few weeks) timescale [Archibald et al., 2009, Papitto et al., 2013, Bassa et al., 2014].

Although J1048 is one of only a handful of RBs that occasionally displays emission lines in their optical spectra, similar behaviour is observed in other RBs and BWs, such as 3FGL J0838.8–2829 [Halpern et al., 2017b,a], PSR J1628–3205 [Cho et al., 2018, Strader et al., 2019],

and PSR J1311–3430 [Romanova and Owocki, 2015]. Further spectroscopic observations of these RBs and BWs therefore seem warranted. It would be interesting to monitor these systems for several contiguous orbital phases to study the evolution of the Doppler map and confirm the rapid variability of the gas distribution.

5

Conclusions and future prospects

In this thesis I presented the results of my work as PhD candidate at the Insubria University in collaboration with the INAF-Osservatorio Astronomico di Brera, encompassing multi-wavelength studies of a diverse ensemble of binary millisecond pulsars (MSPs). Different data-analysis techniques were employed and optimized depending on the evolutionary state and the physical properties of the systems under study.

The leading purpose of this thesis was addressing open questions concerning which processes are responsible for the multi-wavelength pulsed emission in binary MSPs and in which conditions they operate. In order to properly face this problem, I employed timing analysis techniques in different electromagnetic domains, from X-ray to UV/optical and radio bands to study these objects in all their evolutionary phases, from the accretion state to the quiescent radio pulsar state.
The rapid variability between low/high and flares modes (see Chapter 1) during the sub-luminous disc state in transitional millisecond pulsars (tMSPs) is another focus of this thesis. To investigate these phenomena, I made use of X-ray spectral analysis techniques, applying it to the study of the tMSPs XSS J12270–4859 and PSR J1023+0038. The presence of an accretion disc and a possible intra-binary shock emission in redback (RB) and accreting millisecond X-ray pulsar (AMXP)

systems during their radio pulsar or quiescence state has also been investigated in this work, given its profound implications for the study of the evolution of these objects. This part of my work has involved the optical spectroscopic analysis and the Doppler tomography technique, which I used to reconstruct the geometry and kinematics of the gas in a RB system.

The first important result we obtained is the discovery of a new phenomenology in AMXPs. Timing studies of MSPs are usually based on radio or X-ray data and rarely include observations in the UV/optical band. This is the case for AMXPs, which until recently were believed to emit only X-ray pulsations in their outburst phase. Conducting an innovative observational campaign with the STIS/HST and SiFAP2/TNG instruments, we investigated the existence of pulsations in the UV/optical band in the AMXP SAX J1808.4–3658 during its 2019 outburst phase (see Chapter 2). Pulsations were detected simultaneously in optical, UV and X-ray bands while the pulsar was surrounded by an accretion disc. The optical and the X-ray pulsations from SAX J1808.4–3658 are shifted by half a rotational cycle, i.e. they are almost in anti-phase. This is an evidence that X-ray and optical/UV pulses are likely to be generated by different mechanisms occurring in different locations. We have interpreted this as a sign that, at least during the outburst, the rotation-powered mechanism and the accretion-powered mechanism can co-exist or alternate very rapidly. Such a discovery now challenges the paradigm that MSPs in the accretion state can be detected only as accretion-powered X-ray pulsars, and opens new prospects to understand the complex phenomenology of AMXPs and tMSPs in general.
In order to strengthen our understanding of the physical origin of multi-band pulsed emission in binary MSPs, we need to monitor several sources in different evolutionary states, from the low-mass X-ray binary state to the radio pulsar state. One approved dedicated obser-

vational project led by me have the purpose of studying the physical processes that produces the pulsed X-ray/UV/optical emissions in unison. This future project is a Target of Opportunity observing program with *XMM-Newton* telescope, HST and TNG aiming at searching for UV/optical pulsations at the pulsar spin period in the first known accreting millisecond X-ray pulsars showing a new outburst. About 19 AMXPs have been discovered over the past 21 years, all showing recurrent outburst phases with different intensities and durations. This provides an optimal sample, significantly wider than that of tMSPs, of candidates for the systematic search for pulsations in the X-rays, UV and optical bands during the outburst phase and possibly during quiescence. We also plan to re-observe SAX J1808.4–3658 in the optical band during its quiescence state, a regime in which X-ray and radio pulsations have remained so far undetected. Given the faintness of AMXPs in quiescence at X-ray energies, this is the only opportunity we have to detect any pulsation during the quiescent state.

One of the most enigmatic behaviour of recently discovered tMSPs is the rapid swing between modes of different luminosity during the sub-luminous disc state. We investigated the mechanism that triggers this swing and the possible co-existence of rotation and accretion powered regimes in the sub-luminous state of two tMSPs.
We discussed in detail two spectral models motivated by different physical scenarios in order to explain the rapid variability between high, low and flare modes (see Chapter 3). The first physical scenario was proposed before optical pulsations were discovered in PSR J1023+0038, while the second one accounts for this new phenomenology. The transition between the observed high and low modes in the first model is explained as a fast transition between the 'propeller' state and the radio-ejection pulsar state. In the propeller regime (i.e. the high mode) the presence of a centrifugal barrier inhibits accretion, preventing matter from falling on the NS surface. As shown by magne-

tohydrodynamic simulations, some matter can however leak through the centrifugal barrier and can accrete onto the NS. Instead, during the radio-ejection phase (i.e. the low mode), the mass-accretion stops definitely. The second physical model, driven by the new optical observations, involves an active radio pulsar during the sub-luminous disc state, and the source of power for the pulsations is its rotational energy. X-ray and optical pulsations are produced by synchrotron emission in the intrabinary shock. The position of the termination shock is variable, in the low luminosity mode the shock's radius expands, causing the disappearance of X-ray and optical pulses. Both models provide good fit to the data but we stress that the latter can also explain the new phenomenology of optical pulsations observed in PSR J1023+0038.

The two tMSPs PSR J1023+0038 and XSS J12270–4859 share a very similar phenomenology, however XSS J12270–4859 shows two different low-modes (low-soft and low-hard) distinguishable for their spectral shape. Basing on an accurate spectral analysis that allowed us to compare the different spectral shapes during the soft and hard low modes, we found that the harder component is simply correlated with the tail of the flare emission.

During the ongoing rotation-powered, radio pulsar state, into which the tMSP XSS J12270–4859 entered at the end of 2012/beginning 2013, the system has shown some uncommon features. The X-ray luminosity in the range 0.3–10 keV varied by a factor $\sim$1.6 between two *XMM-Newton* observations taken 6 months apart. Moreover, the X-ray long-term light curve shows a variability of $\sim$40% in the count rate and a sinusoidal modulation with periodicity of 387 ± 7 d. I have an approved program to monitor the X-ray and UV long-term flux variability using the *Swift*-XRT-UVOT satellite in order to confirm the existence of this periodicity and investigate the physical process responsible for it.

In the last part of this thesis, I employed multi-wavelength observations, acquired simultaneously with four telescopes (*Swift*/XRT-UVOT, VLT, Galileo, LOFAR and SRT) on March 2020, to study the RB PSR J1048+2339 (see Chapter 4). Optical spectra of PSR J1048+2339 acquired with the 4-m SOAR telescope and presented in literature show the most intense variability yet observed for any RBs. Strong emission lines were observed, which in some instances appear double-peaked and in others single-peaked. This phenomenology could be associated with a shock caused by the interaction between highly relativistic pulsar wind and the matter coming from the companion star. The multi-wavelength campaign we performed was aimed at confirming or excluding this hypothesis through the Doppler tomography technique. The Doppler tomography method allows us to derive two-dimensional velocity maps of emission lines. The Hα Doppler map that we obtained on PSR J1048+2339, revealed a significant emission from the companion star and close to the inner Lagrangian point L_1, extending along the ballistic trajectory of the gas stream. This structure provides the first direct evidence of an intra-binary shock emission caused by the pulsar wind interacting with the ablated material from the donor in a RB system. PSR J1048+2339 is one of the few RB systems that clearly shows optical emission lines during the radio pulsar state, which allowed us to successfully apply the Doppler tomography method, making this analysis the first of its kind. In the future we plan to apply this technique to investigate the rapid variability of gas distribution between contiguous orbits of other RB systems, possibly with simultaneous radio observations.

The results presented here are an important breakthrough in the knowledge of binary MSPs. These sources, in particular tMSPs, were discovered only recently, therefore much about their phenomenology is yet to be uncovered and explained. The new observational evidences here reported, in particular the discovery of optical/UV pulsations,

could lead to important developments of the current evolutionary scenario and eventually contribute to define a general picture for the mechanism powering the multi-wavelength emission of MSPs. The high sensitivity of optical and UV fast photometric observations may lead to the discovery of coherent pulsations in new sources and regimes for which the X-ray luminosity is too low to search for pulsations.
Multi-wavelength observational techniques, in particular temporal and spectral, can provide a wealth of important information to better understand the physics of these highly energetic sources. Future studies on AMXPs, tMSPs and eclipsing MSPs covering a wide frequency range will likely clarify what makes a system transitional or whether rotation and accretion powered mechanisms can coexist in some regimes. The study of interaction between pulsar magnetic field and in-flowing gas during different accretion regimes can reveal how isolated MSPs are formed.

Bibliography

Hind Al Noori, Mallory S. E. Roberts, Rodrigo A. Torres, Maura A. McLaughlin, Peter A. Gentile, Jason W. T. Hessels, Paul S. Ray, Matthew Kerr, and Rene P. Breton. X-Ray and Optical Studies of the Redback System PSR J2129-0429. *ApJ*, 861(2):89, July 2018. doi: 10.3847/1538-4357/aac828.

M. A. Alpar, A. F. Cheng, M. A. Ruderman, and J. Shaham. A new class of radio pulsars. *Nature*, 300(5894):728–730, December 1982. doi: 10.1038/300728a0.

F. Ambrosino, P. Cretaro, F. Meddi, C. Rossi, S. Sclavi, and I. Bruni. The Latest Version of SiFAP: Beyond Microsecond Time Scale Photometry of Variable Objects. *J. Astron. Instrum.*, 5(3):1650005-1267, September 2016. doi: 10.1142/S2251171716500057.

F. Ambrosino, A. Papitto, L. Stella, F. Meddi, P. Cretaro, L. Burderi, T. Di Salvo, G. L. Israel, A. Ghedina, L. Di Fabrizio, and L. Riverol. Optical pulsations from a transitional millisecond pulsar. *Nature Astron.*, 1:854–858, October 2017. doi: 10.1038/s41550-017-0266-2.

I. Appenzeller, K. Fricke, W. Fürtig, W. Gässler, R. Häfner, R. Harke, H. J. Hess, W. Hummel, P. Jürgens, R. P. Kudritzki, K. H. Mantel, W. Meisl, B. Muschielok, H. Nicklas, G. Rupprecht, W. Seifert, O. Stahl, T. Szeifert, and K. Tarantik. Successful commissioning of FORS1 - the first optical instrument on the VLT. *The Messenger*, 94:1–6, December 1998.

James H. Applegate and Jacob Shaham. Orbital Period Variability in the Eclipsing Pulsar Binary PSR B1957+20: Evidence for a Tidally Powered Star. *ApJ*, 436:312, November 1994. doi: 10.1086/174906.

Anne M. Archibald, Ingrid H. Stairs, Scott M. Ransom, Victoria M. Kaspi, Vladislav I. Kondratiev, Duncan R. Lorimer, Maura A.

McLaughlin, Jason Boyles, Jason W. T. Hessels, Ryan Lynch, Joeri van Leeuwen, Mallory S. E. Roberts, Frederick Jenet, David J. Champion, Rachel Rosen, Brad N. Barlow, Bart H. Dunlap, and Ronald A. Remillard. A Radio Pulsar/X-ray Binary Link. *Science*, 324(5933):1411, June 2009. doi: 10.1126/science.1172740.

Anne M. Archibald, Victoria M. Kaspi, Slavko Bogdanov, Jason W. T. Hessels, Ingrid H. Stairs, Scott M. Ransom, and Maura A. McLaughlin. X-ray Variability and Evidence for Pulsations from the Unique Radio Pulsar/X-ray Binary Transition Object FIRST J102347.6+003841. *ApJ*, 722(1):88–95, October 2010. doi: 10.1088/0004-637X/722/1/88.

Anne M. Archibald, Victoria M. Kaspi, Jason W. T. Hessels, Ben Stappers, Gemma Janssen, and Andrew Lyne. Long-Term Radio Timing Observations of the Transition Millisecond Pulsar PSR1023+0038. *arXiv e-prints*, art. arXiv:1311.5161, November 2013.

Anne M. Archibald, Slavko Bogdanov, Alessandro Patruno, Jason W. T. Hessels, Adam T. Deller, Cees Bassa, Gemma H. Janssen, Vicky M. Kaspi, Andrew G. Lyne, Ben W. Stappers, Shriharsh P. Tendulkar, Caroline R. D'Angelo, and Rudy Wijnands. Accretion-powered Pulsations in an Apparently Quiescent Neutron Star Binary. *ApJ*, 807(1):62, July 2015. doi: 10.1088/0004-637X/807/1/62.

Jr. Arendt, Paul N. and Jean A. Eilek. Pair Creation in the Pulsar Magnetosphere. *ApJ*, 581(1):451–469, December 2002. doi: 10.1086/344133.

K. A. Arnaud. XSPEC: The First Ten Years. In George H. Jacoby and Jeannette Barnes, editors, *Astronomical Data Analysis Software and Systems V*, volume 101 of *Astronomical Society of the Pacific Conference Series*, page 17, January 1996.

J. Arons. Pair creation above pulsar polar caps : geometrical structure and energetics of slot gaps. *ApJ*, 266:215–241, March 1983. doi: 10.1086/160771.

Jonathan Arons and Marco Tavani. High-Energy Emission from the Eclipsing Millisecond Pulsar PSR 1957+20. *ApJ*, 403:249, January 1993. doi: 10.1086/172198.

W. Baade and F. Zwicky. On Super-novae. *Proceedings of the National Academy of Science*, 20(5):254–259, May 1934. doi: 10.1073/pnas.20.5.254.

D. C. Backer, S. R. Kulkarni, C. Heiles, M. M. Davis, and W. M. Goss. A millisecond pulsar. *Nature*, 300(5893):615–618, December 1982. doi: 10.1038/300615a0.

M. C. Baglio, P. D'Avanzo, S. Campana, F. Coti Zelati, S. Covino, and D. M. Russell. Different twins in the millisecond pulsar recycling scenario: Optical polarimetry of PSR J1023+0038 and XSS J12270-4859. *A&A*, 591:A101, June 2016. doi: 10.1051/0004-6361/201628383.

Arash Bahramian, Jay Strader, Laura Chomiuk, Craig O. Heinke, James C. A. Miller-Jones, Nathalie Degenaar, Alexandra J. Tetarenko, Vlad Tudor, Evangelia Tremou, Laura Shishkovsky, Rudy Wijnands, Thomas J. Maccarone, Gregory R. Sivakoff, and Scott Ransom. The MAVERIC Survey: A Transitional Millisecond Pulsar Candidate in Terzan 5. *ApJ*, 864(1):28, September 2018. doi: 10.3847/1538-4357/aad68b.

Arash Bahramian, Jay Strader, James C. A. Miller-Jones, Laura Chomiuk, Craig O. Heinke, Thomas J. Maccarone, David Pooley, Laura Shishkovsky, Vlad Tudor, Yue Zhao, Kwan Lok Li, Gregory R. Sivakoff, Evangelia Tremou, and Johannes Buchner. The

MAVERIC Survey: Chandra/ACIS Catalog of Faint X-Ray Sources in 38 Galactic Globular Clusters. *ApJ*, 901(1):57, September 2020. doi: 10.3847/1538-4357/aba51d.

Ann-Sofie Bak Nielsen, Gemma H. Janssen, Golam Shaifullah, Joris P. W. Verbiest, David J. Champion, Grégory Desvignes, Lucas Guillemot, Ramesh Karuppusamy, Michael Kramer, Andrew G. Lyne, Andrea Possenti, Ben W. Stappers, Cees Bassa, Ismaël Cognard, Kuo Liu, and Gilles Theureau. Timing stability of three black widow pulsars. *MNRAS*, 494(2):2591–2599, April 2020. doi: 10.1093/mnras/staa874.

M. M. Basko and R. A. Sunyaev. Radiative transfer in a strong magnetic field and accreting X-ray pulsars. *A&A*, 42(3):311–321, September 1975.

C. G. Bassa, A. Patruno, J. W. T. Hessels, E. F. Keane, B. Monard, E. K. Mahony, S. Bogdanov, S. Corbel, P. G. Edwards, A. M. Archibald, G. H. Janssen, B. W. Stappers, and S. Tendulkar. A state change in the low-mass X-ray binary XSS J12270-4859. *MNRAS*, 441(2):1825–1830, June 2014. doi: 10.1093/mnras/stu708.

C. G. Bassa, Z. Pleunis, and J. W. T. Hessels. Enabling pulsar and fast transient searches using coherent dedispersion. *Astronomy and Computing*, 18:40–46, January 2017. doi: 10.1016/j.ascom.2017.01.004.

Steve Bégin. A search for fast pulsars in globular clusters. Master's thesis, University of British Columbia, October 2006.

D. Bhattacharya and E. P. J. van den Heuvel. Formation and evolution of binary and millisecond radio pulsars. *Phys. Rep.*, 203(1-2):1–124, January 1991. doi: 10.1016/0370-1573(91)90064-S.

R. Blandford and S. A. Teukolsky. Arrival-time analysis for a pulsar in a binary system. *ApJ*, 205:580–591, April 1976. doi: 10.1086/154315.

Slavko Bogdanov. A NuSTAR Observation of the Gamma-ray-emitting X-ray Binary and Transitional Millisecond Pulsar Candidate 1RXS J154439.4-112820. *ApJ*, 826(1):28, July 2016. doi: 10.3847/0004-637X/826/1/28.

Slavko Bogdanov, Jonathan E. Grindlay, and Maureen van den Berg. An X-Ray Variable Millisecond Pulsar in the Globular Cluster 47 Tucanae: Closing the Link to Low-Mass X-Ray Binaries. *ApJ*, 630 (2):1029–1036, September 2005. doi: 10.1086/432249.

Slavko Bogdanov, Alessandro Patruno, Anne M. Archibald, Cees Bassa, Jason W. T. Hessels, Gemma H. Janssen, and Ben W. Stappers. X-Ray Observations of XSS J12270-4859 in a New Low State: A Transformation to a Disk-free Rotation-powered Pulsar Binary. *ApJ*, 789(1):40, July 2014. doi: 10.1088/0004-637X/789/1/40.

Slavko Bogdanov, Anne M. Archibald, Cees Bassa, Adam T. Deller, Jules P. Halpern, George Heald, Jason W. T. Hessels, Gemma H. Janssen, Andrew G. Lyne, Javier Moldón, Zsolt Paragi, Alessandro Patruno, Benetge B. P. Perera, Ben W. Stappers, Shriharsh P. Tendulkar, Caroline R. D'Angelo, and Rudy Wijnand s. Coordinated X-Ray, Ultraviolet, Optical, and Radio Observations of the PSR J1023+0038 System in a Low-mass X-Ray Binary State. *ApJ*, 806 (2):148, June 2015. doi: 10.1088/0004-637X/806/2/148.

Slavko Bogdanov, Adam T. Deller, James C. A. Miller-Jones, Anne M. Archibald, Jason W. T. Hessels, Amruta Jaodand, Alessandro Patruno, Cees Bassa, and Caroline D'Angelo. Simultaneous Chandra and VLA Observations of the Transitional Millisecond Pulsar PSR

J1023+0038: Anti-correlated X-Ray and Radio Variability. *ApJ*, 856(1):54, March 2018. doi: 10.3847/1538-4357/aaaeb9.

Howard E. Bond, Richard L. White, Robert H. Becker, and M. Sean O'Brien. FIRST J102347.6+003841: The First Radio-selected Cataclysmic Variable. *PASP*, 114(802):1359–1363, December 2002. doi: 10.1086/344381.

R. P. Breton, M. H. van Kerkwijk, M. S. E. Roberts, J. W. T. Hessels, F. Camilo, M. A. McLaughlin, S. M. Ransom, P. S. Ray, and I. H. Stairs. Discovery of the Optical Counterparts to Four Energetic Fermi Millisecond Pulsars. *ApJ*, 769(2):108, June 2013. doi: 10.1088/0004-637X/769/2/108.

J. W. Broderick, R. P. Fender, R. P. Breton, A. J. Stewart, A. Rowlinson, J. D. Swinbank, J. W. T. Hessels, T. D. Staley, A. J. van der Horst, M. E. Bell, D. Carbone, Y. Cendes, S. Corbel, J. Eislöffel, H. Falcke, J. M. Grießmeier, T. E. Hassall, P. Jonker, M. Kramer, M. Kuniyoshi, C. J. Law, S. Markoff, G. J. Molenaar, M. Pietka, L. H. A. Scheers, M. Serylak, B. W. Stappers, S. ter Veen, J. van Leeuwen, R. A. M. J. Wijers, R. Wijnands, M. W. Wise, and P. Zarka. Low-radio-frequency eclipses of the redback pulsar J2215+5135 observed in the image plane with LOFAR. *MNRAS*, 459(3):2681–2689, July 2016. doi: 10.1093/mnras/stw794.

R. Buccheri, K. Bennett, G. F. Bignami, J. B. G. M. Bloemen, V. Boriakoff, P. A. Caraveo, W. Hermsen, G. Kanbach, R. N. Manchester, J. L. Masnou, H. A. Mayer-Hasselwander, M. E. Özel, J. A. Paul, B. Sacco, L. Scarsi, and A. W. Strong. Search for pulsed γ-ray emission from radio pulsars in the COS-B data. *A&A*, 128:245–251, December 1983.

Peter Bult, Deepto Chakrabarty, Zaven Arzoumanian, Keith C. Gendreau, Sebastien Guillot, Christian Malacaria, Paul S. Ray, and

Tod E. Strohmayer. Timing the pulsations of the accreting millisecond pulsar SAX J1808.4-3658 during its 2019 outburst. *arXiv e-prints*, art. arXiv:1910.03062, October 2019.

G. R. Burbidge. Pulsed Radio Sources. *Nature*, 218(5140):433–434, May 1968. doi: 10.1038/218433a0.

L. Burderi, F. D'Antona, M. T. Menna, L. Stella, T. di Salvo, R. Iaria, N. R. Robba, A. Possenti, N. D'Amico, and M. Burgay. A radio pulsar phase in accreting X-ray binaries: limited mass transfer and spin-up of the neutron star. In Riccardo Giacconi, Salvatore Serio, and Luigi Stella, editors, *X-ray Astronomy 2000*, volume 234 of *Astronomical Society of the Pacific Conference Series*, page 237, January 2001.

L. Burderi, T. Di Salvo, M. T. Menna, A. Riggio, and A. Papitto. Order in the Chaos: Spin-up and Spin-down during the 2002 Outburst of SAX J1808.4-3658. *ApJ*, 653(2):L133–L136, December 2006. doi: 10.1086/510666.

M. Burgay, N. D'Amico, A. Possenti, R. N. Manchester, A. G. Lyne, B. C. Joshi, M. A. McLaughlin, M. Kramer, J. M. Sarkissian, F. Camilo, V. Kalogera, C. Kim, and D. R. Lorimer. An increased estimate of the merger rate of double neutron stars from observations of a highly relativistic system. *Nature*, 426(6966):531–533, December 2003. doi: 10.1038/nature02124.

David N. Burrows, J. E. Hill, J. A. Nousek, J. A. Kennea, A. Wells, J. P. Osborne, A. F. Abbey, A. Beardmore, K. Mukerjee, A. D. T. Short, G. Chincarini, S. Campana, O. Citterio, A. Moretti, C. Pagani, G. Tagliaferri, P. Giommi, M. Capalbi, F. Tamburelli, L. Angelini, G. Cusumano, H. W. Bräuninger, W. Burkert, and G. D. Hartner. The Swift X-Ray Telescope. *Space Sci. Rev.*, 120(3-4): 165–195, October 2005. doi: 10.1007/s11214-005-5097-2.

O. W. Butters, A. J. Norton, P. Hakala, K. Mukai, and E. J. Barlow. RXTE determination of the intermediate polar status of XSS J00564+4548, IGR J17195-4100, and XSS J12270-4859. *A&A*, 487 (1):271–276, August 2008. doi: 10.1051/0004-6361:200809942.

F. Camilo. Intermediate-Mass Binary Pulsars: a New Class of Objects? In S. Johnston, M. A. Walker, and M. Bailes, editors, *IAU Colloq. 160: Pulsars: Problems and Progress*, volume 105 of *Astronomical Society of the Pacific Conference Series*, page 539, January 1996.

S. Campana, M. Colpi, S. Mereghetti, L. Stella, and M. Tavani. The neutron stars of Soft X-ray Transients. *A&ARv*, 8(4):279–316, January 1998. doi: 10.1007/s001590050012.

S. Campana, G. L. Israel, L. Stella, F. Gastaldello, and S. Mereghetti. The Variable Quiescence of Centaurus X-4. *ApJ*, 601(1):474–478, January 2004. doi: 10.1086/380194.

S. Campana, F. Coti Zelati, A. Papitto, N. Rea, D. F. Torres, M. C. Baglio, and P. D'Avanzo. A physical scenario for the high and low X-ray luminosity states in the transitional pulsar PSR J1023+0038. *A&A*, 594:A31, October 2016. doi: 10.1051/0004-6361/201629035.

S. Campana, A. Miraval Zanon, F. Coti Zelati, D. F. Torres, M. C. Baglio, and A. Papitto. Probing X-ray emission in different modes of PSR J1023+0038 with a radio pulsar scenario. *A&A*, 629:L8, September 2019. doi: 10.1051/0004-6361/201936312.

Sergio Campana and Tiziana Di Salvo. *Accreting Pulsars: Mixing-up Accretion Phases in Transitional Systems*, volume 457 of *Astrophysics and Space Science Library*, page 149. 2018. doi: 10.1007/978-3-319-97616-7_4.

Sergio Campana, Luigi Stella, Sandro Mereghetti, and Domitilla de Martino. A universal relation for the propeller mechanisms in magnetic rotating stars at different scales. *A&A*, 610:A46, February 2018. doi: 10.1051/0004-6361/201730769.

J. Casares, M. Mouchet, I. G. Martinez-Pais, and E. T. Harlaftis. A coordinated campaign on the intermediate polar AE AQR - I. The system parameters. *MNRAS*, 282(1):182–190, September 1996. doi: 10.1093/mnras/282.1.182.

Deepto Chakrabarty and Edward H. Morgan. The two-hour orbit of a binary millisecond X-ray pulsar. *Nature*, 394(6691):346–348, July 1998. doi: 10.1038/28561.

Nicolas Chamel and Pawel Haensel. Physics of Neutron Star Crusts. *Living Reviews in Relativity*, 11(1):10, December 2008. doi: 10.12942/lrr-2008-10.

Patricia B. Cho, Jules P. Halpern, and Slavko Bogdanov. Variable Heating and Flaring of Three Redback Millisecond Pulsar Companions. *ApJ*, 866(1):71, October 2018. doi: 10.3847/1538-4357/aade92.

G. Chodil, Hans Mark, R. Rodrigues, F. D. Seward, and C. D. Swift. X-Ray Intensities and Spectra from Several Cosmic Sources. *ApJ*, 150:57, October 1967. doi: 10.1086/149312.

Stirling A. Colgate and Richard H. White. The Hydrodynamic Behavior of Supernovae Explosions. *ApJ*, 143:626, March 1966. doi: 10.1086/148549.

F. V. Coroniti. Magnetically Striped Relativistic Magnetohydrodynamic Winds: The Crab Nebula Revisited. *ApJ*, 349:538, February 1990. doi: 10.1086/168340.

F. Coti Zelati, M. C. Baglio, S. Campana, P. D'Avanzo, P. Goldoni, N. Masetti, T. Muñoz-Darias, S. Covino, R. P. Fender, E. Jiménez Bailón, H. Otí-Floranes, E. Palazzi, and F. G. Ramón-Fox. Engulfing a radio pulsar: the case of PSR J1023+0038. *MNRAS*, 444(2): 1783–1792, October 2014. doi: 10.1093/mnras/stu1552.

F. Coti Zelati, S. Campana, V. Braito, M. C. Baglio, P. D'Avanzo, N. Rea, and D. F. Torres. Simultaneous broadband observations and high-resolution X-ray spectroscopy of the transitional millisecond pulsar PSR J1023+0038. *A&A*, 611:A14, March 2018. doi: 10.1051/0004-6361/201732244.

Francesco Coti Zelati, Alessandro Papitto, Domitilla de Martino, David A. H. Buckley, Alida Odendaal, Jian Li, Thomas D. Russell, Diego F. Torres, Simona M. Mazzola, Enrico Bozzo, Mariusz Gromadzki, Sergio Campana, Nanda Rea, Carlo Ferrigno, and Simone Migliari. Prolonged sub-luminous state of the new transitional pulsar candidate CXOU J110926.4-650224. *A&A*, 622:A211, February 2019. doi: 10.1051/0004-6361/201834835.

H. T. Cromartie, F. Camilo, M. Kerr, J. S. Deneva, S. M. Ransom, P. S. Ray, E. C. Ferrara, P. F. Michelson, and K. S. Wood. Six New Millisecond Pulsars from Arecibo Searches of Fermi Gamma-Ray Sources. *ApJ*, 819(1):34, March 2016. doi: 10.3847/0004-637X/819/1/34.

Joseph K. Daugherty and Alice K. Harding. Compton Scattering in Strong Magnetic Fields. *ApJ*, 309:362, October 1986. doi: 10.1086/164608.

Kris Davidson and Jeremiah P. Ostriker. Neutron-Star Accretion in a Stellar Wind: Model for a Pulsed X-Ray Source. *ApJ*, 179:585–598, January 1973. doi: 10.1086/151897.

R. E. Davies and J. E. Pringle. Spindown of neutron stars in close binary systems - II. *MNRAS*, 196:209–224, July 1981. doi: 10.1093/mnras/196.2.209.

D. de Martino, M. Falanga, J. M. Bonnet-Bidaud, T. Belloni, M. Mouchet, N. Masetti, I. Andruchow, S. A. Cellone, K. Mukai, and G. Matt. The intriguing nature of the high-energy gamma ray source XSS J12270-4859. *A&A*, 515:A25, June 2010. doi: 10.1051/0004-6361/200913802.

D. de Martino, J. Casares Velazquez, E. Mason, M. Kotze, D. A. H. Buckley, J. M. Bonnet-Bidaud, T. Belloni, M. Mouchet, and M. Falanga. Spectroscopic observations of the peculiar low-mass X-ray binary XSS J12270-4859. *The Astronomer's Telegram*, 5651: 1, December 2013.

D. de Martino, J. Casares, E. Mason, D. A. H. Buckley, M. M. Kotze, J. M. Bonnet-Bidaud, M. Mouchet, R. Coppejans, and A. A. S. Gulbis. Unveiling the redback nature of the low-mass X-ray binary XSS J1227.0-4859 through optical observations. *MNRAS*, 444(4): 3004–3014, November 2014. doi: 10.1093/mnras/stu1640.

D. de Martino, A. Papitto, T. Belloni, M. Burgay, E. De Ona Wilhelmi, J. Li, A. Pellizzoni, A. Possenti, N. Rea, and D. F. Torres. Multiwavelength observations of the transitional millisecond pulsar binary XSS J12270-4859. *MNRAS*, 454(2):2190–2198, December 2015. doi: 10.1093/mnras/stv2109.

D. de Martino, A. Papitto, M. Burgay, A. Possenti, F. Coti Zelati, N. Rea, D. F. Torres, and T. M. Belloni. NuSTAR and Parkes observations of the transitional millisecond pulsar binary XSS J12270-4859 in the rotation-powered state. *MNRAS*, 492(4):5607–5619, March 2020. doi: 10.1093/mnras/staa164.

N. Degenaar, R. Wijnands, M. T. Reynolds, J. M. Miller, D. Altamirano, J. Kennea, N. Gehrels, D. Haggard, and G. Ponti. The Peculiar Galactic Center Neutron Star X-Ray Binary XMM J174457-2850.3. *ApJ*, 792(2):109, September 2014. doi: 10.1088/0004-637X/792/2/109.

A. T. Deller, A. M. Archibald, W. F. Brisken, S. Chatterjee, G. H. Janssen, V. M. Kaspi, D. Lorimer, A. G. Lyne, M. A. McLaughlin, S. Ransom, I. H. Stairs, and B. Stappers. A Parallax Distance and Mass Estimate for the Transitional Millisecond Pulsar System J1023+0038. *ApJ*, 756(2):L25, September 2012. doi: 10.1088/2041-8205/756/2/L25.

J. S. Deneva, P. S. Ray, F. Camilo, J. P. Halpern, K. Wood, H. T. Cromartie, E. Ferrara, M. Kerr, S. M. Ransom, M. T. Wolff, K. C. Chambers, and E. A. Magnier. Multiwavelength Observations of the Redback Millisecond Pulsar J1048+2339. *ApJ*, 823(2):105, June 2016. doi: 10.3847/0004-637X/823/2/105.

J. S. Deneva, P. S. Ray, F. Camilo, P. C. C. Freire, H. T. Cromartie, S. M. Ransom, E. Ferrara, M. Kerr, T. H. Burnett, and P. M. Saz Parkinson. Timing of Eight Binary Millisecond Pulsars Found with Arecibo in Fermi-LAT Unidentified Sources. *arXiv e-prints*, art. arXiv:2012.15185, December 2020.

J. D. M. Dewi and O. R. Pols. The late stages of evolution of helium star-neutron star binaries and the formation of double neutron star systems. *MNRAS*, 344(2):629–643, September 2003. doi: 10.1046/j.1365-8711.2003.06844.x.

J. D. M. Dewi, O. R. Pols, G. J. Savonije, and E. P. J. van den Heuvel. The evolution of naked helium stars with a neutron star companion in close binary systems. *MNRAS*, 331(4):1027–1040, April 2002. doi: 10.1046/j.1365-8711.2002.05257.x.

T. Di Salvo, A. Sanna, L. Burderi, A. Papitto, R. Iaria, A. F. Gambino, and A. Riggio. NuSTAR and XMM-Newton broad-band spectrum of SAX J1808.4-3658 during its latest outburst in 2015. *MNRAS*, 483(1):767–779, February 2019. doi: 10.1093/mnras/sty2974.

Tiziana Di Salvo and Andrea Sanna. Accretion powered X-ray millisecond pulsars. *arXiv e-prints*, art. arXiv:2010.09005, October 2020.

D. Eckert, M. Del Santo, A. Bazzano, K. Watanabe, A. Paizis, E. Bozzo, C. Ferrigno, I. Caballero, L. Sidoli, and L. Kuiper. IGR J18245-2452: a new hard X-ray transient discovered by INTEGRAL. *The Astronomer's Telegram*, 4925:1, March 2013.

P. P. Eggleton. Aproximations to the radii of Roche lobes. *ApJ*, 268: 368–369, May 1983. doi: 10.1086/160960.

K. Yavuz Ekşİ and M. Alİ Alpar. Disks Surviving the Radiation Pressure of Radio Pulsars. *ApJ*, 620(1):390–397, February 2005. doi: 10.1086/425959.

P. Elebert, M. T. Reynolds, P. J. Callanan, D. J. Hurley, G. Ramsay, F. Lewis, D. M. Russell, B. Nord, S. R. Kane, D. L. Depoy, and P. Hakala. Optical spectroscopy and photometry of SAX J1808.4-3658 in outburst. *MNRAS*, 395(2):884–894, May 2009. doi: 10.1111/j.1365-2966.2009.14562.x.

P. A. Evans, A. P. Beardmore, K. L. Page, J. P. Osborne, P. T. O'Brien, R. Willingale, R. L. C. Starling, D. N. Burrows, O. Godet, L. Vetere, J. Racusin, M. R. Goad, K. Wiersema, L. Angelini, M. Capalbi, G. Chincarini, N. Gehrels, J. A. Kennea, R. Margutti, D. C. Morris, C. J. Mountford, C. Pagani, M. Perri, P. Romano, and N. Tanvir. Methods and results of an automatic analysis of a complete sample of Swift-XRT observations of GRBs. *MNRAS*, 397(3): 1177–1201, August 2009. doi: 10.1111/j.1365-2966.2009.14913.x.

C. Ferrigno, E. Bozzo, A. Papitto, N. Rea, L. Pavan, S. Campana, M. Wieringa, M. Filipović, M. Falanga, and L. Stella. Hiccup accretion in the swinging pulsar IGR J18245-2452. *A&A*, 567:A77, July 2014. doi: 10.1051/0004-6361/201322904.

Edward L. Fitzpatrick. Correcting for the Effects of Interstellar Extinction. *PASP*, 111(755):63–75, January 1999. doi: 10.1086/316293.

Dillon R. Foight, Tolga Güver, Feryal Özel, and Patrick O. Slane. Probing X-Ray Absorption and Optical Extinction in the Interstellar Medium Using Chandra Observations of Supernova Remnants. *ApJ*, 826(1):66, July 2016. doi: 10.3847/0004-637X/826/1/66.

A. S. Fruchter, D. R. Stinebring, and J. H. Taylor. A millisecond pulsar in an eclipsing binary. *Nature*, 333(6170):237–239, May 1988. doi: 10.1038/333237a0.

Duncan K. Galloway and Andrew Cumming. Helium-rich Thermonuclear Bursts and the Distance to the Accretion-powered Millisecond Pulsar SAX J1808.4-3658. *ApJ*, 652(1):559–568, November 2006. doi: 10.1086/507598.

M. Gedalin and D. Eichler. Nonlinear Plasma Mechanisms of Pulsar Eclipse in Binary Systems. *ApJ*, 406:629, April 1993. doi: 10.1086/172474.

N. Gehrels, G. Chincarini, P. Giommi, K. O. Mason, J. A. Nousek, A. A. Wells, N. E. White, S. D. Barthelmy, D. N. Burrows, L. R. Cominsky, K. C. Hurley, F. E. Marshall, P. Mészáros, P. W. A. Roming, L. Angelini, L. M. Barbier, T. Belloni, S. Campana, P. A. Caraveo, M. M. Chester, O. Citterio, T. L. Cline, M. S. Cropper, J. R. Cummings, A. J. Dean, E. D. Feigelson, E. E. Fenimore, D. A. Frail, A. S. Fruchter, G. P. Garmire, K. Gendreau, G. Ghisellini,

J. Greiner, J. E. Hill, S. D. Hunsberger, H. A. Krimm, S. R. Kulkarni, P. Kumar, F. Lebrun, N. M. Lloyd-Ronning, C. B. Markwardt, B. J. Mattson, R. F. Mushotzky, J. P. Norris, J. Osborne, B. Paczynski, D. M. Palmer, H. S. Park, A. M. Parsons, J. Paul, M. J. Rees, C. S. Reynolds, J. E. Rhoads, T. P. Sasseen, B. E. Schaefer, A. T. Short, A. P. Smale, I. A. Smith, L. Stella, G. Tagliaferri, T. Takahashi, M. Tashiro, L. K. Townsley, J. Tueller, M. J. L. Turner, M. Vietri, W. Voges, M. J. Ward, R. Willingale, F. M. Zerbi, and W. W. Zhang. The Swift Gamma-Ray Burst Mission. *ApJ*, 611(2): 1005–1020, August 2004. doi: 10.1086/422091.

Keith Gendreau and Zaven Arzoumanian. Searching for a pulse. *Nature Astron.*, 1:895–895, December 2017. doi: 10.1038/s41550-017-0301-3.

Keith C. Gendreau, Zaven Arzoumanian, Phillip W. Adkins, Cheryl L. Albert, John F. Anders, Andrew T. Aylward, Charles L. Baker, Erin R. Balsamo, William A. Bamford, Suyog S. Benegalrao, Daniel L. Berry, Shiraz Bhalwani, J. Kevin Black, Carl Blaurock, Ginger M. Bronke, Gary L. Brown, Jason G. Budinoff, Jeffrey D. Cantwell, Thoniel Cazeau, Philip T. Chen, Thomas G. Clement, Andrew T. Colangelo, Jerry S. Coleman, Jonathan D. Coopersmith, William E. Dehaven, John P. Doty, Mark D. Egan, Teruaki Enoto, Terry W. Fan, Deneen M. Ferro, Richard Foster, Nicholas M. Galassi, Luis D. Gallo, Chris M. Green, Dave Grosh, Kong Q. Ha, Monther A. Hasouneh, Kristofer B. Heefner, Phyllis Hestnes, Lisa J. Hoge, Tawanda M. Jacobs, John L. Jørgensen, Michael A. Kaiser, James W. Kellogg, Steven J. Kenyon, Richard G. Koenecke, Robert P. Kozon, Beverly LaMarr, Mike D. Lambertson, Anne M. Larson, Steven Lentine, Jesse H. Lewis, Michael G. Lilly, Kuochia Alice Liu, Andrew Malonis, Sridhar S. Manthripragada, Craig B. Markwardt, Bryan D. Matonak, Isaac E. Mcginnis,

Roger L. Miller, Alissa L. Mitchell, Jason W. Mitchell, Jelila S. Mohammed, Charles A. Monroe, Kristina M. Montt de Garcia, Peter D. Mulé, Louis T. Nagao, Son N. Ngo, Eric D. Norris, Dwight A. Norwood, Joseph Novotka, Takashi Okajima, Lawrence G. Olsen, Chimaobi O. Onyeachu, Henry Y. Orosco, Jacqualine R. Peterson, Kristina N. Pevear, Karen K. Pham, Sue E. Pollard, John S. Pope, Daniel F. Powers, Charles E. Powers, Samuel R. Price, Gregory Y. Prigozhin, Julian B. Ramirez, Winston J. Reid, Ronald A. Remillard, Eric M. Rogstad, Glenn P. Rosecrans, John N. Rowe, Jennifer A. Sager, Claude A. Sanders, Bruce Savadkin, Maxine R. Saylor, Alexander F. Schaeffer, Nancy S. Schweiss, Sean R. Semper, Peter J. Serlemitsos, Larry V. Shackelford, Yang Soong, Jonathan Struebel, Michael L. Vezie, Joel S. Villasenor, Luke B. Winternitz, George I. Wofford, Michael R. Wright, Mike Y. Yang, and Wayne H. Yu. The Neutron star Interior Composition Explorer (NICER): design and development. In *Proc. SPIE*, volume 9905 of *Society of Photo-Optical Instrumentation Engineers (SPIE) Conference Series*, page 99051H, July 2016. doi: 10.1117/12.2231304.

A. Ghedina, F. Leone, F. Ambrosino, F. Meddi, A. Papitto, L. Riverol, M. Hernandez, M. Cecconi, M. D. Gonzalez G., H. Perez Ventura, and J. J. San Juan. SIFAP2: a new versatile configuration at the TNG for the MPPC based photometer. In *Proc. SPIE*, volume 10702 of *Society of Photo-Optical Instrumentation Engineers (SPIE) Conference Series*, page 107025Q, July 2018. doi: 10.1117/12.2316348.

P. Ghosh and F. K. Lamb. Disk accretion by magnetic neutron stars. *ApJ*, 223:L83–L87, July 1978. doi: 10.1086/182734.

P. Ghosh and F. K. Lamb. Accretion by rotating magnetic neutron stars. III. Accretion torques and period changes in pulsating X-ray sources. *ApJ*, 234:296–316, November 1979. doi: 10.1086/157498.

Marek Gierliński, Chris Done, and Didier Barret. Phase-resolved X-ray spectroscopy of the millisecond pulsar SAX J1808.4-3658. *MNRAS*, 331(1):141–153, March 2002. doi: 10.1046/j.1365-8711.2002.05174.x.

A. B. Giles, K. M. Hill, and J. G. Greenhill. The optical counterpart of SAX J1808.4 - 3658, the transient bursting millisecond X-ray pulsar. *MNRAS*, 304(1):47–51, March 1999. doi: 10.1046/j.1365-8711.1999.02361.x.

M. Gilfanov, M. Revnivtsev, R. Sunyaev, and E. Churazov. The millisecond X-ray pulsar/burster SAX J1808.4-3658: the outburst light curve and the power law spectrum. *A&A*, 338:L83–L86, October 1998.

Sivan Ginzburg and Eliot Quataert. Black widow evolution: magnetic braking by an ablated wind. *MNRAS*, 495(4):3656–3665, May 2020a. doi: 10.1093/mnras/staa1304.

Sivan Ginzburg and Eliot Quataert. Black widow formation by pulsar irradiation and sustained magnetic braking. *arXiv e-prints*, art. arXiv:2008.06506, August 2020b.

T. Gold. Rotating Neutron Stars as the Origin of the Pulsating Radio Sources. *Nature*, 218(5143):731–732, May 1968. doi: 10.1038/218731a0.

Thomas Gold. Rotating Neutron Stars and the Nature of Pulsars. *Nature*, 221(5175):25–27, January 1969. doi: 10.1038/221025a0.

Peter Goldreich and William H. Julian. Pulsar Electrodynamics. *ApJ*, 157:869, August 1969. doi: 10.1086/150119.

Adelle J. Goodwin, David M. Russell, Duncan K. Galloway, Jean J. M. in't Zand, Craig Heinke, Fraser Lewis, and Maria Cristina

Baglio. Likely new outburst of the accretion-powered millisecond pulsar SAX J1808.4-3658 indicated by increased optical and X-ray intensity. *The Astronomer's Telegram*, 12993:1, August 2019.

Pasi Hakala and Jari J. E. Kajava. Variable polarisation and Doppler tomography of PSR J1023+0038 - Evidence for the magnetic propeller during flaring? *MNRAS*, 474(3):3297–3306, March 2018. doi: 10.1093/mnras/stx2922.

J. P. Halpern, E. Gaidos, A. Sheffield, A. M. Price-Whelan, and S. Bogdanov. Optical Observations of the Binary MSP J1023+0038 in a New Accreting State. *The Astronomer's Telegram*, 5514:1, October 2013.

J. P. Halpern, J. Strader, and M. Li. A Likely Redback Millisecond Pulsar Counterpart of 3FGL J0838.8-2829. *ApJ*, 844(2):150, August 2017a. doi: 10.3847/1538-4357/aa7cff.

Jules P. Halpern, Slavko Bogdanov, and John R. Thorstensen. X-Ray and Optical Study of the Gamma-ray Source 3FGL J0838.8-2829: Identification of a Candidate Millisecond Pulsar Binary and an Asynchronous Polar. *ApJ*, 838(2):124, April 2017b. doi: 10.3847/1538-4357/838/2/124.

Alice K. Harding, Constantinos Kalapotharakos, Monica Barnard, and Christo Venter. Multi-TeV Emission from the Vela Pulsar. *ApJ*, 869 (1):L18, December 2018. doi: 10.3847/2041-8213/aaf3b2.

Jacob M. Hartman, Alessandro Patruno, Deepto Chakrabarty, David L. Kaplan, Craig B. Markwardt, Edward H. Morgan, Paul S. Ray, Michiel van der Klis, and Rudy Wijnands. The Long-Term Evolution of the Spin, Pulse Shape, and Orbit of the Accretion-powered Millisecond Pulsar SAX J1808.4-3658. *ApJ*, 675(2):1468–1486, March 2008. doi: 10.1086/527461.

P. R. Hebbar, C. O. Heinke, D. Kandel, R. W. Romani, and P. C. C. Freire. On the vanishing orbital X-ray variability of the eclipsing binary millisecond pulsar 47 Tuc W. *MNRAS*, October 2020. doi: 10.1093/mnras/staa3072.

C. O. Heinke, A. Bahramian, R. Wijnands, and D. Altamirano. IGR J18245-2452 is a new transient located in the core of the globular cluster M28. *The Astronomer's Telegram*, 4927:1, March 2013.

Jason W. T. Hessels, Scott M. Ransom, Ingrid H. Stairs, Paulo C. C. Freire, Victoria M. Kaspi, and Fernando Camilo. A Radio Pulsar Spinning at 716 Hz. *Science*, 311(5769):1901–1904, March 2006. doi: 10.1126/science.1123430.

A. Hewish, S. J. Bell, J. D. H. Pilkington, P. F. Scott, and R. A. Collins. Observation of a Rapidly Pulsating Radio Source. *Nature*, 217(5130):709–713, February 1968. doi: 10.1038/217709a0.

Johann A. Hibschman and Jonathan Arons. Pair Production Multiplicities in Rotation-powered Pulsars. *ApJ*, 560(2):871–884, October 2001. doi: 10.1086/323069.

A. B. Hill, A. Szostek, S. Corbel, F. Camilo, R. H. D. Corbet, R. Dubois, G. Dubus, P. G. Edwards, E. C. Ferrara, M. Kerr, E. Koerding, D. Kozieł, and Ł. Stawarz. The bright unidentifiedγ-ray source 1FGL J1227.9-4852: can it be associated with a low-mass X-ray binary? *MNRAS*, 415(1):235–243, July 2011. doi: 10.1111/j.1365-2966.2011.18692.x.

G. B. Hobbs, R. T. Edwards, and R. N. Manchester. TEMPO2, a new pulsar-timing package - I. An overview. *MNRAS*, 369(2):655–672, June 2006. doi: 10.1111/j.1365-2966.2006.10302.x.

R. A. Hulse and J. H. Taylor. Discovery of a pulsar in a binary system. *ApJ*, 195:L51–L53, January 1975. doi: 10.1086/181708.

Jarrod R. Hurley, Christopher A. Tout, Dayal T. Wickramasinghe, Lilia Ferrario, and Paul D. Kiel. Formation of binary millisecond pulsars by accretion-induced collapse of white dwarfs. *MNRAS*, 402 (3):1437–1448, March 2010. doi: 10.1111/j.1365-2966.2009.15988.x.

M. N. Iacolina, M. Burgay, L. Burderi, A. Possenti, and T. di Salvo. Search for pulsations at high radio frequencies from accreting millisecond X-ray pulsars in quiescence. *A&A*, 519:A13, September 2010. doi: 10.1051/0004-6361/201014025.

A. F. Illarionov and R. A. Sunyaev. Why the Number of Galactic X-ray Stars Is so Small? *A&A*, 39:185, February 1975.

J. J. M. in 't Zand, J. Heise, J. M. Muller, A. Bazzano, M. Cocchi, L. Natalucci, and P. Ubertini. Discovery of the X-ray transient SAX J1808.4-3658, a likely low-mass X-ray binary. *A&A*, 331:L25–L28, March 1998.

Natalia Ivanova and Ronald E. Taam. Thermal Timescale Mass Transfer and the Evolution of White Dwarf Binaries. *ApJ*, 601(2):1058–1066, February 2004. doi: 10.1086/380561.

Amruta Jaodand, Anne M. Archibald, Jason W. T. Hessels, Slavko Bogdanov, Caroline R. D'Angelo, Alessand ro Patruno, Cees Bassa, and Adam T. Deller. Timing Observations of PSR J1023+0038 During a Low-mass X-Ray Binary State. *ApJ*, 830(2):122, October 2016a. doi: 10.3847/0004-637X/830/2/122.

Amruta Jaodand, Anne M. Archibald, Jason W. T. Hessels, Slavko Bogdanov, Caroline R. D'Angelo, Alessand ro Patruno, Cees Bassa, and Adam T. Deller. Timing Observations of PSR J1023+0038 During a Low-mass X-Ray Binary State. *ApJ*, 830(2):122, October 2016b. doi: 10.3847/0004-637X/830/2/122.

T. J. Johnson, P. S. Ray, J. Roy, C. C. Cheung, A. K. Harding, H. J. Pletsch, S. Fort, F. Camilo, J. Deneva, B. Bhattacharyya, B. W. Stappers, and M. Kerr. Discovery of Gamma-Ray Pulsations from the Transitional Redback PSR J1227-4853. *ApJ*, 806(1):91, June 2015. doi: 10.1088/0004-637X/806/1/91.

Oleg Kargaltsev, George G. Pavlov, and Roger W. Romani. Ultraviolet Emission from the Millisecond Pulsar J0437-4715. *ApJ*, 602(1):327–335, February 2004. doi: 10.1086/380993.

J. G. Kirk, O. Skjæraasen, and Y. A. Gallant. Pulsed radiation from neutron star winds. *A&A*, 388:L29–L32, June 2002. doi: 10.1051/0004-6361:20020599.

W. Kluźniak and S. Rappaport. Magnetically Torqued Thin Accretion Disks. *ApJ*, 671(2):1990–2005, December 2007. doi: 10.1086/522954.

W. Kluzniak, M. Ruderman, J. Shaham, and M. Tavani. Nature and evolution of the eclipsing millisecond binary pulsar PSR1957 + 20. *Nature*, 334(6179):225–227, July 1988. doi: 10.1038/334225a0.

P. Kosec, C. Pinto, A. C. Fabian, and D. J. Walton. Searching for outflows in ultraluminous X-ray sources through high-resolution X-ray spectroscopy. *MNRAS*, 473(4):5680–5697, February 2018. doi: 10.1093/mnras/stx2695.

Aya Kubota, Yasuo Tanaka, Kazuo Makishima, Yoshihiro Ueda, Tadayasu Dotani, Hajime Inoue, and Kazutaka Yamaoka. Evidence for a Black Hole in the X-Ray Transient GRS 1009-45. *PASJ*, 50:667–673, December 1998. doi: 10.1093/pasj/50.6.667.

F. K. Lamb, C. J. Pethick, and D. Pines. A Model for Compact X-Ray Sources: Accretion by Rotating Magnetic Stars. *ApJ*, 184:271–290, August 1973. doi: 10.1086/152325.

M. I. Large, A. E. Vaughan, and B. Y. Mills. A Pulsar Supernova Association? *Nature*, 220(5165):340–341, October 1968. doi: 10.1038/220340a0.

K. D. Lawson, C. J. Mayer, J. L. Osborne, and M. L. Parkinson. Variations in the spectral index of the galactic radio continuum emission in the northern hemisphere. *MNRAS*, 225:307–327, March 1987. doi: 10.1093/mnras/225.2.307.

D. A. Leahy. Searches for pulsed emission - Improved determination of period and amplitude from epoch folding for sinusoidal signals. *A&A*, 180(1-2):275–277, June 1987.

D. A. Leahy, R. F. Elsner, and M. C. Weisskopf. On searches for periodic pulsed emission - The Rayleigh test compared to epoch folding. *ApJ*, 272:256–258, September 1983. doi: 10.1086/161288.

C. Leong, E. Kellogg, H. Gursky, H. Tananbaum, and R. Giacconi. X-Ray Emission from the Magellanic Clouds Observed by UHURU. *ApJ*, 170:L67, December 1971. doi: 10.1086/180842.

Kwan-Lok Li, Jay Strader, James C. A. Miller-Jones, Craig O. Heinke, and Laura Chomiuk. The Flare-dominated Accretion Mode of a Radio-bright Candidate Transitional Millisecond Pulsar. *ApJ*, 895 (2):89, June 2020. doi: 10.3847/1538-4357/ab8f28.

M. Linares. X-Ray States of Redback Millisecond Pulsars. *ApJ*, 795 (1):72, November 2014. doi: 10.1088/0004-637X/795/1/72.

M. Linares, T. Shahbaz, and J. Casares. Peering into the Dark Side: Magnesium Lines Establish a Massive Neutron Star in PSR J2215+5135. *ApJ*, 859(1):54, May 2018. doi: 10.3847/1538-4357/aabde6.

Vladimir Mikhailovich Lipunov. *Astrophysics of neutron stars*. 1987.

Q. Z. Liu, J. van Paradijs, and E. P. J. van den Heuvel. A catalogue of low-mass X-ray binaries in the Galaxy, LMC, and SMC (Fourth edition). *A&A*, 469(2):807–810, July 2007. doi: 10.1051/0004-6361:20077303.

D. R. Lorimer and M. Kramer. *Handbook of Pulsar Astronomy*, volume 4. 2004.

A. G. Lyne, M. Burgay, M. Kramer, A. Possenti, R. N. Manchester, F. Camilo, M. A. McLaughlin, D. R. Lorimer, N. D'Amico, B. C. Joshi, J. Reynolds, and P. C. C. Freire. A Double-Pulsar System: A Rare Laboratory for Relativistic Gravity and Plasma Physics. *Science*, 303(5661):1153–1157, February 2004. doi: 10.1126/science.1094645.

R. N. Manchester, A. G. Lyne, N. D'Amico, M. Bailes, S. Johnston, D. R. Lorimer, P. A. Harrison, L. Nicastro, and J. F. Bell. The Parkes Southern Pulsar Survey. I. Observing and data analysis systems and initial results. *MNRAS*, 279(4):1235–1250, April 1996. doi: 10.1093/mnras/279.4.1235.

L. Maraschi, R. Traversini, and A. Treves. A model for A0538-66: the fast flaring pulsar. *MNRAS*, 204:1179–1184, September 1983. doi: 10.1093/mnras/204.4.1179.

Ben Margalit and Brian D. Metzger. Constraining the Maximum Mass of Neutron Stars from Multi-messenger Observations of GW170817. *ApJ*, 850(2):L19, December 2017. doi: 10.3847/2041-8213/aa991c.

T. R. Marsh and Keith Horne. Images of accretion discs - II. Doppler tomography. *MNRAS*, 235:269–286, November 1988. doi: 10.1093/mnras/235.1.269.

N. Masetti, L. Morelli, E. Palazzi, G. Galaz, L. Bassani, A. Bazzano, A. J. Bird, A. J. Dean, G. L. Israel, R. Landi, A. Malizia, D. Minniti, F. Schiavone, J. B. Stephen, P. Ubertini, and R. Walter. Unveiling the nature of INTEGRAL objects through optical spectroscopy. V. Identification and properties of 21 southern hard X-ray sources. *A&A*, 459(1):21–30, November 2006. doi: 10.1051/0004-6361:20066055.

F. Meddi, F. Ambrosino, R. Nesci, C. Rossi, S. Sclavi, I. Bruni, A. Ruggieri, and S. Sestito. A New Fast Silicon Photomultiplier Photometer. *PASP*, 124(915):448, May 2012. doi: 10.1086/665925.

D. B. Melrose. Coherent emission mechanisms in astrophysical plasmas. *Reviews of Modern Plasma Physics*, 1(1):5, December 2017. doi: 10.1007/s41614-017-0007-0.

F. C. Michel. Origin of millisecond pulsars. *Nature*, 329(6137):310–312, September 1987. doi: 10.1038/329310a0.

Roberto P. Mignani. Optical, ultraviolet, and infrared observations of isolated neutron stars. *Advances in Space Research*, 47(8):1281–1293, April 2011. doi: 10.1016/j.asr.2009.12.011.

Jessie M. Miller, Samuel J. Swihart, Jay Strader, Ryan Urqhuart, Elias Aydi, Laura Chomiuk, Kristen C. Dage, Adam Kawash, Laura Shishkovsky, and Kirill V. Sokolovsky. A New Candidate Transitional Millisecond Pulsar in the Sub-luminous Disk State: 4FGL J0407.7–5702. *arXiv e-prints*, art. arXiv:2009.09054, September 2020.

A. Miraval Zanon, S. Campana, A. Ridolfi, P. D'Avanzo, and F. Ambrosino. X-ray study of high-and-low luminosity modes and peculiar low-soft-and-hard activity in the transitional pulsar XSS

J12270-4859. *A&A*, 635:A30, March 2020. doi: 10.1051/0004-6361/201936356.

G. Naletto, C. Barbieri, T. Occhipinti, I. Capraro, A. di Paola, C. Facchinetti, E. Verroi, P. Zoccarato, G. Anzolin, M. Belluso, S. Billotta, P. Bolli, G. Bonanno, V. da Deppo, S. Fornasier, C. Germanà, E. Giro, S. Marchi, F. Messina, C. Pernechele, F. Tamburini, M. Zaccariotto, and L. Zampieri. Iqueye, a single photon-counting photometer applied to the ESO new technology telescope. *A&A*, 508 (1):531–539, December 2009. doi: 10.1051/0004-6361/200912862.

Ramesh Narayan. Advection-dominated Models of Luminous Accreting Black Holes. *ApJ*, 462:136, May 1996. doi: 10.1086/177136.

Ramesh Narayan and Insu Yi. Advection-dominated Accretion: A Self-similar Solution. *ApJ*, 428:L13, June 1994. doi: 10.1086/187381.

J. R. Oppenheimer and G. M. Volkoff. On Massive Neutron Cores. *Physical Review*, 55(4):374–381, February 1939. doi: 10.1103/PhysRev.55.374.

Jeremiah Ostriker. Possible Model for a Rapidly Pulsating Radio Source. *Nature*, 217(5135):1227–1228, March 1968. doi: 10.1038/2171227a0.

F. Pacini. Energy Emission from a Neutron Star. *Nature*, 216(5115): 567–568, November 1967. doi: 10.1038/216567a0.

F. Pacini and M. Salvati. The optical luminosity of very fast pulsars. *ApJ*, 274:369–371, November 1983. doi: 10.1086/161452.

C. Pallanca, E. Dalessandro, F. R. Ferraro, B. Lanzoni, and G. Beccari. The Optical Counterpart to the X-Ray Transient IGR J1824-

24525 in the Globular Cluster M28. *ApJ*, 773(2):122, August 2013. doi: 10.1088/0004-637X/773/2/122.

A. Papitto and D. F. Torres. A Propeller Model for the Sub-luminous State of the Transitional Millisecond Pulsar PSR J1023+0038. *ApJ*, 807(1):33, July 2015. doi: 10.1088/0004-637X/807/1/33.

A. Papitto, T. Di Salvo, A. D'Aì, R. Iaria, L. Burderi, A. Riggio, M. T. Menna, and N. R. Robba. XMM-Newton detects a relativistically broadened iron line in the spectrum of the ms X-ray pulsar SAX J1808.4-3658. *A&A*, 493(3):L39–L43, January 2009. doi: 10.1051/0004-6361:200811401.

A. Papitto, A. Riggio, L. Burderi, T. di Salvo, A. D'Aí, and R. Iaria. Spin down during quiescence of the fastest known accretion-powered pulsar. *A&A*, 528:A55, April 2011. doi: 10.1051/0004-6361/201014837.

A. Papitto, C. Ferrigno, E. Bozzo, N. Rea, L. Pavan, L. Burderi, M. Burgay, S. Campana, T. di Salvo, M. Falanga, M. D. Filipović, P. C. C. Freire, J. W. T. Hessels, A. Possenti, S. M. Ransom, A. Riggio, P. Romano, J. M. Sarkissian, I. H. Stairs, L. Stella, D. F. Torres, M. H. Wieringa, and G. F. Wong. Swings between rotation and accretion power in a binary millisecond pulsar. *Nature*, 501(7468):517–520, September 2013. doi: 10.1038/nature12470.

A. Papitto, D. F. Torres, and Jian Li. A propeller scenario for the gamma-ray emission of low-mass X-ray binaries: the case of XSS J12270-4859. *MNRAS*, 438(3):2105–2116, March 2014. doi: 10.1093/mnras/stt2336.

A. Papitto, F. Ambrosino, L. Stella, D. Torres, F. Coti Zelati, A. Ghedina, F. Meddi, A. Sanna, P. Casella, Y. Dallilar, S. Eikenberry, G. L. Israel, F. Onori, S. Piranomonte, E. Bozzo, L. Burderi, S. Campana,

D. de Martino, T. Di Salvo, C. Ferrigno, N. Rea, A. Riggio, S. Serrano, A. Veledina, and L. Zampieri. Pulsating in Unison at Optical and X-Ray Energies: Simultaneous High Time Resolution Observations of the Transitional Millisecond Pulsar PSR J1023+0038. *ApJ*, 882(2):104, September 2019. doi: 10.3847/1538-4357/ab2fdf.

Alessandro Papitto and Domitilla de Martino. Transitional millisecond pulsars. *arXiv e-prints*, art. arXiv:2010.09060, October 2020.

Kyle Parfrey and Alexander Tchekhovskoy. General-relativistic Simulations of Four States of Accretion onto Millisecond Pulsars. *ApJ*, 851(2):L34, December 2017. doi: 10.3847/2041-8213/aa9c85.

Kyle Parfrey, Anatoly Spitkovsky, and Andrei M. Beloborodov. Torque Enhancement, Spin Equilibrium, and Jet Power from Disk-Induced Opening of Pulsar Magnetic Fields. *ApJ*, 822(1):33, May 2016. doi: 10.3847/0004-637X/822/1/33.

Kyle Parfrey, Anatoly Spitkovsky, and Andrei M. Beloborodov. Simulations of the magnetospheres of accreting millisecond pulsars. *MNRAS*, 469(3):3656–3669, August 2017. doi: 10.1093/mnras/stx950.

L. E. Pasinetti Fracassini, L. Pastori, S. Covino, and A. Pozzi. Catalogue of Apparent Diameters and Absolute Radii of Stars (CADARS) - Third edition - Comments and statistics. *A&A*, 367: 521–524, February 2001. doi: 10.1051/0004-6361:20000451.

A. Patruno and A. L. Watts. Accreting Millisecond X-Ray Pulsars. *arXiv e-prints*, art. arXiv:1206.2727, June 2012.

A. Patruno, A. M. Archibald, J. W. T. Hessels, S. Bogdanov, B. W. Stappers, C. G. Bassa, G. H. Janssen, V. M. Kaspi, S. Tendulkar, and A. G. Lyne. A New Accretion Disk around the Missing Link

Binary System PSR J1023+0038. *ApJ*, 781(1):L3, January 2014. doi: 10.1088/2041-8205/781/1/L3.

Alessandro Patruno and Anna L. Watts. Accreting Millisecond X-ray Pulsars. *Astrophysics and Space Science Library*, 461:143–208, January 2021. doi: 10.1007/978-3-662-62110-3_4.

Alessandro Patruno, Amruta Jaodand, Lucien Kuiper, Peter Bult, Jason W. T. Hessels, Christian Knigge, Andrew R. King, Rudy Wijnands, and Michiel van der Klis. Radio Pulse Search and X-Ray Monitoring of SAX J1808.4-3658: What Causes Its Orbital Evolution? *ApJ*, 841(2):98, June 2017. doi: 10.3847/1538-4357/aa6f5b.

Saarah F. Pirbhoy, Maria Cristina Baglio, David M. Russell, D. M. Bramich, Payaswini Saikia, Aisha Al Yazeedi, and Fraser Lewis. XB-NEWS detection of a new outburst of MAXI J1348-630. *The Astronomer's Telegram*, 13451:1, February 2020.

E. J. Polzin, R. P. Breton, A. O. Clarke, V. I. Kondratiev, B. W. Stappers, J. W. T. Hessels, C. G. Bassa, J. W. Broderick, J. M. Grießmeier, C. Sobey, S. ter Veen, J. van Leeuwen, and P. Weltevrede. The low-frequency radio eclipses of the black widow pulsar J1810+1744. *MNRAS*, 476(2):1968–1981, May 2018. doi: 10.1093/mnras/sty349.

Simon F. Portegies Zwart and Lev R. Yungelson. The possible companions of young radio pulsars. *MNRAS*, 309(1):26–30, October 1999. doi: 10.1046/j.1365-8711.1999.02792.x.

Magaretha L. Pretorius. Time-resolved optical observations of five cataclysmic variables detected by INTEGRAL. *MNRAS*, 395(1): 386–393, May 2009. doi: 10.1111/j.1365-2966.2009.14521.x.

J. E. Pringle and M. J. Rees. Accretion Disc Models for Compact X-Ray Sources. *A&A*, 21:1, October 1972.

Rostislav Protassov, David A. van Dyk, Alanna Connors, Vinay L. Kashyap, and Aneta Siemiginowska. Statistics, Handle with Care: Detecting Multiple Model Components with the Likelihood Ratio Test. *ApJ*, 571(1):545–559, May 2002. doi: 10.1086/339856.

V. Radhakrishnan and G. Srinivasan. On the origin of the recently discovered ultra-rapid pulsar. *Current Science*, 51:1096–1099, December 1982.

S. M. Ransom, S. S. Eikenberry, and J. Middleditch. Fourier Techniques for Very Long Astrophysical Time-Series Analysis. *AJ*, 124: 1788–1809, September 2002. doi: 10.1086/342285.

Frederic A. Rasio, Stuart L. Shapiro, and Saul A. Teukolsky. What Is Causing the Eclipse in the Millisecond Binary Pulsar? *ApJ*, 342: 934, July 1989a. doi: 10.1086/167649.

Frederic A. Rasio, Stuart L. Shapiro, and Saul A. Teukolsky. What Is Causing the Eclipse in the Millisecond Binary Pulsar? *ApJ*, 342: 934, July 1989b. doi: 10.1086/167649.

A. Ridolfi, P. C. C. Freire, P. Torne, C. O. Heinke, M. van den Berg, C. Jordan, M. Kramer, C. G. Bassa, J. Sarkissian, N. D'Amico, D. Lorimer, F. Camilo, R. N. Manchester, and A. Lyne. Long-term observations of the pulsars in 47 Tucanae - I. A study of four elusive binary systems. *MNRAS*, 462(3):2918–2933, November 2016. doi: 10.1093/mnras/stw1850.

Mallory S. E. Roberts. Surrounded by spiders! New black widows and redbacks in the Galactic field. In Joeri van Leeuwen, editor, *Neutron Stars and Pulsars: Challenges and Opportunities after 80*

years, volume 291 of *IAU Symposium*, pages 127–132, March 2013. doi: 10.1017/S174392131202337X.

Roger W. Romani and Nicolas Sanchez. Intra-binary Shock Heating of Black Widow Companions. *ApJ*, 828(1):7, September 2016. doi: 10.3847/0004-637X/828/1/7.

Marina M. Romanova and Stanley P. Owocki. Accretion, Outflows, and Winds of Magnetized Stars. *Space Sci. Rev.*, 191(1-4):339–389, October 2015. doi: 10.1007/s11214-015-0200-9.

Peter W. A. Roming, Thomas E. Kennedy, Keith O. Mason, John A. Nousek, Lindy Ahr, Richard E. Bingham, Patrick S. Broos, Mary J. Carter, Barry K. Hancock, Howard E. Huckle, S. D. Hunsberger, Hajime Kawakami, Ronnie Killough, T. Scott Koch, Michael K. McLelland, Kelly Smith, Philip J. Smith, Juan Carlos Soto, Patricia T. Boyd, Alice A. Breeveld, Stephen T. Holland, Mariya Ivanushkina, Michael S. Pryzby, Martin D. Still, and Joseph Stock. The Swift Ultra-Violet/Optical Telescope. *Space Sci. Rev.*, 120(3-4): 95–142, October 2005. doi: 10.1007/s11214-005-5095-4.

J. Roy, B. Bhattacharyya, and P. S. Ray. GMRT discovery of a 1.69 ms radio pulsar associated with XSS J12270-4859. *The Astronomer's Telegram*, 5890:1, February 2014.

Jayanta Roy, Paul S. Ray, Bhaswati Bhattacharyya, Ben Stappers, Jayaram N. Chengalur, Julia Deneva, Fernando Camilo, Tyrel J. Johnson, Michael Wolff, Jason W. T. Hessels, Cees G. Bassa, Evan F. Keane, Elizabeth C. Ferrara, Alice K. Harding, and Kent S. Wood. Discovery of Psr J1227-4853: A Transition from a Low-mass X-Ray Binary to a Redback Millisecond Pulsar. *ApJ*, 800(1):L12, February 2015. doi: 10.1088/2041-8205/800/1/L12.

M. A. Ruderman and P. G. Sutherland. Theory of pulsars: polar gaps, sparks, and coherent microwave radiation. *ApJ*, 196:51–72, February 1975. doi: 10.1086/153393.

D. M. Russell, R. P. Fender, R. I. Hynes, C. Brocksopp, J. Homan, P. G. Jonker, and M. M. Buxton. Global optical/infrared-X-ray correlations in X-ray binaries: quantifying disc and jet contributions. *MNRAS*, 371(3):1334–1350, September 2006. doi: 10.1111/j.1365-2966.2006.10756.x.

David M. Russell, Daniel M. Bramich, Fraser Lewis, Aisha AlMannaei, Thabet Al Qaissieh, Ahlam Al Qasim, Aisha Al Yazeedi, Maria Cristina Baglio, Federico Bernardini, Nour Elgalad, Aldrin Gabuya, Jean-Pierre Lasota, Alejandro Palado, Paul Roche, Hinna Shivkumar, Silviu-Marian Udrescu, and Guobao Zhang. Optical precursors to X-ray binary outbursts. *Astronomische Nachrichten*, 340(4):278–283, May 2019. doi: 10.1002/asna.201913610.

George B. Rybicki and Alan P. Lightman. *Radiative processes in astrophysics*. 1979.

Kei Saitou, Masahiro Tsujimoto, Ken Ebisawa, and Manabu Ishida. Suzaku X-Ray Study of an Anomalous Source XSS J12270-4859. *PASJ*, 61:L13, August 2009. doi: 10.1093/pasj/61.4.L13.

Nicolas Sanchez and Roger W. Romani. B-ducted Heating of Black Widow Companions. *ApJ*, 845(1):42, August 2017. doi: 10.3847/1538-4357/aa7a02.

A. Sanna, A. Bahramian, E. Bozzo, C. Heinke, D. Altamirano, R. Wijnands, N. Degenaar, T. Maccarone, A. Riggio, T. Di Salvo, R. Iaria, M. Burgay, A. Possenti, C. Ferrigno, A. Papitto, G. R. Sivakoff,

N. D'Amico, and L. Burderi. Discovery of 105 Hz coherent pulsations in the ultracompact binary IGR J16597-3704. *A&A*, 610:L2, February 2018a. doi: 10.1051/0004-6361/201732262.

A. Sanna, C. Ferrigno, P. S. Ray, L. Ducci, G. K. Jaisawal, T. Enoto, E. Bozzo, D. Altamirano, T. Di Salvo, T. E. Strohmayer, A. Papitto, A. Riggio, L. Burderi, P. M. Bult, S. Bogdanov, A. F. Gambino, A. Marino, R. Iaria, Z. Arzoumanian, D. Chakrabarty, K. C. Gendreau, S. Guillot, C. Markwardt, and M. T. Wolff. NuSTAR and NICER reveal IGR J17591-2342 as a new accreting millisecond X-ray pulsar. *A&A*, 617:L8, October 2018b. doi: 10.1051/0004-6361/201834160.

A. Sanna, T. Di Salvo, L. Burderi, A. Riggio, A. Gambino, and R. Iaria. NuSTAR observation of the latest outburst of SAX J1808.4-3658. *The Astronomer's Telegram*, 13022:1, August 2019.

William C. Saslaw. Rapidly Pulsing Radio Sources. *Nature*, 217(5135): 1222–1227, March 1968. doi: 10.1038/2171222a0.

S. Yu. Sazonov and M. G. Revnivtsev. VizieR Online Data Catalog: AGNs from RXTE 3-20keV All-Sky Survey (Sazonov+, 2004). *VizieR Online Data Catalog*, art. J/A+A/423/469, May 2004a.

S. Yu. Sazonov and M. G. Revnivtsev. Statistical properties of local active galactic nuclei inferred from the RXTE 3-20 keV all-sky survey. *A&A*, 423:469–480, August 2004b. doi: 10.1051/0004-6361:20047150.

Edward F. Schlafly and Douglas P. Finkbeiner. Measuring Reddening with Sloan Digital Sky Survey Stellar Spectra and Recalibrating SFD. *ApJ*, 737(2):103, August 2011. doi: 10.1088/0004-637X/737/2/103.

K. Schwarzschild. On the Gravitational Field of a Mass Point According to Einstein's Theory. *Abh. Konigl. Preuss. Akad. Wissenschaften Jahre 1906,92, Berlin,1907*, 1916:189–196, January 1916.

T. Shahbaz, M. Linares, S. P. Nevado, P. Rodríguez-Gil, J. Casares, V. S. Dhillon, T. R. Marsh, S. Littlefair, A. Leckngam, and S. Poshyachinda. The binary millisecond pulsar PSR J1023+0038 during its accretion state - I. Optical variability. *MNRAS*, 453(4):3461–3473, November 2015. doi: 10.1093/mnras/stv1686.

G. Shaifullah, J. P. W. Verbiest, P. C. C. Freire, T. M. Tauris, N. Wex, S. Osłowski, B. W. Stappers, C. G. Bassa, R. N. Caballero, D. J. Champion, I. Cognard, G. Desvignes, E. Graikou, L. Guillemot, G. H. Janssen, A. Jessner, C. Jordan, R. Karuppusamy, M. Kramer, K. Lazaridis, P. Lazarus, A. G. Lyne, J. W. McKee, D. Perrodin, A. Possenti, and C. Tiburzi. 21 year timing of the black-widow pulsar J2051-0827. *MNRAS*, 462(1):1029–1038, October 2016. doi: 10.1093/mnras/stw1737.

N. I. Shakura and R. A. Sunyaev. Reprint of 1973A&A....24..337S. Black holes in binary systems. Observational appearance. *A&A*, 500:33–51, June 1973.

S. L. Shapiro and S. A. Teukolsky. Book-Review - Black-Holes White Dwarfs and Neutron Stars. *Journal of the British Astronomical Association*, 93(6):276, October 1983.

V. F. Shvartsman. On the generation of relativistic particles by neutron stars in the state of accretion. *Astrofizika*, 6:309–317, January 1970.

Sarah L. Smedley, Christopher A. Tout, Lilia Ferrario, and Dayal T. Wickramasinghe. Formation of redbacks via accretion-induced col-

lapse. *MNRAS*, 446(3):2540–2549, January 2015. doi: 10.1093/mnras/stu2252.

H. C. Spruit. Fast maximum entropy Doppler mapping. *arXiv e-prints*, art. arXiv:9806141, June 1998.

David H. Staelin and III Reifenstein, Edward C. Pulsating Radio Sources near the Crab Nebula. *Science*, 162(3861):1481–1483, December 1968. doi: 10.1126/science.162.3861.1481.

Ingrid H. Stairs. Pulsars in Binary Systems: Probing Binary Stellar Evolution and General Relativity. *Science*, 304(5670):547–552, April 2004. doi: 10.1126/science.1096986.

B. W. Stappers, J. W. T. Hessels, A. Alexov, K. Anderson, T. Coenen, T. Hassall, A. Karastergiou, V. I. Kondratiev, M. Kramer, J. van Leeuwen, J. D. Mol, A. Noutsos, J. W. Romein, P. Weltevrede, R. Fender, R. A. M. J. Wijers, L. Bähren, M. E. Bell, J. Broderick, E. J. Daw, V. S. Dhillon, J. Eislöffel, H. Falcke, J. Griessmeier, C. Law, S. Markoff, J. C. A. Miller-Jones, B. Scheers, H. Spreeuw, J. Swinbank, S. Ter Veen, M. W. Wise, O. Wucknitz, P. Zarka, J. Anderson, A. Asgekar, I. M. Avruch, R. Beck, P. Bennema, M. J. Bentum, P. Best, J. Bregman, M. Brentjens, R. H. van de Brink, P. C. Broekema, W. N. Brouw, M. Brüggen, A. G. de Bruyn, H. R. Butcher, B. Ciardi, J. Conway, R. J. Dettmar, A. van Duin, J. van Enst, M. Garrett, M. Gerbers, T. Grit, A. Gunst, M. P. van Haarlem, J. P. Hamaker, G. Heald, M. Hoeft, H. Holties, A. Horneffer, L. V. E. Koopmans, G. Kuper, M. Loose, P. Maat, D. McKay-Bukowski, J. P. McKean, G. Miley, R. Morganti, R. Nijboer, J. E. Noordam, M. Norden, H. Olofsson, M. Pandey-Pommier, A. Polatidis, W. Reich, H. Röttgering, A. Schoenmakers, J. Sluman, O. Smirnov, M. Steinmetz, C. G. M. Sterks, M. Tagger, Y. Tang, R. Vermeulen, N. Vermaas, C. Vogt, M. de Vos,

S. J. Wijnholds, S. Yatawatta, and A. Zensus. Observing pulsars and fast transients with LOFAR. *A&A*, 530:A80, June 2011. doi: 10.1051/0004-6361/201116681.

B. W. Stappers, A. M. Archibald, J. W. T. Hessels, C. G. Bassa, S. Bogdanov, G. H. Janssen, V. M. Kaspi, A. G. Lyne, A. Patruno, S. Tendulkar, A. B. Hill, and T. Glanzman. A State Change in the Missing Link Binary Pulsar System PSR J1023+0038. *ApJ*, 790(1): 39, July 2014. doi: 10.1088/0004-637X/790/1/39.

L. Stella, N. E. White, and R. Rosner. Intermittent Stellar Wind Acceleration and the Long-Term Activity of Population I Binary Systems Containing an X-Ray Pulsar. *ApJ*, 308:669, September 1986. doi: 10.1086/164538.

L. Stella, S. Campana, S. Mereghetti, D. Ricci, and G. L. Israel. The Discovery of Quiescent X-Ray Emission from SAX J1808.4-3658, the Transient 2.5 Millisecond Pulsar. *ApJ*, 537(2):L115–L118, July 2000. doi: 10.1086/312765.

Peter B. Stetson. Homogeneous Photometry for Star Clusters and Resolved Galaxies. II. Photometric Standard Stars. *PASP*, 112(773): 925–931, July 2000. doi: 10.1086/316595.

Jay Strader, Kwan-Lok Li, Laura Chomiuk, Craig O. Heinke, Andrzej Udalski, Mark Peacock, Laura Shishkovsky, and Evangelia Tremou. A New γ-Ray Loud, Eclipsing Low-mass X-Ray Binary. *ApJ*, 831 (1):89, November 2016. doi: 10.3847/0004-637X/831/1/89.

Jay Strader, Samuel Swihart, Laura Chomiuk, Arash Bahramian, Chris Britt, C. C. Cheung, Kristen Dage, Jules Halpern, Kwan-Lok Li, Roberto P. Mignani, Jerome A. Orosz, Mark Peacock, Ricardo

Salinas, Laura Shishkovsky, and Evangelia Tremou. Optical Spectroscopy and Demographics of Redback Millisecond Pulsar Binaries. *ApJ*, 872(1):42, February 2019. doi: 10.3847/1538-4357/aafbaa.

Tod E. Strohmayer, William Zhang, Jean H. Swank, Alan Smale, Lev Titarchuk, Charles Day, and Umin Lee. Millisecond X-Ray Variability from an Accreting Neutron Star System. *ApJ*, 469:L9, September 1996. doi: 10.1086/310261.

R. E. Taam and E. P. J. van den Heuvel. Magnetic Field Decay and the Origin of Neutron Star Binaries. *ApJ*, 305:235, June 1986. doi: 10.1086/164243.

Ronald E. Taam and Eric L. Sandquist. Common Envelope Evolution of Massive Binary Stars. *ARA&A*, 38:113–141, January 2000. doi: 10.1146/annurev.astro.38.1.113.

J. Takata, K. L. Li, Gene C. K. Leung, A. K. H. Kong, P. H. T. Tam, C. Y. Hui, E. M. H. Wu, Yi Xing, Yi Cao, Sumin Tang, Zhongxiang Wang, and K. S. Cheng. Multi-wavelength Emissions from the Millisecond Pulsar Binary PSR J1023+0038 during an Accretion Active State. *ApJ*, 785(2):131, April 2014. doi: 10.1088/0004-637X/785/2/131.

J. Takata, P. H. T. Tam, C. W. Ng, K. L. Li, A. K. H. Kong, C. Y. Hui, and K. S. Cheng. High-energy Emissions from the Pulsar/Be Binary System PSR J2032+4127/MT91 213. *ApJ*, 836(2):241, February 2017. doi: 10.3847/1538-4357/aa5c80.

T. M. Tauris and E. P. J. van den Heuvel. *Formation and evolution of compact stellar X-ray sources*, volume 39, pages 623–665. 2006.

T. M. Tauris, M. Kramer, and N. Langer. Recycling Pulsars: spins, masses and ages. In Joeri van Leeuwen, editor, *Neutron Stars*

and Pulsars: Challenges and Opportunities after 80 years, volume 291 of *IAU Symposium*, pages 137–140, March 2013. doi: 10.1017/S1743921312023393.

Thomas M. Tauris, Edward P. J. van den Heuvel, and Gerrit J. Savonije. Formation of Millisecond Pulsars with Heavy White Dwarf Companions:Extreme Mass Transfer on Subthermal Timescales. *ApJ*, 530(2):L93–L96, February 2000. doi: 10.1086/312496.

Marco Tavani and Jonathan Arons. Theory of High-Energy Emission from the Pulsar/Be Star System PSR 1259-63. I. Radiation Mechanisms and Interaction Geometry. *ApJ*, 477(1):439–464, March 1997. doi: 10.1086/303676.

A. M. Thompson and T. V. Cawthorne. Cyclotron emission from white dwarf accretion columns. *MNRAS*, 224:425–434, January 1987. doi: 10.1093/mnras/224.2.425.

C. Thompson, R. D. Blandford, Charles R. Evans, and E. S. Phinney. Physical Processes in Eclipsing Pulsars: Eclipse Mechanisms and Diagnostics. *ApJ*, 422:304, February 1994. doi: 10.1086/173728.

Richard C. Tolman. Static Solutions of Einstein's Field Equations for Spheres of Fluid. *Physical Review*, 55(4):364–373, February 1939. doi: 10.1103/PhysRev.55.364.

Diego F. Torres. Order parameters for the high-energy spectra of pulsars. *Nature Astron.*, 2:247–256, February 2018. doi: 10.1038/s41550-018-0384-5.

V. Tudor, J. C. A. Miller-Jones, A. Patruno, C. R. D'Angelo, P. G. Jonker, D. M. Russell, T. D. Russell, F. Bernardini, F. Lewis, A. T. Deller, J. W. T. Hessels, S. Migliari, R. M. Plotkin, R. Soria, and R. Wijnands. Disc-jet coupling in low-luminosity accreting neutron

stars. *MNRAS*, 470(1):324–339, September 2017. doi: 10.1093/mnras/stx1168.

G. Valente, T. Pisanu, P. Bolli, S. Mariotti, P. Marongiu, A. Navarrini, R. Nesti, A. Orfei, and J. Roda. The dual-band LP feed system for the Sardinia Radio Telescope prime focus. In *Proc. SPIE*, volume 7741 of *Society of Photo-Optical Instrumentation Engineers (SPIE) Conference Series*, page 774126, July 2010. doi: 10.1117/12.857306.

E. P. J. van den Heuvel and J. van Paradijs. Fate of the companion stars of ultra-rapid pulsars. *Nature*, 334(6179):227–228, July 1988. doi: 10.1038/334227a0.

Christian J. T. van der Merwe, Zorawar Wadiasingh, Christo Venter, Alice K. Harding, and Matthew G. Baring. X-ray Through Very-High-Energy Intrabinary Shock Emission from Black Widows and Redbacks. *arXiv e-prints*, art. arXiv:2010.01125, October 2020.

M. P. van Haarlem, M. W. Wise, A. W. Gunst, G. Heald, J. P. McKean, J. W. T. Hessels, A. G. de Bruyn, R. Nijboer, J. Swinbank, R. Fallows, M. Brentjens, A. Nelles, R. Beck, H. Falcke, R. Fender, J. Hörandel, L. V. E. Koopmans, G. Mann, G. Miley, H. Röttgering, B. W. Stappers, R. A. M. J. Wijers, S. Zaroubi, M. van den Akker, A. Alexov, J. Anderson, K. Anderson, A. van Ardenne, M. Arts, A. Asgekar, I. M. Avruch, F. Batejat, L. Bähren, M. E. Bell, M. R. Bell, I. van Bemmel, P. Bennema, M. J. Bentum, G. Bernardi, P. Best, L. Bîrzan, A. Bonafede, A. J. Boonstra, R. Braun, J. Bregman, F. Breitling, R. H. van de Brink, J. Broderick, P. C. Broekema, W. N. Brouw, M. Brüggen, H. R. Butcher, W. van Cappellen, B. Ciardi, T. Coenen, J. Conway, A. Coolen, A. Corstanje, S. Damstra, O. Davies, A. T. Deller, R. J. Dettmar, G. van Diepen, K. Dijkstra, P. Donker, A. Doorduin, J. Dromer, M. Drost, A. van Duin, J. Eislöffel, J. van

Enst, C. Ferrari, W. Frieswijk, H. Gankema, M. A. Garrett, F. de Gasperin, M. Gerbers, E. de Geus, J. M. Grießmeier, T. Grit, P. Gruppen, J. P. Hamaker, T. Hassall, M. Hoeft, H. A. Holties, A. Horneffer, A. van der Horst, A. van Houwelingen, A. Huijgen, M. Iacobelli, H. Intema, N. Jackson, V. Jelic, A. de Jong, E. Juette, D. Kant, A. Karastergiou, A. Koers, H. Kollen, V. I. Kondratiev, E. Kooistra, Y. Koopman, A. Koster, M. Kuniyoshi, M. Kramer, G. Kuper, P. Lambropoulos, C. Law, J. van Leeuwen, J. Lemaitre, M. Loose, P. Maat, G. Macario, S. Markoff, J. Masters, R. A. McFadden, D. McKay-Bukowski, H. Meijering, H. Meulman, M. Mevius, E. Middelberg, R. Millenaar, J. C. A. Miller-Jones, R. N. Mohan, J. D. Mol, J. Morawietz, R. Morganti, D. D. Mulcahy, E. Mulder, H. Munk, L. Nieuwenhuis, R. van Nieuwpoort, J. E. Noordam, M. Norden, A. Noutsos, A. R. Offringa, H. Olofsson, A. Omar, E. Orrú, R. Overeem, H. Paas, M. Pand ey-Pommier, V. N. Pandey, R. Pizzo, A. Polatidis, D. Rafferty, S. Rawlings, W. Reich, J. P. de Reijer, J. Reitsma, G. A. Renting, P. Riemers, E. Rol, J. W. Romein, J. Roosjen, M. Ruiter, A. Scaife, K. van der Schaaf, B. Scheers, P. Schellart, A. Schoenmakers, G. Schoonderbeek, M. Serylak, A. Shulevski, J. Sluman, O. Smirnov, C. Sobey, H. Spreeuw, M. Steinmetz, C. G. M. Sterks, H. J. Stiepel, K. Stuurwold, M. Tagger, Y. Tang, C. Tasse, I. Thomas, S. Thoudam, M. C. Toribio, B. van der Tol, O. Usov, M. van Veelen, A. J. van der Veen, S. ter Veen, J. P. W. Verbiest, R. Vermeulen, N. Vermaas, C. Vocks, C. Vogt, M. de Vos, E. van der Wal, R. van Weeren, H. Weggemans, P. Weltevrede, S. White, S. J. Wijnholds, T. Wilhelmsson, O. Wucknitz, S. Yatawatta, P. Zarka, A. Zensus, and J. van Zwieten. LOFAR: The LOw-Frequency ARray. *A&A*, 556: A2, August 2013. doi: 10.1051/0004-6361/201220873.

J. van Paradijs and J. E. McClintock. Optical and ultraviolet observations of X-ray binaries. In *X-ray Binaries*, pages 58–125, January

1995.

Alexandra Veledina, Joonas Nättilä, and Andrei M. Beloborodov. Pulsar Wind-heated Accretion Disk and the Origin of Modes in Transitional Millisecond Pulsar PSR J1023+0038. *ApJ*, 884(2):144, October 2019. doi: 10.3847/1538-4357/ab44c6.

D. A. Verner, G. J. Ferland, K. T. Korista, and D. G. Yakovlev. Atomic Data for Astrophysics. II. New Analytic FITS for Photoionization Cross Sections of Atoms and Ions. *ApJ*, 465:487, July 1996. doi: 10.1086/177435.

Guillaume Voisin, René P. Breton, and Charlotte Summers. A spider timing model: accounting for quadrupole deformations and relativity in close pulsar binaries. *MNRAS*, 492(2):1550–1565, February 2020. doi: 10.1093/mnras/stz3430.

S. D. Vrtilek, J. C. Raymond, M. R. Garcia, F. Verbunt, G. Hasinger, and M. Kurster. Observations of Cygnus X-2 with IUE : ultraviolet results from a multiwavelength campaign. *A&A*, 235:162, August 1990.

Richard A. Wade and Keith Horne. The Radial Velocity Curve and Peculiar TiO Distribution of the Red Secondary Star in Z Chamaeleontis. *ApJ*, 324:411, January 1988. doi: 10.1086/165905.

Zorawar Wadiasingh, Christo Venter, Alice K. Harding, Markus Böttcher, and Patrick Kilian. Pressure Balance and Intrabinary Shock Stability in Rotation-powered-state Redback and Transitional Millisecond Pulsar Binary Systems. *ApJ*, 869(2):120, December 2018. doi: 10.3847/1538-4357/aaed43.

Zhongxiang Wang, Rene P. Breton, Craig O. Heinke, Christopher J. Deloye, and Jing Zhong. Multiband Studies of the Optical Periodic Modulation in the X-Ray Binary SAX J1808.4-3658 during Its

Quiescence and 2008 Outburst. *ApJ*, 765(2):151, March 2013. doi: 10.1088/0004-637X/765/2/151.

Anna L. Watts, Nils Andersson, Deepto Chakrabarty, Marco Feroci, Kai Hebeler, Gianluca Israel, Frederick K. Lamb, M. Coleman Miller, Sharon Morsink, Feryal zel, and et al. Colloquium: Measuring the neutron star equation of state using x-ray timing. *Reviews of Modern Physics*, 88(2), Apr 2016. ISSN 1539-0756. doi: 10.1103/revmodphys.88.021001. URL `http://dx.doi.org/10.1103/RevModPhys.88.021001`.

Rudy Wijnands. Accretion-Driven Millisecond X-ray Pulsars. In John A. Lowry, editor, *Trends in Pulsar Research*, page 53, January 2006.

Rudy Wijnands and Michiel van der Klis. A millisecond pulsar in an X-ray binary system. *Nature*, 394(6691):344–346, July 1998. doi: 10.1038/28557.

R. Willingale, R. L. C. Starling, A. P. Beardmore, N. R. Tanvir, and P. T. O'Brien. Calibration of X-ray absorption in our Galaxy. *MNRAS*, 431(1):394–404, May 2013. doi: 10.1093/mnras/stt175.

J. Wilms, A. Allen, and R. McCray. On the Absorption of X-Rays in the Interstellar Medium. *ApJ*, 542(2):914–924, October 2000. doi: 10.1086/317016.

Y. X. Yap, K. L. Li, A. K. H. Kong, J. Takata, J. Lee, and C. Y. Hui. Face changing companion of the redback millisecond pulsar PSR J1048+2339. *A&A*, 621:L9, January 2019. doi: 10.1051/0004-6361/201834545.

L. Zampieri, G. Naletto, C. Barbieri, E. Verroi, M. Barbieri, G. Ceribella, M. D'Alessandro, G. Farisato, A. Di Paola, and P. Zoc-

carato. Aqueye+: a new ultrafast single photon counter for optical high time resolution astrophysics. In Ivan Prochazka, Roman Sobolewski, and Ralph B. James, editors, *Photon Counting Applications 2015*, volume 9504 of *Society of Photo-Optical Instrumentation Engineers (SPIE) Conference Series*, page 95040C, May 2015. doi: 10.1117/12.2179547.

L. Zampieri, G. Naletto, C. Barbieri, A. Burtovoi, M. Fiori, A. Spolon, P. Ochner, L. Lessio, G. Umbriaco, and M. Barbieri. (Very) Fast astronomical photometry for meter-class telescopes. *Contributions of the Astronomical Observatory Skalnate Pleso*, 49(2):85–96, May 2019a.

Luca Zampieri, Aleksandr Burtovoi, Michele Fiori, Giampiero Naletto, Alessia Spolon, Cesare Barbieri, Alessandro Papitto, and Filippo Ambrosino. Precise optical timing of PSR J1023+0038, the first millisecond pulsar detected with Aqueye+ in Asiago. *MNRAS*, 485 (1):L109–L113, May 2019b. doi: 10.1093/mnrasl/slz043.

C. Zurita, J. Casares, and T. Shahbaz. Evidence for Optical Flares in Quiescent Soft X-Ray Transients. *ApJ*, 582(1):369–381, January 2003. doi: 10.1086/344534.

Piotr T. Życki, Chris Done, and David A. Smith. The 1989 May outburst of the soft X-ray transient GS 2023+338 (V404 Cyg). *MNRAS*, 309(3):561–575, November 1999. doi: 10.1046/j.1365-8711.1999.02885.x.

Ringraziamenti

Ringrazio Sergio e Paolo per avermi accolta all'Osservatorio di Merate e avermi seguita nel corso del mio dottorato. Con il passare del tempo, conoscendoli meglio ho capito la gran fortuna che ho avuto incontrandoli nel mio percorso. Devo loro molto, sia dal punto di vista umano, che professionale. In questi tre anni mi hanno appassionato alla ricerca, insegnandomi molto, sollecitando la mia curiositá e spingendomi a migliorare. Insieme a loro ringrazio Federica, tutti i ricercatori e studenti dell'area Swift, che hanno sempre creato un'atmosfera ricca di allegria e di cooperazione.

Ringrazio i miei colleghi e amici astrofisici, Alessandro, Francesco e Filippo, che hanno reso il dottorato un'esperienza indimenticabile. Grazie soprattutto a loro il lavoro é diventato un piacere e un'occasione anche per ridere e scherzare. Grazie Filippo per i viaggi passati insieme, per avermi fatto scoprire nuovi luoghi a Roma e per essere andati insieme in uno dei posti piú belli del mondo ad osservare. Grazie Ghedo e Max per avermi accolta come una di voi. Grazie Alessandro per l'amicizia, le lunghe chiacchierate e le gite in Sardegna. Grazie Francesco per la tua dolcezza, che infonde serenitá e allegria.

Ringrazio le mie amiche di sempre, Daria e Laura, per tutti questi anni di amicizia, per le serate in compagnia e per essere venute spesso a trovarmi nella solitaria Sartirana. Daria, una parte di questo dottorato é anche tua, anche se sono sicura che non la vorrai...senza di te e i nostri splendidi viaggi (organizzati da te) sarei stata senz'altro meno serena. Quando la pandemia sará passata..il mio zaino sará pronto per la prossima avventura. Un grazie anche a tutti gli amici e amiche di Venezia, che hanno reso piacevoli i miei rientri a casa.

Un grazie agli amici dell'universitá, che da lontano hanno condiviso questo difficile percorso. Grazie Caterina per tutte le telefonate e il sostegno e grazie Achille per aver sognato insieme il Cile (dove prima o poi spero andremo). Grazie Silvia, é stato bello condividere con te le

tante avventure di questo dottorato. Un grazie anche a tutti i ragazzi della foresteria di Merate e a Chiara per essermi stata tanto vicina.

Grazie Elise e Leonardo per i pomeriggi passati insieme a giocare, ridere e scherzare. Anche da lontano riuscite a trasmettermi felicitá.

Grazie Alessandro, Domitilla, Luigi, Andrea, Marta, Cristina, Teo e a tutti i ricercatori con cui ho avuto il piacere di collaborare e dai quali ho imparato tanto.

Un grazie speciale a Giampaolo, per tutto l'amore, l'aiuto e il sostegno che mi ha dato. Siamo cresciuti insieme affrontando diverse difficoltá, ma anche realizzando molti sogni comuni. Mi hai riempito di curiositá con le tue passione, facendomi diventare una persona e una ricercatrice migliore.

Un grazie a tutti i luoghi dove mi sono sentita a casa, da Fregona a Venezia, Padova e Sartirana..ma anche a tutte le bellezze che ho visto per la prima volta e mi hanno fatto sognare ad occhi aperti. Ringrazio la mia famiglia, perché per quanto vivace non mi ha mai fatto sentire sola e mi ha spinto sempre ad inseguire i miei sogni. Gli interminabili litigi, o discussioni come voi li chiamate, alla fine ci hanno unito di piú negli anni rendendoci una cosa sola.

Grazie Paolo Ferrari, perché senza di te forse questo percorso non sarebbe mai iniziato. Nonostante il tuo difficile carattere mi sono affezionata a te e tutt'ora ti considero un amico, oltre che un bravo insegnante. I pomeriggi e le serate a parlare e a risolvere problemi di trigonometria sono un ricordo indelebile. Mi hanno permesso di apprezzare, forse per la prima volta, la matematica e l'astronomia.